I

Study of Optical Phase Lock Loops and the Applications in Coherent Beam Combining and Coherence Cloning

Thesis by

Wei Liang

In Partial Fulfillment of the Requirements for the

degree of

Doctor of Philosophy

CALIFORNIA INSTITUTE OF TECHNOLOGY

Pasadena, California

2008

(Defended March 6, 2008)

Acknowledgements

I would like to use this opportunity to express my sincere gratitude to all people who have helped me on the long journey to finish my Ph.D thesis. Without their support, my accomplishments would not be possible.

First of all, I want to thank the Department of Applied Physics of Caltech for admitting me to the world-famous research institution. I also appreciate Prof. Amnon Yariv for guiding me and providing the environment to conduct the independent research in the foremost fields of optoelectronics. He also sets a role model for us by constantly showing his deep understanding of optics, persistent curiosity of physics, and profound knowledge of humanities including language, literature, arts and music.

The last few years of research have been exciting and prosperous for me. The research works presented in this thesis were all conducted in the last three years. I have to thank Dr. Tony Kewitsch and Dr. George Rakuljic for bringing me the chance to work on such an important project aimed towards solving practical problems. Dr. Tony is also the best engineer I have seen and has taught me a great deal of lab skills. Dr. George Rakuljic showed me the positive altitude and mindset of being an entrepreneur. I also feel lucky to work with Naresh Satayan on these projects. Lots of the ideas I have had won't be realized without his help and the intense discussion with him, and the projects won't have progressed so smoothly without his contribution. It was also an enjoyable experience to work with Firooz from Prof. Hossein Hashemi's group at USC. I sincerely respect Firooz's knowledge on RF circuit design, and the rigor he takes in his analysis. Dr. Reg Lee is another person I appreciate. He is very helpful for technique and engineering questions.

I am also deeply indebted to the other people I have worked with during my Ph.D studies.. Prof. Yong Xu is the first postdoc I have worked with. He has always impressed me with his understanding of physics, skillful use of mathematics and simulations, and

acute perception of emerging field in optics. I also greatly enjoyed working with Prof. Yanyi Huang during the middle stage of my Ph.D studies. He not only showed me his extensive lab skills but also acted as a role model for creating the balance between a joyful life and effective work. Prof. Lan Yang is another person I am grateful for; she always encouraged me when I was frustrated and helped me on both research work and immigration issues. Prof. Joyce Poon impressed me with not only her drive and motivation in the scientific research but also with her affection – a quality rare among men – towards the group. Of course I won't forget the help of the other members including Prof. Bruno Crosignani, Ali Ghaffari, John Choi, Xiankai Sun, Philip Chak, Lin Zhu, George Paloczi, and Will Green. The group lunch discussions, particularly the argument between Lin and Joyce Poon always brought laughter and inspiration to our quiet research life.

I also need to thank Connie Rodriguez and Irene Loera for their constant help. In addition to organizing all the group activities, Connie is also a big source for help and advice on every aspect of life from food to culture. Having a chat with her proves to be a good way for relieving work stress and learning some idioms.

There are also lots of friends in Caltech including Peng Wang, staffs from ISP, etc., who helped me to get through the long and difficult Ph.D life. Their encouragement and the exciting and fun activities we did together will always be the best memories of my life.

Most importantly, I want to thank my family, especially my parents for working their best to give me the education, the opportunities and freedoms to pursue my dreams and interests. I also would like to devote my special gratitude to my wife Jing, who has brought the fresh air, and the excitement to my last few years in graduate school, and has been a source for advice, support, criticism, and joy.

Abstract

A phase lock loop (PLL) is a negative feedback control system that fixes the frequency and phase of a local oscillator in relation to the frequency and phase of a "reference" signal. Electronic phase lock loop has been studied for more than half a century and has been widely used for clock recovery and generation, spread spectrum, clock distribution, jitter and noise reduction.

However, the study and applications of Optical phase lock loop (OPLL), the counterpart of electronic PLL in the optical domain, are far from the same level of progress as electronic PLL. Part of the reason is that most applications of optical signals so far do not require the precise control of the phase of the optical signals; another reason is that most implemented OPLLs are based on either gas lasers or solid state lasers, whose bulky size and high cost inhibit the applications of OPLLs.

Today semiconductor lasers are being used in numerous applications due to their low cost, small size, and high efficiency. OPLLs based on SCLs were once studied in the late 1980s and early 1990s for coherent optical communication purposes. However, at that time, a few technical difficulties associated with SCLs were not completely solved and the technology was not mature. Since the invention of Erbium doped fiber amplifier, direct detection has become the dominant technology for telecommunication and research on SCL OPLLs has declined abruptly.

In the last decade, heavy investment in telecom has significantly improved the performance of SCLs. Emerging applications have drawn the attention of researchers to phase coherent optics again. In this thesis, I report on a study of OPLLs using commercial SCLs, and explore the applications in emerging fields other than telecommunication.

The first part introduces the theory of OPLLs and presents the experimental study of OPLLs made from different commercial SCLs. The non-uniform FM response of single-section SCLs and the non-negligible loop delay are identified as the critical factors which

limit the performance of the OPLLs. In order to improve the performance of OPLLs, electronic compensations using filter designs are also discussed and studied.

In the second part, the application of OPLLs in coherent beam combining is firstly studied. Using OPLLs, an array of slave lasers can be phase locked to the same master laser at the same frequency, their outputs can then be coherently combined. The phase variations of the element beams due to the optical path-length variations in fibers can be further corrected for by using multi-level OPLLs. This approach eliminates the use of the optical phase/frequency shifters conventionally required in a coherent beam combining system. Proof of principle experiments are demonstrated using the filled-aperture combining scheme. Furthermore, I will discuss the scalability of a cascaded filled-aperture combining system for the combination of a large number of lasers.

The second application using OPLLs explored in this work is to clone the superior coherence property of a high-quality master laser to inexpensive SCLs. First, I will describe the theory of coherence transfer using OPLLs. I will then present the experimental measurements of the linewidths and frequency noises of the master laser, the free-running and locked slave lasers.

The thesis concludes by identifying future works that need to be done to advance the development of this technology.

Table Of Contents

List of Figures

List of Publications

1. **Liang W**, Satyan N, Aflatouni F, Yariv A, Kewitsch A, Rakuljic G, Hashemi H, "Tiled-aperture Coherent Beam Combining Using Heterodyne Optical Phase Lock Loops," *In preparation.*
2. **Liang W**, Satyan N, Aflatouni F, Yariv A, "Cloning the Coherence Property of a Low Noise Fiber Laser to Semiconductor Lasers Using Heterodyne Optical Phase Lock Loops," *In preparation.*
3. Satyan N, **Liang W**, Yariv A, Kewitsch A, Rakuljic G, Aflatouni F**,** Hashemi H, "Phase-controlled Apertures using Heterodyne Optical Phase-Lock Loops," *submitted to Photonics Technology Letters.*
4. **Liang W**, Satyan N, Aflatouni F**,** Yariv A, Kewitsch A, Rakuljic G, Hashemi H, "Coherent beam combining with multi-level optical phase lock loops," JOSA B, **24**, pp. 2930-2939 (2007).
5. **Liang W**, Satyan N, Yariv A, Kewitsch A, Rakuljic G, Aflatouni F**,** Hashemi H and Ungar J, "Coherent Combining of High Power MOPA Semiconductor Lasers Using Optical Phase-Lock Loops (OPLLs)," Optics Express, **15**, 3201-3205 (2007).
6. **Liang W**, Yariv A, Kewitsch A and Rakuljic G, "Coherent Combining of Two Semiconductor Lasers Using Optical Phase-Lock Loops (OPLLs)," Opt. Lett. **32,** 370-372, 2007.
7. **Liang W**, Satyan N, Yariv A, Kewitsch A, Rakuljic G, Aflatouni F**,** Hashemi H, "Coherent beam combining with OPLLs," SPIE Photonics West, 2008.
8. **Liang W**, Satyan N, Yariv A, Kewitsch A, Rakuljic G, **"**Narrow Linewidth High Power Semiconductor MOPA Achieved Using Optical Phase Lock Loops (OPLLs)," Frontiers in Optics, 2007.
9. Yariv A, **Liang W**, Satyan N, Kewitsch A, Rakuljic G, "Coherent Combination of Semiconductor Lasers Using Optical Phase Lock Loops," IEEE International Topical Meeting on Microwave Photonics, Victoria, Canada, October 2007.
10. **Liang W**, Yariv A, Kewitsch A, Rakuljic G, "Coherent Combination of Two Semiconductor Lasers Using Optical Phase Locked Loops (OPLLs)," Frontiers in

Optics, 2006.

11. Yariv A, **Liang W,** Kewitsch A, Rakuljic G, Ungar J., “Semiconductor Lasers as Current Controlled Oscillators in Optical Phase-Lock Loops (OPLLs),” DARPA MTO RF Photonics Symposium, August 2006.

Glossary of Acronyms

AOM - Acoustic optical modulator

CBC - Coherent beam combining

CCO - Current controlled oscillator

DFB - Distributed feedback

DSHI - Delayed self-heterodyne interferometer

FFT - Fast Fourier transfer

FM - Frequency modulation

FSR - Free spectral range

FWHM - Full-width-at-half-maximum

LIDAR - Light detection and ranging

LO - Local oscillator

LP - Low pass

MOPA - Master oscillator power amplifier

OpAmp - Operational amplifier

OPLL - Optical Phase Lock Loop

OSA - Optical spectrum analyzer

PD - Photo-detector or phase-detector

PLL - Phase lock loop

PM - phase modulator

PSD - Power spectral density

RF - Radio frequency

RIN - Relative intensity noise

SBC - Spectral beam combining

SCL - Semiconductor laser

TEC - Thermoelectric cooler

VCO - Voltage controlled oscillator

Chapter 1 Introduction

1.1 Background and motivation

Phase locked loops(PLLs) are the most prolific feedback systems today and are widely used in almost all electronic systems including satellite communication systems, radars, cell phones, televisions, radios, pagers, computers, etc.[1, 2] The concept of PLL was first developed in the 1930's. The key parts in a PLL include a phase detector (PD) and a local oscillator whose frequency can be tuned by changing the input voltage or current. The system forces the local oscillator (LO) to follow the frequency/phase of an incoming reference signal. The earliest widespread use of PLLs was in radio and television. After the first PLL integrated circuit arrived in the 1960's, there has been an explosion of the use of PLLs in FM demodulation, synchronization, frequency synthesizers, etc.

Optical phase lock loops (OPLLs) are essentially the counterparts of PLLs in the optical domain, where a slave laser is used as the LO and is phase-locked to a master laser. The role of the phase detector is played by a photo detector. OPLL was first described four years after the invention of laser in 1960's[3]. Since then OPLLs based on various laser systems have been demonstrated[4-11]. One would naturally expect OPLLs to have a similar significance and impact in the optical domain as their counterparts have in the electronic domain. Historically, OPLLs have been studied for very few applications, including coherent optical communication[12-15], RF signal generation and delivery[4, 9-11], and most recently, in optical clocks[16-18]. Most of the OPLLs have been demonstrated in laboratories and have never achieved wide commercial application. The great potential of OPLL technology is far from being realized. This can be attributed to

both the very high cost, the immaturity of OPLL technology, and the lack of mature applications demanding this technology.

In an OPLL, the most critical condition to achieve the optical phase locking is that the sum of the linewidths of the master laser and the slave laser be much smaller than the loop bandwidth. This condition is relatively easy to implement with solid state lasers, gas lasers and fiber lasers because they have superior frequency stability and very narrow linewidth (equal or less than a few kHz), so they do not require a high loop bandwidth to be locked[11, 19]. However these lasers are very expensive and bulky. In addition, they are typically thermal or piezo tuned, which limits their tuning speed and range. These lasers have recently been used in very special applications, including space coherent optical communication[20], precision frequency standard synthesized using optical clocks[16-18], and accurate control of fiber lengths for millimeter wave signal distribution in large radio telescope arrays[21].

In comparison with solid state and fiber lasers, semiconductor laser (SCL) is a more favorable candidate to build agile, low cost OPLLs for a variety of applications, due to their unparalleled advantages:

- SCLs have a very high energy efficiency; state-of-the-art solid state lasers or fiber lasers have an efficiency of around 10%, while SCLs with efficiencies greater than 80% have been demonstrated recently.
- SCLs are significantly cheaper than solid state or fiber lasers.
- SCLs can be current tuned at very high speed.

- SCLs are very small. Due to their small size, the compatibility of their fabrication process with the semiconductor industry, and their current frequency tuning capability, SCLs are the excellent candidates to build integrated OPLL, which will significantly reduce their cost and open up numerous applications.

On the negative side, SCLs possess wide linewidth, which requires a high loop bandwidth and high speed feedback electronics to lock the lasers. A serious issue with single section SCLs is that their current frequency modulation(FM) response exhibits a 180^0 phase reversal within the frequency range of 0.1-10 MHz, which limits the loop bandwidth to the same frequency range[22, 23]. In order to efficiently lock the SCLs, either their linewidth has to be reduced, or the laser structure has to be redesigned to obtain a wide uniform FM response. In the late 1980's and early 1990's, a great deal of research activity was directed to the development of a coherent receiver for long-range coherent optical communication. Sub-MHz external cavity SCLs were built in laboratories and used to implement OPLLs [7, 9]. However, external cavity SCLs are complex, expensive, and bulky. Multi-section SCLs were demonstrated to possess a flat FM response up to a few GHz[11, 24]. However these lasers were only built in laboratories and had reliability issues[23]. In addition, coherent communication technology lost out to direct detection optical communication technology since the invention of Erbium doped fiber amplifiers in the 1990's. Research into SCL OPLLs has declined abruptly since then, except for some continuing work on RF signal generation with OPLLs[11].

In the last decade, the performance of SCLs has been improved significantly as a result of heavy investment in the telecom industry towards the end of the last century. Low cost telecom standard DFB lasers and external cavity SCLs with sub-MHz linewidth are now commercially available. The fact that their linewidth is smaller than the loop bandwidth limited by the thermal crossover makes it possible to lock these low cost, highly reliable commercial SCLs, and paves the way for a number of emerging applications. In this thesis I will study the OPLLs based on state-of-the-art commercial SCLs. In particular I will study the use of various high speed feedback electronics designs to improve the performance of SCL OPLLs, and explore the application of SCL OPLLs in coherent beam combining and coherence cloning.

Coherent beam combining(CBC) promises to enable high power laser systems with near-ideal beam quality for a number of industrial applications[25, 26]. Of the different CBC techniques, active feedback phase control is the most promising and has attracted intensive study[25, 27]. Conventionally, optical phase or frequency shifters such as phase modulators, fiber stretchers and acoustic optical modulators (AOM) are used in the feedback phase control system[25, 27-29]. Due to their ability to control the phase of the slave laser, OPLLs provide a natural platform for phase control of the SCLs, which enables a full electronic phase control system and significantly reduces the cost and dimension of the system by eliminating optical frequency/phase shifters.

Another application of OPLLs explored in this thesis is coherence cloning. For example, an optical sensing network requires a large number of coherent sources of very

narrow linewidths. Instead of using a number of solid state lasers or fiber lasers, an array of inexpensive SCLs can be locked to one high quality laser so that they have similar superior coherence properties. This technology can significantly reduce the system cost by eliminating the need for a large number of expensive solid state or fiber lasers. Another possible application is in the field of high precision optical clock signal distribution. Isolated high finesse optical cavities has been used to narrow a laser linewidth to less than Hz[30, 31]. One can easily transfer the superior frequency stability and coherence of this sophisticated laser system to SCLs by using heterodyne OPLLs.

1.2 Thesis outline

This thesis is organized as follows: The theoretical analysis of PLL in both the time and the frequency domain is presented in Chapter 2, with the latter one being the emphasis of this study. A major analysis tool called the bode plot, is introduced, and is used to study the performance of a PLL in terms of its stability, acquisition range, holding range, residual frequency noise, etc. I then add the non-uniform current FM response of the SCLs and the non-negligible loop delay into the analysis and consider their influence on the loop performance.

Chapter 3 is devoted to the experimental study of OPLLs. This chapter starts with the measurement of current FM response, and then presents the experimental demonstration and characterization of OPLLs based on various commercial SCLs. The last part of this chapter is devoted to the electronic filter design aimed at optimizing the system's performance. In particular, a phase lead-lag filter, passive and active lag-lead filters and an aided acquisition circuit are discussed and implemented.

An experimental study of coherent beam combining using OPLLs is presented in Chapter 4. I will first demonstrate the combination of two slave lasers phase locked to the

same master laser. However the optical path length variation in the combining fibers changes the combined output power and needs to corrected for. A higher level PLL control loop using a RF voltage controlled oscillator(VCO) is introduced, analyzed, and implemented to correct for the optical path length variation in fiber. A combining efficiency of 94% is demonstrated.

Although I have demonstrated the coherent combining of two SCLs, the scalability of this technology to the combination of a large number of lasers is not clear. In Chapter 5, I will use a cascaded filled-aperture scheme to analyze the efficiency of combining a large number of lasers in the presence of various noise sources. In particular I will consider the residual differential phase error due to the limited loop bandwidth, the phase error introduced by the VCO phase control loop, the phase noise introduced by the high power fiber amplifiers in the MOPA scheme, the phase front error introduced by combining optics, and intensity noise.

In Chapter 6 I will present the study of coherence cloning using OPLLs. First I will present the theoretical description of the coherence property of a laser under both the free-running and the phase-locked conditions. I will then describe the measurement of the laser lineshape using a self-delayed heterodyne interferometer, and the measurement of frequency noise using a Mach Zehnder interferometer. Finally the measured linewidths and frequency noises of the master laser, the free-running and the phase-locked slave lasers are shown and compared.

Chapter 2 Theory of Optical Phase lock Loops

A Phase Lock Loop (PLL) is a negative feedback control system, which forces a local oscillator (LO) to track the frequency and phase of a reference signal within the loop bandwidth. This same idea can be used to construct an Optical Phase Lock Loop (OPLL), in which a slave laser tracks the frequency and phase of the optical signal of a master laser. In this chapter, I will study the theory of an OPLL in detail. I will first summarize the basic concept and theory of OPLLs and present both the time domain and the frequency domain analyses of an OPLL. I will then linearize the system using the small signal approximation and utilize the transfer function methodology to study the stability, acquisition range, holding range, and the residual phase noise of the OPLLs. Finally the effect of the loop delay and the non-uniform FM response will be considered.

2.1 Principle of operation

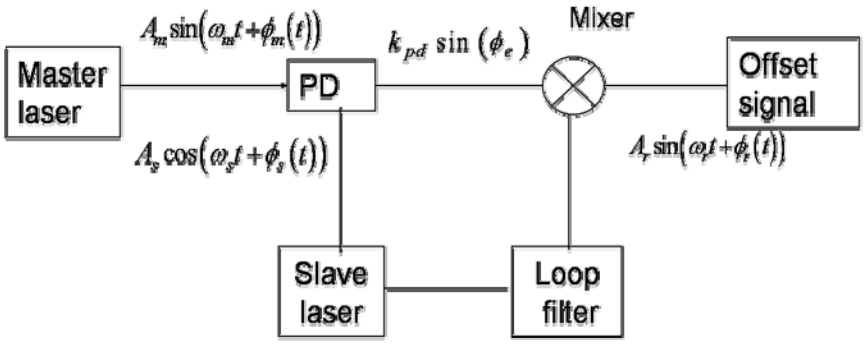

Fig. 2.1 Schematic diagram of an OPLL.

A schematic diagram of a typical heterodyne OPLL is plotted in Fig. 2.1. The optical signals of the master laser $A_m \sin(\omega_m t + \phi_m)$ and the slave laser $A_s \sin(\omega_s t + \phi_s)$ are combined at a photodetector, which detects the phase and frequency differences. The output of the photodetector is further mixed with a reference signal $A_r \sin(\omega_r t + \phi_r)$. The

down-converted phase error signal passes through a loop filter and is fed back to the slave laser. The frequency and phase of the slave laser are modulated by the feedback current, and are forced to track those of the master laser with a frequency and phase offset determined by the reference signal. A rigorous analysis of the OPLLs can be performed in either the time domain or the frequency domain.

2.2 Time domain analysis

The operation principle of an OPLL is very similar to the well-studied electronic PLLs. Therefore the theoretical analysis of OPLL can be directly borrowed from the theoretical framework of PLLs[1, 2]. In Fig. 2.1 the photodetector and the radio frequency (RF) mixer together play the role of a phase detector. The master laser signal and the slave laser signal are mixed and fed into the photodetector (with a built-in trans-impedance amplifier), the resulting output is given by

$$v_1(t) = 2R_{pd}\sqrt{P_m P_s}\sin\left[(\omega_m - \omega_s)t + \phi_m(t) - \phi_s(t)\right] \tag{2.1}$$

where R_{pd} is the responsivity of the photodetector, P_m and P_s are the optical power of the master laser and the slave laser respectively. $v_1(t)$ is further mixed with a RF reference signal $E_r = A_r\cos\left(\omega_r t + \phi_r(t)\right)$ using a RF mixer. Neglecting the sum frequency term, the down-converted phase error current signal provided by the mixer is

$$i(t) = K_{pd}\sin\phi_e = K_{pd}\sin\left[(\omega_m - \omega_s - \omega_r)t + \phi_m(t) - \phi_s(t) - \phi_r(t)\right] \tag{2.2}$$

where $K_{pd} = \eta R_{pd}\sqrt{P_m P_s}A_r$ is defined as the gain of the phase detector, and η is the current responsivity of the RF mixer. Care must be taken when determining η since most mixers are neither ideal current sources nor ideal voltage sources, and η also depends on the load applied to the output port of the mixer. The down-converted phase error signal is fed back to the slave laser, whose phase is modulated as

$$\frac{d\phi_s(t)}{dt} = K_s \cdot \left\{ i(t) * f_{flt}(t) * f_s(t) \right\} \tag{2.3}$$

where K_s is the current FM sensitivity of the slave laser and $f_{flt}(t)$ and $f_s(t)$ are the impulse response of the loop filter and the slave laser respectively. By setting all the d/dt terms equal to zero in Eq. (2.3), the steady state solution is obtained as

$$\begin{aligned} &\omega_s = \omega_m - \omega_r \ , \ \phi_s = \phi_m - \phi_r - \phi_{e0} \\ &sin(\phi_{e0}) = (\omega_m - \omega_{s,fr} - \omega_r) / K_{dc} \end{aligned} \tag{2.4}$$

where $\omega_{s,fr}$ is the frequency of the free-running slave laser, $K_{dc} = K_{pd} K_f K_s$ is the loop DC gain, K_f is the DC response of the loop filter, and ϕ_{e0} is the steady state phase error. Eq. (2.4) shows that the frequency and phase difference between the locked slave laser and the master laser are set by the RF reference signal. This configuration is called heterodyne OPLL. If there is no frequency offset, i.e., $\omega_r = 0$, when the loop is in lock $\omega_s = \omega_m$ and the system becomes a homodyne OPLL. The analyses of heterodyne and homodyne OPLLs are similar, except that the frequency and phase of the RF reference signal have to be considered in Eq. (2.2) and the conversion gain of the mixer has to be included while calculating the loop gain. For the sake of simplicity, I will use the homodyne OPLL scheme to perform the analysis in the remainder of the thesis, unless explicitly stated otherwise.

In general Eq. (2.3) is a complex nonlinear differential equation involving convolutions and there is no simple analytic solution. To understand the fundamental dynamic process of this feedback control system, I assume that the response of the slave laser is instantaneous, i.e., $f_s(t) = \delta(t)$. Ignoring the loop filter and using the dynamic variable $\phi_e = \phi_m - \phi_s$, Eq. (2.3) reduces to

$$\phi_e'(t) + K_{dc} \sin \phi_e(t) = \phi_m'(t) \tag{2.5}$$

where $K_{dc} = K_{pd}K_s$ is the loop DC gain. Assuming a small phase error $\phi_e(t) << 1$, the solution to this differential equation takes the form

$$\phi_e(t) = e^{-K_{dc}t}\int e^{-K_{dc}t'}\phi_m'(t')dt' + ce^{-K_{dc}t} \tag{2.6}$$

It is instructive to look at two simple cases. The first case is one starting with a constant phase error, i.e., $\phi_e(0) = \Delta\phi$, then the solution is

$$\phi_e(t) = \Delta\phi e^{-K_{dc}t} \tag{2.7}$$

Eq. (2.7) corresponds to an exponentially decaying phase error with a time constant $1/K_{dc}$, so that the phase of the slave laser eventually tracks the phase of the master laser. The loop gain K_{dc} determines the speed of phase-tracking, or the loop bandwidth.

Another typical case is one of a phase ramp $\phi_m(t) = \Delta\omega \cdot t$. This is the case when there exists an initial frequency offset $\Delta\omega$ between the slave laser and the master laser. The solution to this case is

$$\phi_e(t) = \frac{\Delta\omega}{K_{dc}}\left(1 - e^{-K_{dc}t}\right) \tag{2.8}$$

In this case in the limit $t \to \infty$ there is a nonzero steady state phase error

$$\phi_{e0} = \Delta\omega / K_{dc} \tag{2.9}$$

which results in a constant feedback current, that forces the frequency of the slave laser to track that of the master laser. Eqs. (2.7) and (2.8) show that the function of an OPLL is to force the phase and frequency of the slave laser to track that of the master laser.

2.3 Frequency domain analysis

2.3.1 Transfer function method

Frequency domain analysis is a more convenient and powerful tool in characterizing OPLLs. In the time domain, solving Eq. (2.3) involves a complicated and

time-consuming convolution algorithm. In the frequency domain, Eq. (2.3) involves only products of Fourier transforms, i.e., the transfer functions. The performance of OPLLs such as their stability, the loop bandwidth, the compensation filter design can be analyzed by means of the transfer function formalism and Bode plots.

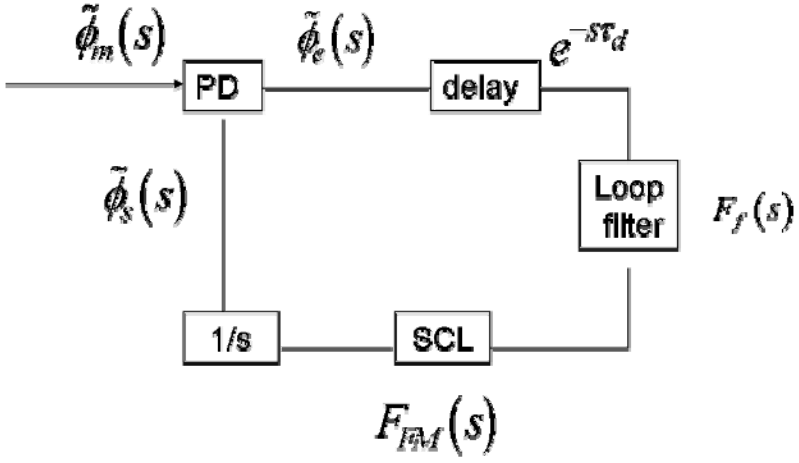

Fig. 2.2 The frequency domain representation of OPLLs.

The schematic frequency domain representation of a homodyne OPLL is shown in Fig. 2.2. $s = j\omega$ is the Laplace variable, $\exp(-s\tau_d)$ represents the delay of the loop, $F_f(s)$ is the normalized transfer function of the loop filter, and $F_{FM}(s)$ is the normalized transfer function of the FM response of the slave laser. The 1/s block originates from the fact that the phase ϕ, which is the dynamic variable, is the integration of the frequency over time. By using the small signal perturbation to linearize Eq. (2.3) about the steady state locking point ϕ_{e0}, and taking the Fourier transform, the open loop transfer function is derived as

$$G_{op}(s) \equiv \frac{\phi_s(s)}{\phi_e(s)} = \frac{K'_{dc} F_f(s) F_{FM}(s) \exp(-s\tau_d)}{s} \tag{2.10}$$

where $K'_{dc} = K_{dc} \cos\phi_{e0}$. The closed loop signal transfer function is defined as

$$H_o(s) \equiv \frac{\phi_s(s)}{\phi_m(s)} = \frac{G_{op}(s)}{1+G_{op}(s)} = \frac{K'_{dc}F_{FM}(s)F(s)\exp(-s\tau_d)}{s+K'_{dc}F_{FM}(s)F(s)\exp(-s\tau_d)} \tag{2.11}$$

and the error transfer function is

$$H_e(s) \equiv \frac{\phi_e(s)}{\phi_m(s)} = \frac{1}{1+G_{op}(s)} = 1-H_o \tag{2.12}$$

The closed loop signal transfer function $H_o(s)$ acts as a low pass filter, which means that the phase of the slave laser tracks the phase of the master laser within the bandwidth of the filter. On the other hand, the phase error transfer function $H_e(s)$ behaves as a high pass filter. The differential phase error within the loop bandwidth is thus suppressed by the OPLL. In practice, the loop bandwidth is limited mainly by the non-negligible loop delay and the non-uniform FM response of the slave laser. These issues will be discussed in detail in Section 2.5.

2.3.2 Acquisition and holding range

Two important parameters describing the locking capability and the stability of the OPLL are the acquisition range Δf_{acq} (the maximal frequency difference between the free-running slave laser and the master laser for the OPLL to acquire lock), and the holding range Δf_h (the maximal frequency difference between the free-running slave laser and the master laser for the OPLL to stay in lock). The acquisition and holding ranges of a PLL generally depend on the loop gain and the loop order[32].

First order PLL

The first order PLL is defined as one with no loop filter, i.e., $F_f(s)=1$. If I assume that the slave laser has a flat frequency modulation response $F_{FM}(s)=1$, then the open loop gain is found from Eq. (2.10) as

$$G(s) = \frac{K_{dc}}{s}e^{-s\tau_d} \tag{2.13}$$

In this case, the acquisition and holding ranges are simply[1]

$$\Delta f_{acq} = \Delta f_h = K_{dc} / 2\pi \tag{2.14}$$

Second-order PLL

Traditionally three types of loop filters are typically used to make the second-order PLL: the lowpass(LP) filter, the passive lead-lag (or lag-lead) filter, and the active second-order filter. An active second-order filter has a transfer function of

$$F(s) = \frac{1+\tau_2 s}{\tau_1 s} \tag{2.15}$$

Since this type of filter has an integration term $1/s$, the loop has very high open loop gain at low frequency and provides the best performance with respect to phase noise reduction[1]. The acquisition and holding ranges are theoretically infinite for such a loop filter.

2.3.3 Bode plot and stability criterion

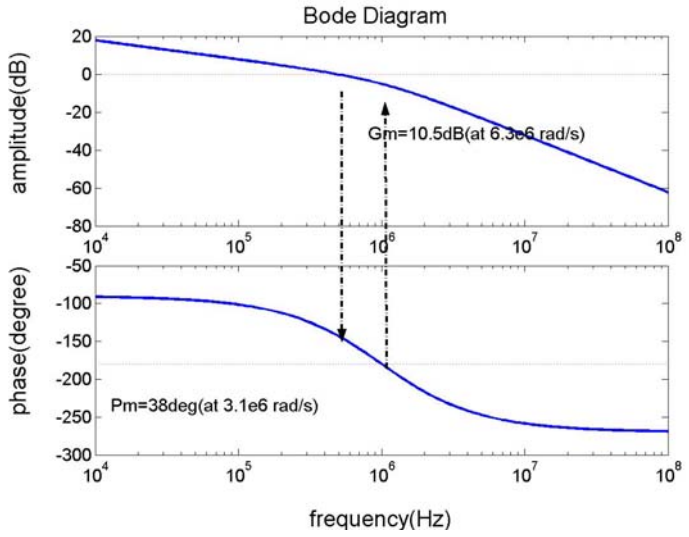

Fig. 2.3 The Bode plot of a PLL with a second-order low pass filter. The gain margin is $G_m = 10.5\ dB$ and the phase margin is $P_m = 38^0$.

The Bode plot is a powerful graphic tool in studying the performance and stability of

PLLs especially when various compensation filters are included. Fig. 2.3 shows the Bode plot of a PLL with a second-order low pass loop filter, in which both the amplitude $\left|G_{op}\left(j\omega\right)\right|$ (dB scale) and the phase $Arg\left[G_{op}\left(j\omega\right)\right]$ (in degrees) are plotted as a function of the frequency.

Stability criterion: The stability criterion of an OPLL can easily be derived from its Bode plot: if the amplitude of $G_{op}\left(s\right)$ crosses 0 dB at only one frequency, the amplitude $\left|G\left(j\omega_{\pi}\right)\right|$ must be smaller than 1 at the π phase lag frequency ω_{π} ($\angle G_{op}\left(j\omega_{\pi}\right)=-180^{o}$). Equivalently, the phase lag $\angle G_{op}\left(j\omega_{gc}\right)$ must be bigger than -180^{o} at the gain crossover frequency ω_{gc} ($\left|G_{op}\left(j\omega_{gc}\right)\right|=1$)[1]. This can be understood by the following intuitive reasoning. At the π phase lag frequency ω_{π} the original negative feedback system becomes a positive feedback system. If the amplitude of the loop gain is higher than 1, any noise in the system will be amplified in each round-trip, eventually leading to oscillations.

Stability margins

Based on the stability criterion, one can define two stability margins: the phase margin is defined as $\angle G_{op}\left(j\omega_{gc}\right)+\pi$, and the gain margin is defined as $-20\log\left|G_{op}\left(j\omega_{\pi}\right)\right|dB$. Sufficient phase margin or gain margin are necessary to guarantee the stability of the loop. Based on the time domain simulation, the gain margin is generally chosen to be within the range 8~10 dB to suppress excessive ringing during the acquisition[33].

2.4 Loop noise characterization

In an OPLL, various noise sources affect the loop performance and need to be considered. Among these noise sources, the phase noise of the SCLs, is the dominant one, since SCLs typically possess a linewidth between hundreds of KHz and a few MHz. Other noise sources include the photodetector shot noise and the electronics noise. A schematic

diagram of the various phase noise sources and their points of entry in an OPLL is shown in Fig. 2.4. The phase noise of the master laser and the slave laser are accounted for by ϕ_m^n and ϕ_s^n. ϕ_{sn} stands for the photodetector shot noise. The electronics noise is small and can be ignored.

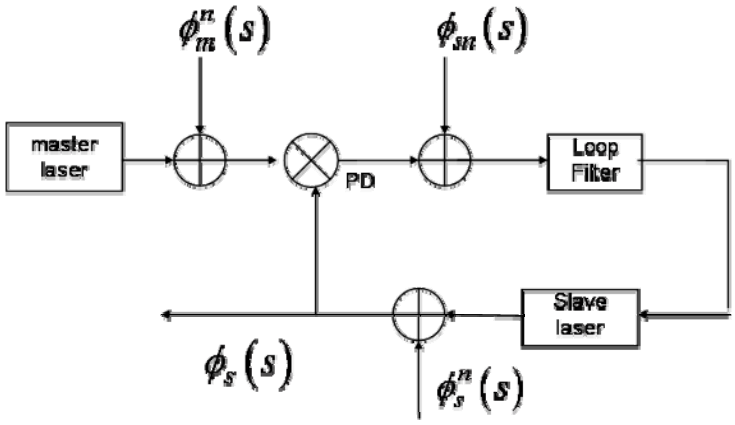

Fig. 2.4 Sources of phase noise in an OPLL

Following the standard negative feedback analysis, one obtain the phase of the locked slave laser and the differential phase error as

$$\phi_s(s) = \left(\phi_m + \phi_m^n\right) \cdot H_o + \phi_{sn} / K_{pd} \cdot H_o + \phi_s^n \cdot H_e \tag{2.16}$$

$$\phi_e(s) = \left(\phi_m + \phi_m^n + \phi_s^n\right) \cdot H_e + \phi_{sn} / K_{pd} \cdot H_o \tag{2.17}$$

The corresponding spectral power density functions are

$$S_s(f) = \left[S_m(f) + S_{sn}(f) / K_{pd}^2\right] \left|H_o(f)\right|^2 + S_{s,fr}(f) \left|H_e(f)\right|^2 \tag{2.18}$$

$$S_e(f) = \left[S_m(f) + S_{s,fr}(f)\right] \cdot \left|H_e(f)\right|^2 + S_{sn}(f) / K_{pd}^2 \cdot \left|H_o(f)\right|^2 \tag{2.19}$$

where $S_{s,fr}, S_m, S_{sn}$ are, respectively, the spectral density functions of phase noise of the free-running slave laser, the phase noise of the master laser, and the shot noise.

Here I will only use the differential phase error to characterize the noise level of an OPLL. A detailed analysis and measurement of the phase noise of the slave laser in an OPLL will be given in Chapter 6 (Coherence cloning using OPLLs). Assuming that the

frequency noise of the lasers has a white Gaussian distribution, the double-sided spectral densities of the different noise sources are given by [19]

$$S_m(f)=\frac{\Delta f_m}{2\pi f^2},\ \ S_s(f)=\frac{\Delta f_s}{2\pi f^2},\ S_{sn}(f)=2eR(P_s+P_m) \tag{2.20}$$

where Δf_m and Δf_s are the FWHM linewidths of the master laser and the free-running slave laser, R is the responsivity of the photodetector. Fig. 2.5 shows the power spectral density of the differential phase error ϕ_e in a typical OPLL with a loop delay of 100 ns. At low frequencies, the phase error is significantly reduced by the feedback loop. As the loop gain increases, the bandwidth and ratio of the noise reduction increase. However, as the gain approaches the maximum allowable loop gain, as per the stability criterion, a spectral peak appears and the noise at the corresponding frequency is significantly amplified. In Fig. 2.5(b) an active second-order filter $(1+f/f_0)/(f/f_0)$ is used to further reduce the phase noise at low frequencies.

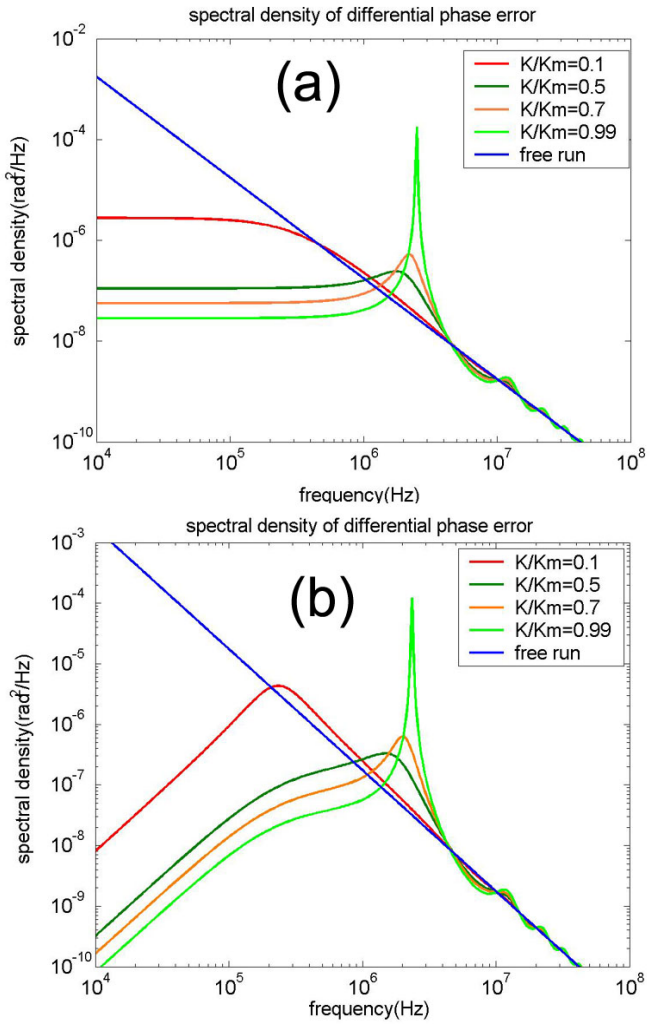

Fig. 2.5 The spectral density functions of the differential phase error ϕ_e for different small signal loop gain K. K_m is the maximum allowable loop gain determined by the stability criterion. (a) No loop filter is used. (b) An active second-order filter $(1+f/f_0)/(f/f_0)$ is used. In both (a) and (b), a loop delay of 100 ns is assumed.

An important parameter called the phase error variance can be obtained by integrating the phase noise spectral density over all frequencies

$$\sigma^2 = \int_{-\infty}^{\infty} S(f)df \tag{2.21}$$

Thus the variance of the differential phase error is

$$\sigma_{\phi_e}^2 = \int_{-\infty}^{+\infty} S_{\phi_e} df = \int_{-\infty}^{+\infty} \left[S_m(f) + S_{s,fr}(f) \right] \cdot \left| H_e(f) \right|^2 + S_{sn}(f) / K_{pd}^2 \cdot \left| H_o(f) \right|^2 df \quad (2.22)$$

Combining Eq. (2.20) with the definitions

$$B_n = \int_0^{\infty} H_o(f) df \text{ and } I_p = \int_0^{\infty} H_e(f) / f^2 df \quad (2.23)$$

Eq. (2.22) is simplified to

$$\sigma_{\phi_e}^2 = \frac{\Delta f}{\pi} I_p + \frac{eB_n (P_m + P_s)}{RP_m P_s} \quad (2.24)$$

where $\Delta f = \Delta f_m + \Delta f_s$ is the sum of the linewidths of the master laser and the slave laser.

In the presence of phase noise, the loop loses lock through cycle slipping (the output phase error rotates through 2π after initially starting at zero)[1], and the noise in the OPLL can be evaluated by the average time between cycle slips T_{cs}. For the first order, the modified first-order, and the second-order type II loops, T_{cs} is related to σ^2 by, respectively[1]

$$T_{cs-I} \simeq \pi e^{2/\sigma^2} / 4B_n, \quad T_{cs-II} \simeq e^{\pi/2\sigma^2} / B_n \quad (2.25)$$

2.5 Practical limitations of the loop bandwidth

In the previous analysis, the bandwidth, acquisition range, holding range and noise reduction capability of an OPLL all rely on one critical parameter: i.e., the loop gain K_{dc}. Therefore, a large, loop gain is desired. However, K_{dc} is limited by two major practical constraints – namely, the non-negligible loop delay and the non-uniform frequency modulation response of SCLs. In this section I will analyze the loop performance limited by these two factors.

2.5.1 The non-negligible loop delay

Loop delay exists in all practical feedback control systems. In the presence of the loop delay, the phase lag increases unbounded as the frequency increases. As described in Section 2.3.3, the stability criterion requires the loop gain to be restricted to less than 1 at the 180 degree phase lag frequency. Hence the loop gain and the resulting loop bandwidth will be limited. In electronic PLLs made of integrated circuits, the length of the loop is at most a few mm and the delay is not a serous concern. In constructing an OPLL, either using micro-optics or using fiber optical components, the delay can be as big as a few ns. As the desired loop bandwidth is equal or greater than tens of MHz, due to the large linewidth of SCLs, the effect of the loop delay at these frequency ranges can't be ignored. Here I first restrict the analysis to the case where the loop bandwidth is only limited by the loop delay. The FM responses of the slave laser and all the electronics are assumed to be ideal. With the above assumption, and in the absence of a loop filter, the open loop transfer function (Eq. (2.10)) is simplified to

$$G_{op}(s) = K'_{dc}\frac{\exp(-s\tau_d)}{s} \tag{2.26}$$

and the 180^0 phase lag frequency is

$$\omega_\pi = \pi/2\tau_d \quad \text{or} \quad f_\pi = 1/4\tau_d \tag{2.27}$$

Considering the stability criterion described in Section 2.3.3, the maximum loop gain K_{dc} is $\pi/2\tau_d$. The resulting maximum holding range and acquisition range are $f_\pi = 1/4\tau_d$. In practice, this number is even smaller since a gain margin of 8~10 dB is needed to avoid excessive ringing.

I have studied the dynamic locking process in the time domain using the Simulink toolbox in MATLAB®. The FM response of the slave laser is assumed to be uniform, and the laser is modeled as an ideal integrator 1/s. As an example, I assume that the delay time is t_d = 5 ns, the frequency difference between the free-running slave laser and the

master laser is $\Delta\omega = 2$ MHz. No loop filter is used. The corresponding maximum loop gain in this case is $10\pi \times 10^7 \, rad/s$. The simulated temporal dependence of $\sin\phi_e(t)$ is plotted in Fig. 2.6. When the loop gain is $4\pi \times 10^7 \, rad/s$ (corresponding to a gain margin of 8dB), the photodetector output $\sin\phi_e(t)$ quickly settles down to the steady state locking point. As the loop gain is increased to $8\pi \times 10^7 \, rad/s$, $\sin\phi_e(t)$ converges to the steady state locking point with significant ringing. As the loop gain is further increased to $10.2\pi \times 10^7 \, rad/s$, the loop becomes unstable and starts oscillating. From this time domain simulation, one can see that a gain margin of at least 8 dB is needed to suppress ringing effects.

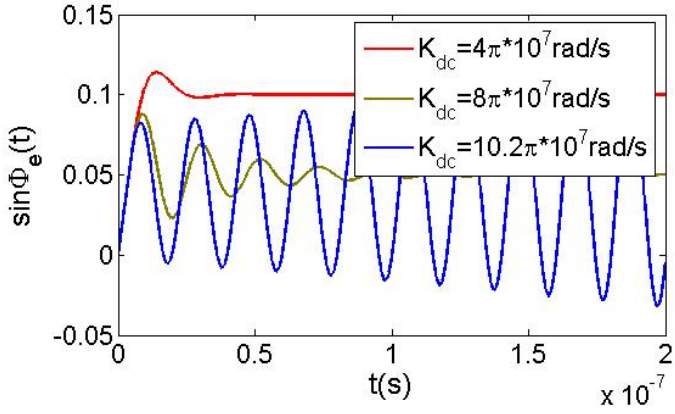

Fig. 2.6 Temporal dependence of $\sin\phi_e$ for different DC loop gain K_{dc}. A loop delay of 5 ns and a free-running frequency difference of 2 MHz are assumed in the simulation.

The variance of the differential phase error can be calculated according to Eq. (2.22). Using the parameters $P_m = P_s = 1mW$, R = 0.5A/W, and a gain margin of 8 dB, I calculate the variance of the differential phase error as a function of the loop delay and the summed linewidth of the lasers. From the calculation one observes that the variance of the differential phase error is only dependent on the summed linewidth normalized by

the π phase lag frequency, i.e. $\Delta f / f_\pi$, not on the absolute value of the delay time. This observation can be proved rigorously. By plugging Eq. (2.26) and Eq. (2.27) into Eq. (2.26) one obtains

$$\begin{aligned} B_n &= f_\pi \cdot \int_0^\infty \left| \frac{G_{mg} \exp\left(-\pi f'/2\right)}{f' + G_{mg} \exp\left(-\pi f'/2\right)} \right|^2 df' = \beta f_\pi \\ I_p &= \frac{1}{f_\pi} \cdot \int_0^\infty \left| \frac{1}{f' + G_{mg} \exp\left(-\pi f'/2\right)} \right|^2 df' = \alpha / f_\pi \end{aligned} \tag{2.28}$$

where $f' = f / f_\pi$ is the normalized frequency, $G_{mg} = K_{dc} / \left(K_{dc}\right)_{\max}$ is the gain margin, α and β are dimentionless numbers which only depend on the gain margin. Next I plug Eq. (2.28) back into Eq. (2.27) and get

$$\sigma_{\phi_e}^2 = \alpha \frac{\Delta f}{\pi f_\pi} + \beta f_\pi \frac{e\left(P_m + P_s\right)}{R P_m P_s} \tag{2.29}$$

Using typical values for $\Delta f \sim 1MHz$ for SCLs, $G_{mg} = 8dB$, $R \sim 0.5 A/W$, $P_s \sim 1mW$, $P_m \sim 0.01mW$ and $f_\pi \le 100MHz$, I estimate that the second term ($\sim 10^{-6} rad^2$) is much smaller than the first term($\sim 0.01 rad^2$) in Eq. (2.29). Therefore $\sigma_{\phi_e}^2$ only depends on the normalized laser linewidth, i.e., $\sigma_{\phi_e}^2 = \alpha \Delta f / \pi f_\pi$. In Fig. 2. I plot the variance of the differential phase error as a function of the normalized summed laser linewidth $\Delta f / f_\pi$. If one uses T_{cs}=10years as the figure of merit for a high performance OPLL, the summed laser linewidth has to be smaller than ~1/60 of $f_\pi = 1/4\tau_d$. When fiber optical components are used, τ_d is typically 5 ns. It can be reduced to ~0.5 ns if microoptics are used instead. The corresponding summed laser linewidth has to be smaller than ~0.8MHz or ~8 MHz separately to achieve T_{cs}=10years.

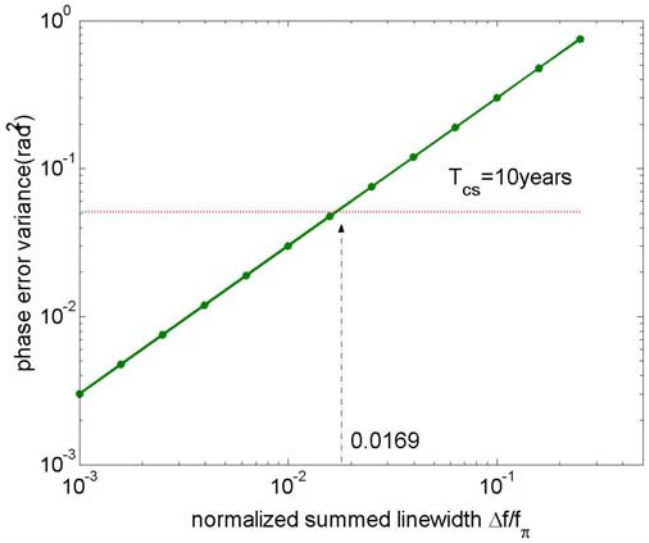

Fig. 2.7 The variance of the differential phase error as a function of the normalized summed laser linewidth $\Delta f / f_\pi$. $f_\pi = 1/4\tau_d$ is the π phase lag frequency given by the loop delay. T_{cs} is the average time between cycle slips defined in Eq. (2.25).

2.5.2 The non-uniform frequency modulation (FM) response of SCLs

In an SCL based OPLL, the SCL acts as a current-controlled oscillator (CCO) and its frequency is directly modulated by the current feedback signal[34, 35]. In the previous analysis I have assumed that the slave laser is an ideal CCO with a flat FM response. In practice, the FM response of SCLs is not uniform and exhibits different characteristics depending on the range of the modulation frequency. For a typical single-section SCL, the low frequency (smaller than 10MHz) FM response is dominated by the thermal effect and the carrier-induced effect. At the intermediate frequency (above 100MHz), the thermal effect fades out and the carrier-induced effect is the summation of an adiabatic term and a transient term[35]. As the modulation frequency further increases to a few GHz, the relaxation resonance effect becomes significant. All these phenomena contribute to the FM response and need to be examined in the OPLL analysis.

First, the relaxation resonance effect is excluded in this analysis since it is significant

only at frequencies above a few GHz, which is far beyond the OPLL bandwidths (< 10MHz) encountered in this work.

In the intermediate frequency range, the FM response is composed of two terms, the adiabatic term and the transient term[35]. Using the results of [35], the current-phase modulation of a SCL is given by

$$\frac{d\phi_s}{dt} = A\frac{d}{dt}i + Bi \tag{2.30}$$

where A and B are respectively the adiabatic and the transient modulation coefficients, and i is the modulation current. Taking the Fourier transform of Eq. (2.30) and substituting it into Eq. (2.10), the open loop transfer function becomes

$$G_{op}(s) = \frac{K_{dc}}{s}\left(1+\frac{A}{B}s\right)\exp\left(-s\tau_d\right) \tag{2.31}$$

In Eq. (2.31) A/B is typically around 10^{-11}[35], which means the adiabatic term becomes significant only at frequencies above 1 GHz. One can thus ignore its effect within the typical OPLL bandwidths studied in this work.

At frequencies smaller than 100MHz, the FM response of SCLs is composed of the thermal effect and the carrier-induced effect. While the carrier-induced effect is in phase with the modulation current and results in a blue shift with increasing current, the thermal effect is out of phase with the modulation current and produces a red shift. Due to the competition between the thermal and the carrier-induced effects, the FM response of a single section SCL exhibits a characteristic π phase reversal in the frequency range 100 kHz~10 MHz[23]. Compared to the loop delay, this phenomenon imposes a more serious constraint on the achievable loop bandwidth[22, 23, 36]. In this section I will analyze the influence of the thermal FM response on the performance of an OPLL.

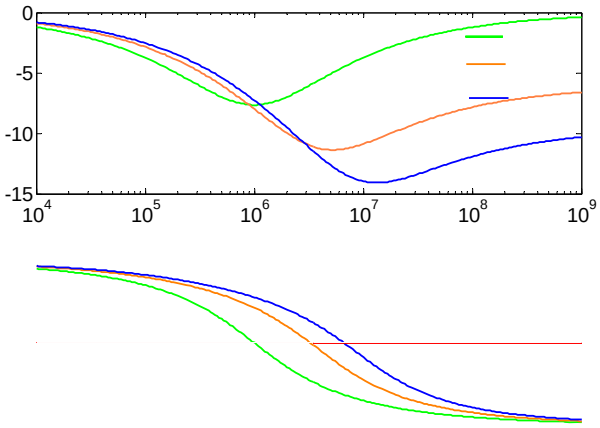

Fig. 2.8 FM response of single-section DFB lasers calculated with the modified low-pass filter model. The fitting parameters are: $f_c = 1MHz$ and b = 1, 2 and 3.

The thermal effect dominates at low frequency and fades out with the increase of the modulation frequency. Employing a modified low-pass filter model, an empirical FM transfer function of the thermal effect is given by[23, 37]

$$H_{th}(f) = -K_{th} \cdot \frac{1}{1+\sqrt{j f / f_c}} \tag{2.32}$$

where K_{th} is the thermal FM efficiency in Hz/mA and f_c is the thermal cut-off frequency. The fitting parameter f_c is structure-dependent and is typically in the range of 10kHz-10MHz[22]. The carrier-induced FM response is flat from DC to frequencies in the neighborhood of the relaxation frequency, and is in phase with the modulation current, i.e.

$$H_{el} = K_{el} \tag{2.33}$$

Combining the thermal and carrier-induced effects, the total FM response is described by

$$H_{FM}^{DFB}(f) = -\frac{K_0}{b}\left(\frac{b-\sqrt{jf/f_c}}{1+\sqrt{jf/f_c}}\right) \tag{2.34}$$

where K_0 is the DC current-frequency tuning sensitivity and $b = K_{th}/K_{el} - 1$ is related to the relative strengths of the carrier-induced effect and the thermal effect. In Fig. 2.8 I plot the FM responses for $f_c = 1MHz$ and b = 1, 2 and 3, respectively.

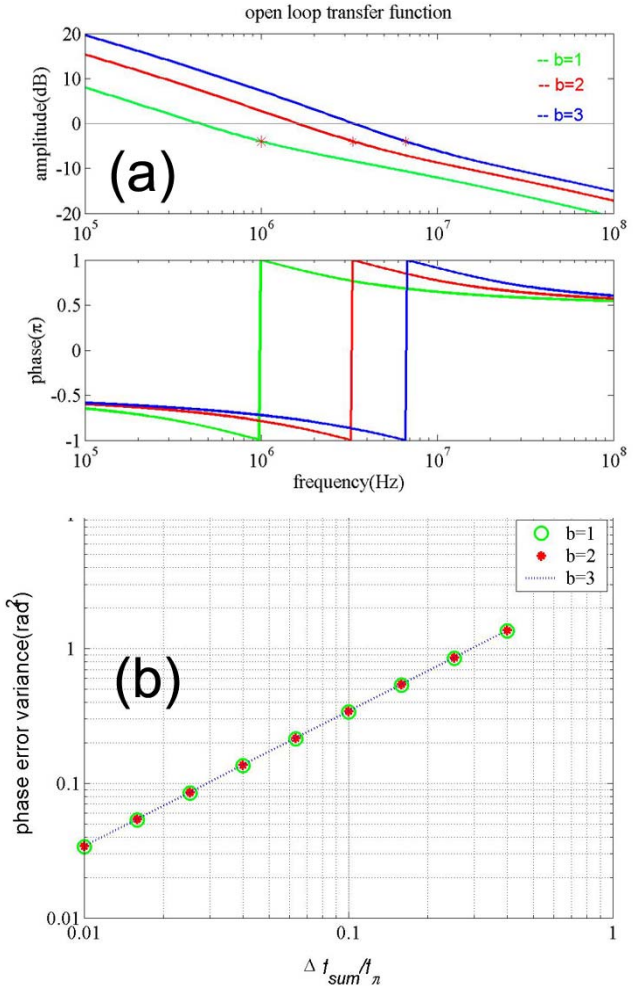

Fig. 2.9 (a) The Bode plots of the open loop transfer functions for different values of the fitting parameter b in Eq. (2.34). (b) The variance of the differential phase error as a function of the normalized laser linewidth $\Delta f / f_\pi$.

Substituting Eq. (2.34) into Eq. (2.10), I proceed to calculate the open loop transfer

function and the results are plotted in Fig. 2.9(a). The gain margin is 8 dB and the other parameters are the same as those in Fig. 2.8. The corresponding π phase lag frequencies f_π are 1, 3.2 and 6.6MHz respectively. I further calculate the variance of the differential phase error with Eq. (2.22). The results are shown in Fig. 2.9(b) as a function of the normalized summed laser linewidth $\Delta f / f_\pi$. Similar to the loop delay case, the variance of the differential phase error only depends on $\Delta f / f_\pi$ for a given gain margin.

In conclusion, to phase lock SCLs with reasonably small residual differential phase error, the summed linewidth has to be significantly smaller than the loop bandwidth. The bandwidth of the OPLL, however, is limited to a few MHz due to the non-uniform FM response of the single section SCLs. Historically, specially designed SCLs, such as multi-section DFBs, have been demonstrated to have flat FM response up to a few GHz[11]. However, these lasers are not commercially available and their stability needs to be improved. On the other hand, the linewidth of SCLs can be reduced by introducing optical feedback. Therefore external cavity SCLs with sub-MHz linewidth have been used to build OPLLs. In the next chapter, I will present and characterize the experimental study of OPLLs built using different commercial SCLs.

Chapter 3 Experimental study and optimization of OPLLs

In Chapter 2 I have presented the theory of OPLL and identified critical issues for OPLLs using SCLs. In this chapter I will present the detailed experimental study of OPLLs constructed using different commercial SCLs. I first start the chapter with the measurement of the current-frequency modulation (FM) response of SCLs. Once the FM response is known, one can include it into the open loop transfer function and model the performance of the OPLL. In Section 3.2 I will describe the experimental setup of OPLLs in details and the measurement results, in particular the spectrum of the beat signal between the master laser and the locked slave laser, from which the residual differential phase error can be characterized. In the last Section 3.3, I will discuss the use of various compensation filters and circuits to improve the acquisition range, the holding range, and the residual differential phase error.

3.1 Measurement of the FM response

In Chapter 2 I pointed out that the characteristic phase reversal of the FM response of the single-section SCLs presents the main constraint on the bandwidth of the OPLLs. Given the limited loop bandwidth, the slave laser can be locked to the master laser with reasonable locking quality only if the summed linewidth of the master laser and the slave laser is much smaller than the π phase lag frequency f_π,. The linewidth of typical SCLs lies between ~100kHz and ~10MHz and f_π is usually in the same frequency range. Thus the preliminary characterization of the linewidth and the FM response of the laser is necessary before implementing the OPLL.

The summed linewidth can be measured using a heterodyne mixing method. The signals of the master laser and the slave laser are first mixed at a high speed photodetector. An RF spectrum analyzer is then used to measure the linewidth of the photocurrent,

which is exactly the summed linewidth of the lasers. The FM response measurement, however, is more complicated and will be introduced in the following section.

3.1.1 Analysis of the FM response measurement system

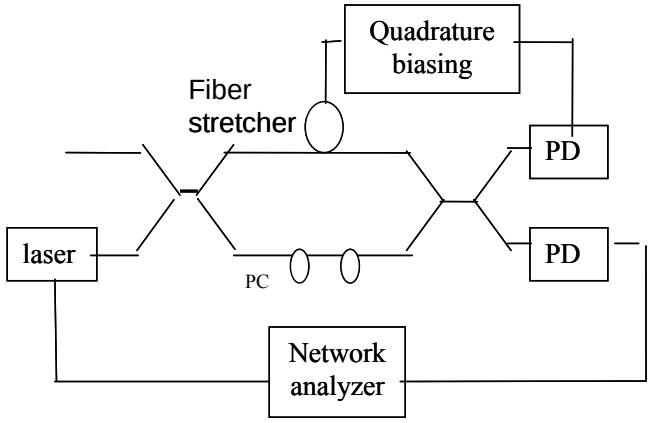

Fig. 3.1 Schematic diagram of a FM response measurement setup

The FM response of a laser can be measured with a network analyzer and an optical frequency discriminator[38]. Fig. 3.1 displays the schematic diagram of a typical FM response measurement setup. The network analyzer drives the laser with a modulation signal. The frequency of the laser is modulated and the frequency discriminator converts the frequency modulation into an intensity modulation, which is detected using a photodetector. The output of the photodetector is then fed back into the network analyzer to measure the amplitude and phase of the FM response of the laser[38].

The optical electric field fed into the frequency discriminator can be described by

$$E(t) = \sqrt{P(t)}e^{j(\omega_o t + \phi(t))} \tag{3.35}$$

where *P(t)* is the optical power, $\omega_0 = 2\pi f_0$ is the average angular frequency, and $\phi(t)$ is the optical phase. In a network analysis measurement, the laser is stimulated at a modulation frequency and its response (both amplitude and phase) is measured at the

same frequency. When the network analyzer applies a voltage modulation signal $\mathrm{Re}\left\{\tilde{V}_m e^{j\omega_m t}\right\}$ at the frequency $\omega_m = 2\pi f_m$ to the laser, the optical power is given by

$$P(t) = \mathrm{Re}\left\{P_0\left[1+\tilde{m}e^{j\omega_m t}\right]\right\} \tag{3.36}$$

where $\tilde{m}$ is a complex variable representing the intensity modulation factor. In general $\tilde{m}$ is a function of the modulation frequency.

Meanwhile the optical phase is also modulated as

$$\phi(t) = \mathrm{Re}\left\{\tilde{\phi}_m e^{j\omega_m t}\right\} \tag{3.37}$$

where $\tilde{\phi}_m$ is the complex phase modulation factor. The frequency modulation can be deduced from the phase modulation by taking the derivative of Eq. (3.37)

$$\upsilon(t) = \frac{1}{2\pi}\frac{d\phi}{dt} = \mathrm{Re}\left\{\tilde{\upsilon}_m e^{j\omega_m t}\right\} \tag{3.38}$$

where $\tilde{\upsilon}_m = \tilde{\phi}_m j f_m$ represents the frequency deviation of the optical carrier at the modulation frequency f_m.

The frequency discriminator depicted in Fig. 3.1 is simply a Mach-Zehnder interferometer. The modulated optical field is split into two signals using a fiber optical coupler. One part is delayed by time τ and then combined with the other signal again using a fiber optical coupler. The photocurrent resulted from the mixed signals is given by

$$I_D(t) \propto \left|E(t)+E(t-\tau)\right|^2 \tag{3.39}$$

where I have assumed 3-dB directional couplers and matched polarization states for the recombining signals. Substituting (3.35) into (3.39), the photocurrent becomes

$$I_D(t) \propto P(t)+P(t-\tau)+2\sqrt{P(t)P(t-\tau)}\cos\left(\Delta\phi(t)+\omega_0\tau\right) \tag{3.40}$$

where $\Delta\phi(t) = \phi(t)-\phi(t-\tau)$ is the phase difference between the recombining optical signals due to the differential delay τ through the interferometer. Information on the phase or frequency deviations of the input optical signal is contained in this phase

difference term.

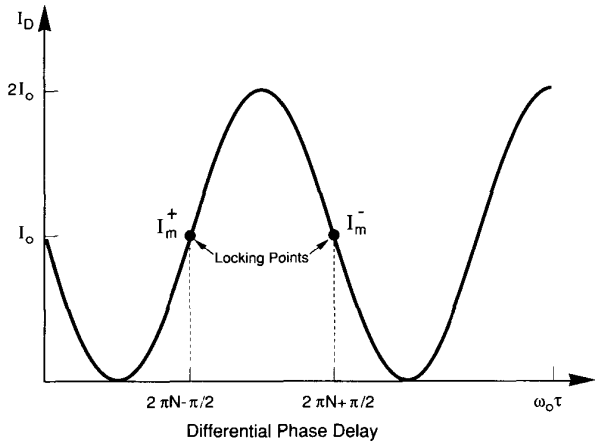

Fig. 3.2 Variation of the photocurrent at the output of a frequency discriminator as a function of the differential time delay τ without modulation.

Fig. 3.2 shows the variation of the photocurrent as a function of this differential time delay without any frequency modulation. By adjusting the differential time delay (e.g., through the use of a fiber stretcher) or the average optical frequency, the interferometer can be held in the quadrature condition (i.e., $\omega_0\tau = 2\pi N \pm \pi/2$). If both the intensity modulation and the phase modulation are small, one can plug Eqs. (3.36) and (3.38) into Eq. (3.40) and linearize it to derive the complex photocurrent

$$\tilde{I}_m(f_m) \approx I_0\left[\tilde{H}_m(f_m)\tilde{m}(f_m) \pm \tilde{H}_\upsilon(f_m)\tilde{\upsilon}_m\right] \tag{3.41}$$

where $\tilde{H}_m(f_m) = \cos(\pi f_m \tau)e^{-j\pi f_m \tau}$ is the intensity modulation transfer function and $\tilde{H}_\upsilon(f_m) = \pi\tau \sin c(\pi f_m \tau)e^{-j\pi f_m \tau}$ is the frequency modulation transfer function of the Mach-Zehnder interferometer. In our measurement, the time delay is chosen such that $f_m << 1/\tau$ which reduces $\tilde{H}_\upsilon(f_m)$ to a constant proportionality factor independent of the modulation frequency.

Eq. (3.41) shows that the measured photocurrent is a combination of both the filtered intensity modulation and frequency modulation on the optical input. One can separate the

intensity modulation and the frequency modulation responses by making two separate measurements, each biased at quadrature but on opposite slopes (see Fig. 3.2). By taking the vector subtraction of these two measurements, the intensity modulation response can be removed**.** Letting $\tilde{I}_m^+$ be the measured photocurrent at the modulation frequency while the discriminator is locked on the positive slope and $\tilde{I}_m^-$ for the negative slope (see Fig. 3.2), the FM response is obtained from Eq. (3.41) to give

$$\tilde{I}_{FM} = \tilde{I}_m^+ - \tilde{I}_m^- \approx 2I_0 \pi\tau \;\; \tilde{\upsilon}_m\left(f_m\right) \tag{3.42}$$

if the condition $f_m << 1/\tau$ is satisfied.

By comparing the photocurrent signal $\tilde{I}_{FM}$ to the driving voltage signal $\tilde{V}_m$, the network analyzer measures the amplitude and phase response of the whole system, including not only the FM response of the SCL, but also the response of the frequency discriminator, the photodetector, the electronics, and the delay of the optical fiber and the electric cable. This can be written down mathematically as

$$\tilde{H}'_{FM} = \frac{\tilde{I}_{FM}}{\tilde{V}_m} = \frac{\tilde{i}_m}{\tilde{V}_m} \cdot \tilde{H}_{FM}^{DFB} \cdot \tilde{H}_{\upsilon} \cdot \tilde{H}_{PD} \cdot \tilde{H}_{delay} \tag{3.43}$$

where $\tilde{H}'_{FM}$ is the measured frequency modulation response of the system, $\tilde{i}_m$ is the modulation current received by the laser, $\tilde{H}_{FM}^{DFB}$ is the current FM response of the laser, $\tilde{H}_{\upsilon}\left(f_m\right)$ is the response of the Mach Zehnder interferometer which is defined in Eq. (3.41), $\tilde{H}_{PD}$ is the response of the photodetector, and $\tilde{H}_{delay}$ represents the system delay.

To obtain $\tilde{H}_{FM}^{DFB}$, one needs to calibrate and remove the responses of all the other components. This can be done by performing an intensity modulation measurement using the same system with the shorter path of the Mach Zehnder interferometer disconnected. In this case the frequency discriminator acts as a fixed delay line. The measured intensity

modulation of the system can be described by

$$\tilde{H}'_{AM} = \frac{\tilde{I}_{AM}}{\tilde{V}_m} = \frac{\tilde{i}_m}{\tilde{V}_m} \cdot \tilde{H}_{AM} \cdot \tilde{H}_{PD} \cdot \tilde{H}_{delay} \tag{3.44}$$

where $\tilde{H}_{AM}$ accounts for the laser's intensity modulation response. The other variables are the same as those defined in Eq. (3.43). Dividing Eq. (3.43) by Eq. (3.44) one obtains the FM response of the laser

$$\tilde{H}_{FM}^{DFB} = \frac{\tilde{H}'_{FM}}{\tilde{H}'_{AM}\tilde{H}_{\upsilon}} \tilde{H}_{AM} \tag{3.45}$$

The measurement of the FM response is therefore calibrated by taking the ratio of the two measurements. The responses of the circuit, the delay, and the photodetector are automatically accounted for. For a modulation frequency much smaller than the relaxation resonance frequency of the laser, I can assume that the intensity modulation response of the laser $\tilde{H}_{AM}$ is a constant. The response of the frequency discriminator is also a constant for $f_m << 1/\tau$. Eq. (3.45) then reduces to

$$\tilde{H}_{FM}^{DFB} \sim \tilde{H}'_{FM} / \tilde{H}'_{AM} \tag{3.46}$$

Finally, the DC FM sensitivity can be obtained by changing the DC current and measuring the frequency shift.

3.1.2 Experimental measurement

To measure the FM response I constructed a FM response measurement setup similar to the one shown in Fig. 3.1. In the setup I use an Agilent 4395A network analyzer to drive the laser and measure the modulation response. The frequency range of the network analyzer is from 10Hz to 500MHz, which covers the typical thermal crossover frequency of SCLs. The photodetector I use is a New Focus 1544-B high speed photodetector. The frequency discriminator is made of two 3dB fiber couplers. The total length of the frequency discriminator (the longer path) is 1.7m and the differential delay length is

20cm which translates to the delay time $\tau \sim 1ns$. Typically the FM measurement is performed in the range of 1kHz to 50MHz, which satisfies the condition $f_m << 1/\tau$. In the measurement, the Mach Zehnder interferometer is not actively biased at its quadrature point. Thus the method described by Eq. (3.42) can not be directly used here. However, the high FM sensitivity of the SCLs combined with the high sensitivity of the frequency discriminator (proportional to the differential delay $\tau \sim 1ns$), result in the second term in Eq. (3.41) arising from the frequency modulation being typically 20dB higher than the first term arising from the intensity modulation. Therefore the intensity modulation in Eq. (3.41) can be ignored.

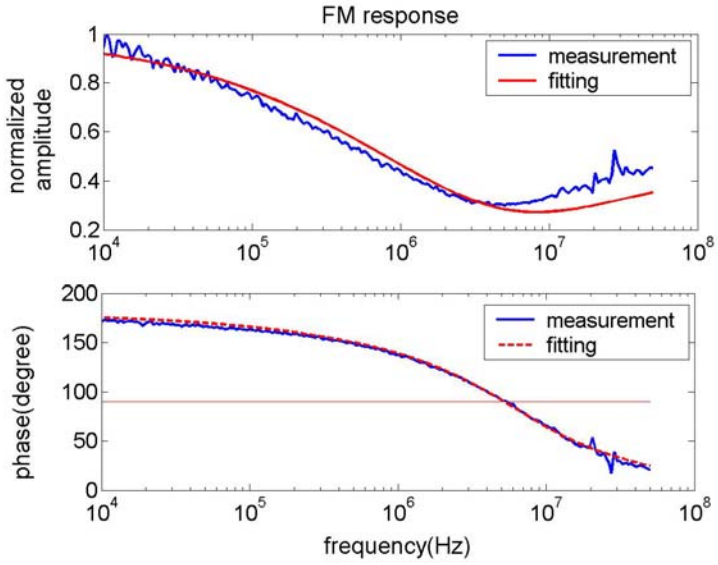

Fig. 3.3 Measurement (blue line) and theoretical fitting (red line) of the FM response of a JDSU DFB laser. The fitting parameters are: $b = 1.98$ and $f_c = 1.6MHz$.

I first measured the FM response of a JDSU CQF935/908 DFB laser. The laser is driven with an ILX low noise battery diode driver and the temperature is stabilized with an ILX TEC controller. The bias current is 400mA and the output power is 16dBm. By measuring the intensity modulation and the frequency modulation responses, I use Eq. (3.46) to calculate the FM response of the laser and the result is plotted in Fig. 3.3. The

blue solid line is the measured data and the red solid line is a theoretical fitting with the model described in Section 2.5.2 [23]

$$H_{FM}^{DFB}(f) = -\frac{K_0}{b}\left(\frac{b-\sqrt{jf/f_c}}{1+\sqrt{jf/f_c}}\right) \tag{3.47}$$

In obtaining Fig. 3.3 I have used the fitting parameters $b=1.98$ and $f_c=1.6MHz$. As I have discussed in Chapter 2.5.2, the amplitude of the FM response is not uniform and exhibits a characteristic dip at a few MHz. The phase of the FM response exhibits a π phase reversal starting from a few hundreds of kHz to a few tens of MHz.

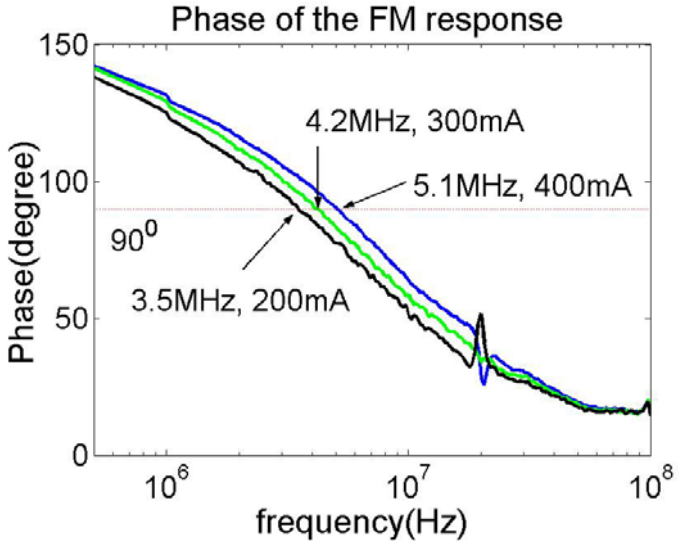

Fig. 3.4 Measured FM response of the JDSU DFB laser with different bias currents

It has been pointed out in [23] that the heat generated in the laser chip is proportional to the square of the bias current, and the small signal thermal FM strength is proportional to the bias current. According to the definition of the parameter *b* following Eq. (2.34), higher bias currents result in a stronger thermal FM contribution, which leads to a larger value of *b* and a higher thermal crossover frequency, as shown in Fig. 2.10. To confirm this I further measured the FM response of the JDSU DFB laser with bias currents of 200mA, 300mA and 400mA, respectively. The results are plotted in Fig. 3.4. As can be seen, the phase reversal of the FM response is indeed shifted to higher frequency with

higher bias current. Specifically, the 90 degree phase lag frequencies (corresponding to the π phase lag frequency in the open loop transfer function) are, respectively, 3.5MHz, 4.2MHz and 5.1MHz.

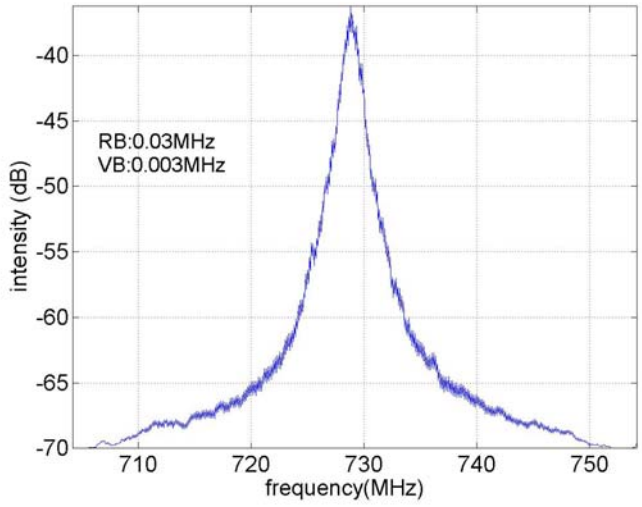

Fig. 3.5 Measured spectrum of the heterodyne beat signal between two JDSU DFB lasers

It is well known that the linewidth of a SCL is inversely proportional to the optical power[39]. Thus it is preferable to operate the laser at higher bias currents so that the loop performance can benefit from both the higher loop bandwidth (due to higher thermal crossover frequency of the FM response) and the smaller linewidth.

A straightforward method of measuring the linewidth of the laser is to heterodyne mix two lasers of similar linewidths and measure the RF beat signal on a spectrum analyzer. Fig. 3.5 gives the spectrum of the beat signal between two JDSU CQF 485 lasers measured with a HP 8565E RF Spectrum analyzer. The measured lineshape deviates from a Lorentzian shape due to frequency jitter. The summed FWHM is ~1.2MHz and the 20dB linewidth is ~ 7MHz. Since the summed 3dB linewidth is much smaller than the π phase lag frequency, $f_\pi \sim 5MHz$ determined from the non-uniform FM response, the laser can be locked.

3.2 Phase lock of different lasers

3.2.1 Phase lock of the JDSU DFB SCLs

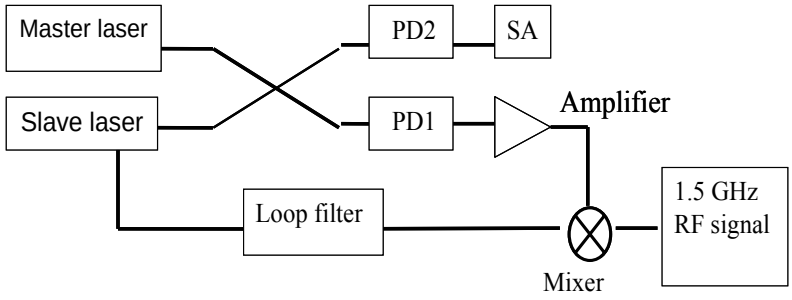

PD: photodetector SA: Spectrum analyzer

Fig. 3.6 Schematic diagram of a heterodyne OPLL.

I first built a heterodyne OPLL with the JDSU DFB laser as the slave laser and an Agilent 81640A tunable laser as the master laser. The schematic diagram of the system is plotted in Fig. 3.6. The master laser has a 3dB linewidth of about 50kHz and its output power can be adjusted from -20dBm to 3dBm. The JDSU laser is biased at 400mA and the output power is 16dBm. A 3dB 1550nm fiber optical coupler is used to combine the signals of the master laser and the slave laser. One output of the coupler is fed to the New Focus 1544B high speed photodetector, whose output is further down-converted by mixing with an offset RF signal (1.5GHz, ~15dBm) using a Minicircuits Z11-H RF mixer. The RF reference signal is produced by a HP8359A signal generator. The down-converted signal goes through a loop filter and is fed back to the slave laser to complete the negative feedback loop. The other output of the fiber coupler is fed into a HP 11982A photodetector, whose output signal is measured by an HP 8565 RF spectrum analyzer to monitor the locking status. An RF amplifier can be added following the output of the photodetector to further increase the total loop gain. With the electric gain compensation, the master laser signal can be reduced to as small as -15dBm to lock the slave laser. The fact that the loop gain can be electrically compensated enables the possibility of locking a

large number of slave lasers to one low power master laser.

The total delay time of the optical and the electric path is estimated to be about 5ns based on measuring their physical length. At the frequency of a few MHz, the phase lag due to this delay time is less than 10 degrees. Taking into account the inherent $\pi/2$ phase lag due to the integration of the current controlled oscillator, and the thermal crossover of the FM response, the π phase lag frequency f_π of the open loop transfer function should be about 5MHz. The measured acquisition range and holding range are about 9MHz.

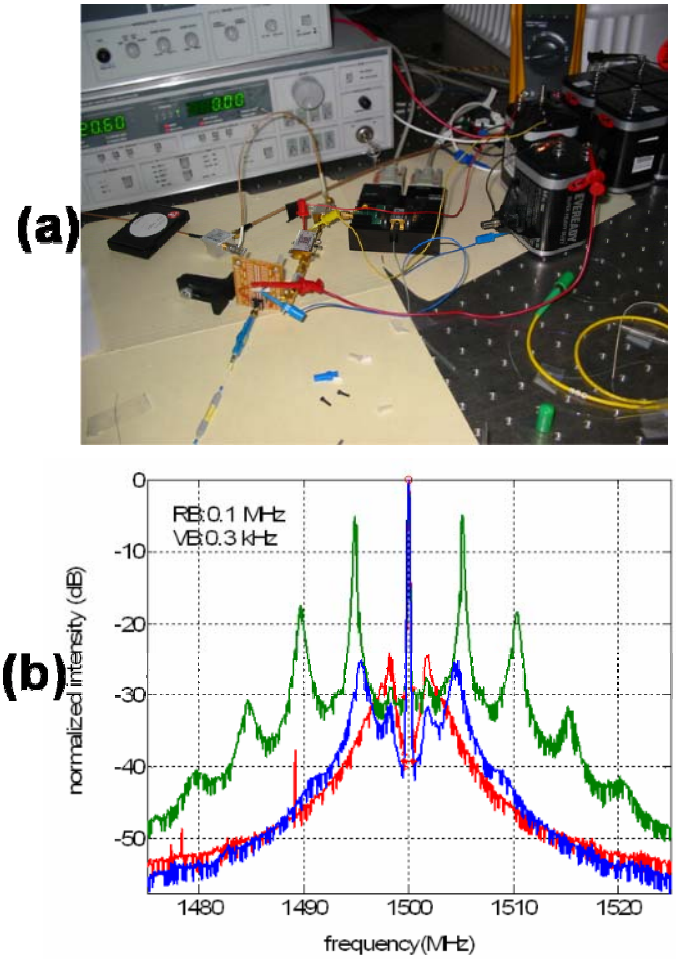

Fig. 3.7(a) A picture of the JDSU OPLL experimental setup. (b) Measured spectra of the locked beat signal of the JDSU OPLL for different loop gains.

Fig. 3.7(a) shows a picture of the actual JDSU OPLL setup. Fig. 3.7(b) shows the measured power spectra of the locked beat signal between the master laser and the slave laser for different loop gains. The red line corresponds to a low loop gain. As the loop gain is increased and the gain margin is reduced(the blue line), the frequency of the residual phase noise peak is pushed to a higher frequency. When the gain is further increased(the green line), one starts seeing the higher order side bands of the noise peak, which indicates significant ringing effect in the loop. This trend agrees with the theoretical calculation shown in Fig. 2.5. As I have pointed out in Section 2.3.3, as the gain margin approaches 0dB, the system starts oscillating at f_π. Hence the frequency difference between the central carrier and the first order noise peak in the ringing case is a good estimate of the π phase lag frequency f_π of the OPLL. In Fig. 3.7(b) f_π is about 5 MHz, which agrees with the theoretical prediction based on the measured FM response of the slave laser and the estimated loop delay.

3.2.2 Estimation of the residual differential phase error

In Section 2.5. I have pointed out the residual differential phase error is an important metric for evaluating the quality of an OPLL. Based on the measured power spectrum of the locked beat signal, one can calculate the root-mean-square (rms) differential phase error.

Assume the locked beat signal takes the form of

$$E = E_0 \cos\left(\omega_{rf} t + \phi_n\right) \tag{3.48}$$

where ω_{rf} is the frequency of the RF offset signal. When the two lasers are locked, the phase noise ϕ_n is bounded. Assuming $\phi_n << 1$, one can expand Eq. (3.48) to

$$E \approx E_0[\cos\omega_{rf} t - \sin\omega_{rf} t \cdot \phi_n] \tag{3.49}$$

The first term is a pure tone at the frequency of ω_{rf} which gives the central carrier

signal in the power spectra shown in Fig. 3.7(b). By averaging the square of the electric field over a time scale much longer than the period of the signal, one obtains the power of the signal as $P_s \sim E_0^2$. The second term in Eq. (3.49) leads to the double side noise shoulder seen in Fig. 3.7(b) when there is no significant ringing effect. Use the same argument described above, the power of the second term in Eq. (3.49) is $P_n \sim E_0^2 \overline{\phi}_n^2$, which can be calculated by integrating the double side power spectral density excluding the central carrier. From the ratio between the noise power and the carrier power one can estimate the rms differential phase error

$$\bar{\sigma} = \sqrt{\overline{\phi}_n^2} = \sqrt{P_n / P_s} \tag{3.50}$$

In Fig. 3.7(b), the rms phase error of the blue curve is about 0.32 *rad*.

3.2.3 Phase lock of the QPC MOPAs

Based on the same OPLL scheme, I also phase locked a QPC semiconductor Master-Oscillator-Power-Amplifier (MOPA) laser to the Agilent tunable laser. The MOPA is soldered on a C-mount, which is mounted on a copper block for heat dissipation. The MOPA is temperature controlled and operated with bias currents of 485 mA and 4 A, for the oscillator section and the amplifier section respectively. The wavelength of the MOPA is 1548nm and the output power is ~1W. The measured linewidth is less than 1MHz. The beam of the MOPA diverges in free space and part of the optical power is collected using a cleaved single mode fiber and then combined with the reference optical signal using a 3dB optical fiber coupler. The resulting phase error signal is injected into the oscillator section to modulate the optical frequency. Fig. 3.8(a) gives a picture of the actual setup and Fig. 3.8(b) displays the measured spectrum of the locked beat signal. The differential phase error between the slave laser and the master laser is calculated with Eq. (3.50) to be about 0.3 *rad*.

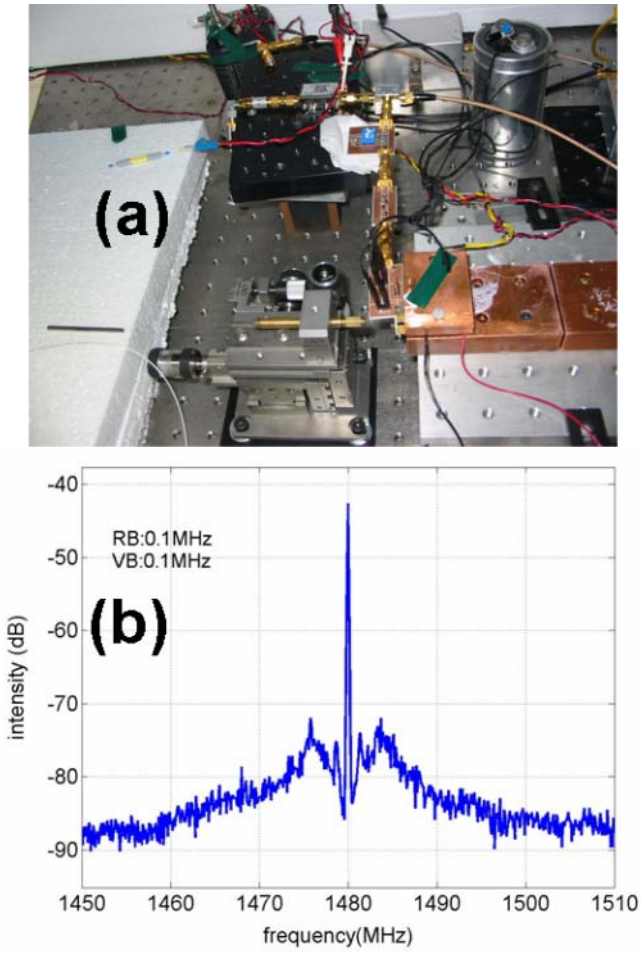

Fig. 3.8 (a) A picture of the QPC OPLL experimental setup. (b) Measured spectrum of the locked beat signal.

3.2.4 Phase lock of IPS external cavity lasers

I also phase-locked 75mW 1064nm external cavity SCLs (Innovative Photonic Solutions) with a 3 dB FWHM linewidth of 0.5 MHz. The reference laser is a spectrally stabilized NP Photonics fiber laser with a 3dB FWHM linewidth of 2.5 kHz. Fig. 3.9 gives the spectrum of the locked beat signal. A compensation filter with the lag-lead property at low frequency and the lead-lag property at frequency close to the f_π is used, and the rms differential phase error is about 0.13 *rad*. The topic of the compensation filter will be discussed in detail in the next section.

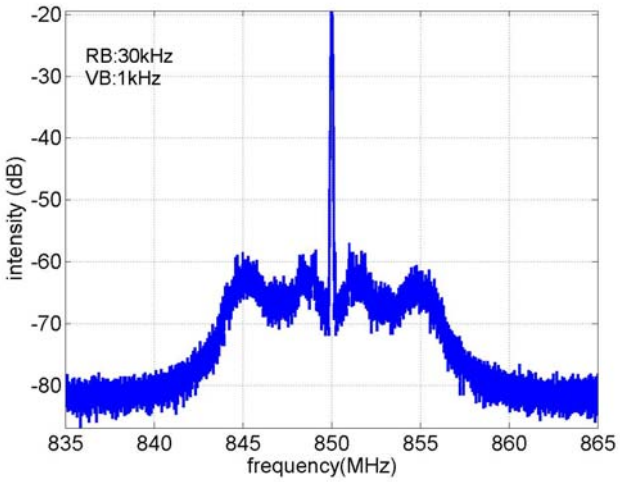

Fig. 3.9 Measured spectrum of the locked beat signal of the IPS OPLL.

3.3 Optimization with the compensation circuits

In Chapter 2 I pointed out that the loop bandwidth is limited by the non-uniform FM response of SCLs and the loop delay. This results in a number of critical issues, besides the non-negligible residual phase error. For example, the acquisition range and the holding range, which are proportional to the loop DC gain for the first-order PLL, are only a few MHz in the OPLLs I built. Upon being turned on, the frequency of the beat signal has to be manually tuned to be within ~10MHz from the frequency of the RF reference signal for the loop to acquire lock. In addition, the frequency of the SCLs jitters for tens of MHz within a few seconds, and hundreds of MHz over the long term, due to thermal fluctuations, current source noise, and acoustic noise. When the holding range is small the frequency jitter of the SCLs constantly throws the loop out of lock. All these issues can be partially solved by using certain compensation circuits. In this section I will study the use of three types of compensation circuits: the phase lead-lag filter, the lag-lead filter, and the aided-acquisition circuit.

3.3.1 Lead-lag filter to increase the phase margin

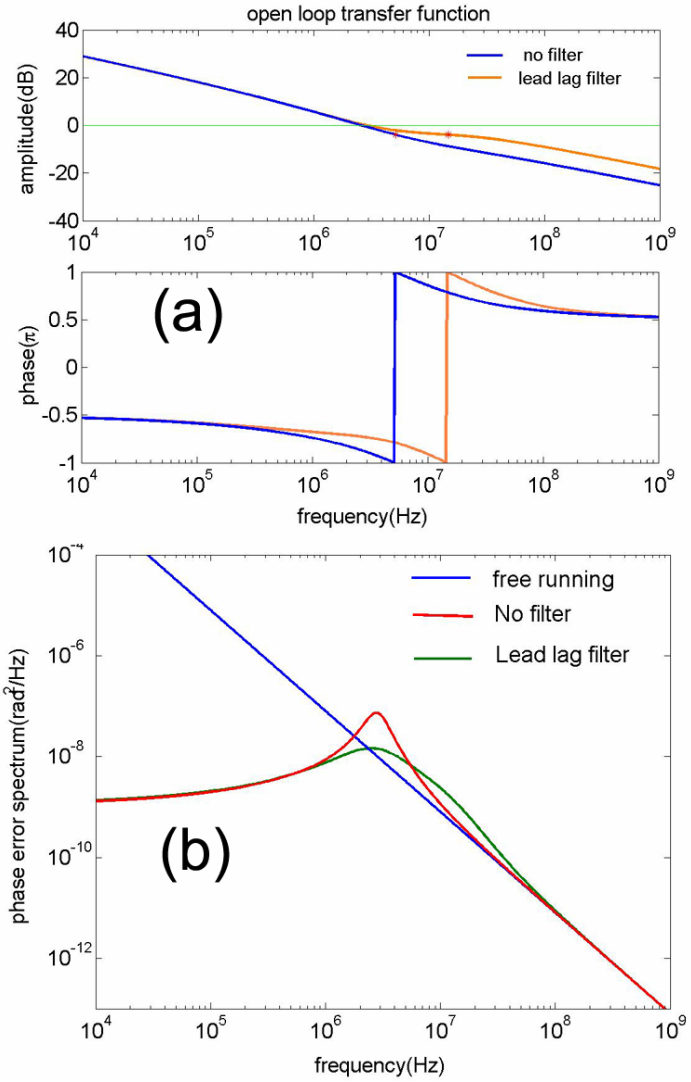

Fig. 3.10(a) Open loop transfer function of the JDSU OPLL with and without a lead-lag filter. (b). Corresponding power spectral density of the differential phase error. The FM response of the slave laser is described by Eq. (3.47) with b = 2.6, f_c = 1MHz. The transfer function of the filter is $F = (1+\tau_2 s)/(1+\tau_1 s)$ with $\tau_1 = 8ns$ and $\tau_2 = 40ns$.

As can be seen, the π phase lag frequency f_π is limited to a few MHz, due mainly to the phase lag given by the non-uniform FM response of the laser. Phase lead-lag filters can be used to increase f_π. The transfer function of a lead-lag filter is

$$F = \frac{1+\tau_2 s}{1+\tau_1 s}, \quad \tau_2 > \tau_1 \tag{3.51}$$

Eq. (3.51) can be included into the OPLL open loop transfer function to evaluate its influence. In Fig. 3.10(a) I compare the open loop transfer function with and without a lead-lag filter. In the calculation I use the FM response of the slave laser described by Eq. (3.47) and the parameters b = 2.6, f_c = 1MHz. The parameters of the lead-lag filter are $\tau_1 = 8ns$ and $\tau_2 = 40ns$. With the lead-lag filter f_π is increased from 5MHz to 14MHz. However this comes at the cost of reduced gain margin because the lead-lag filter raises the loop gain at high frequency. This can be seen in Fig. 3.10(a). The amplitudes of the blue (no filter) and the orange (with the lead-lag filter) lines are the same at low frequency. The amplitude of the orange line rises above the blue line at higher frequency. In Fig. 3.10(b) I also compare the power spectral density of the differential phase error without and with a lead-lag filter. On the diagram, the spectral peak at the frequency close to f_π is suppressed and broadened with the filter.

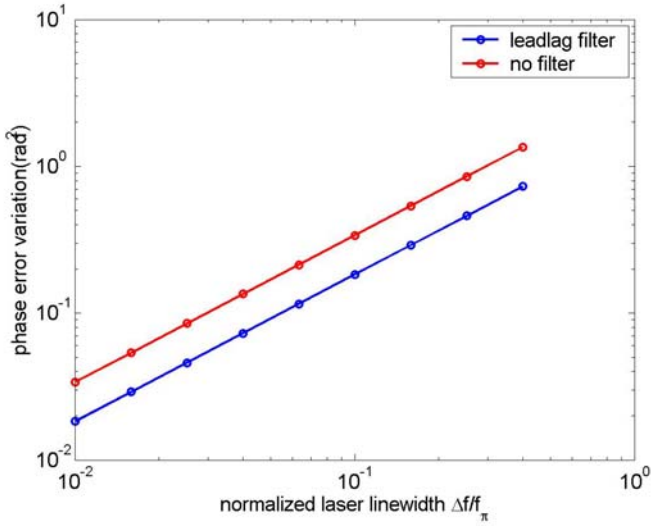

Fig. 3.11 The variance of the differential phase error as a function of the summed linewidth of the lasers Δf normalized by the π phase lag frequency f_π, with and without a lead-lag filter.

I further calculate and compare the variance of the differential phase error as a function of the normalized linewidth $\Delta f / f_\pi$ with and without a lead-lag filter. The results are plotted in Fig. 3.11. With the lead-lag filter the variance of the differential phase error can be reduced by almost a factor of 2.

Experimental demonstration

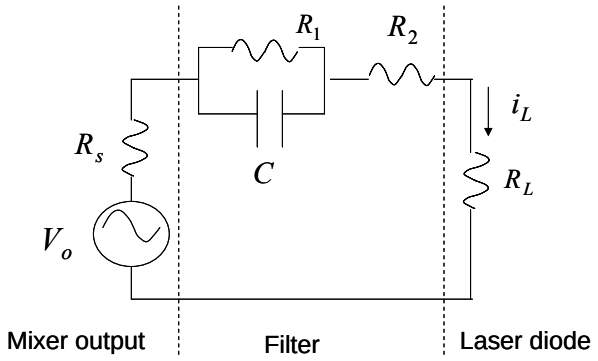

Fig. 3.12 Schematic diagram of the feedback circuit with a lead-lag filter

I have implemented a lead-lag filter in the JDSU OPLL and the circuit diagram is shown in Fig. 3.12. The mixer is modeled as a voltage source V_0 with the internal impedance R_s. The phase error voltage signal is filtered and converted to the current feedback signal i_L and sent into the laser diode R_L. A straightforward calculation leads to

$$i_L = \frac{V_o}{R_L + R_2 + R_1 + R_s} \frac{1+\tau_2 s}{1+\tau_1 s}, \tag{3.52}$$

where $\tau_1 = R_1 \left(R_L + R_s + R_2 \right) C / \left(R_L + R_s + R_1 + R_2 \right)$, $\tau_2 = R_1 C$. All the parameters are defined in Fig. 3.12.

The filter is implemented with the parameters $R_1 = 430\Omega$, $R_2 = 7.3\Omega$, and $C = 100 pF$. Impedance of the laser diode is $R_L \approx 3\Omega$ and impedance of the mixer is $R_s = 50\Omega$. Using these numbers I obtain the time constants $\tau_1 = 5.3 \times 10^{-9} s$ and

$\tau_2 = 4.3\times10^{-8} s$. With the same fitting parameters used in obtaining Fig. 3.3, one finds that the π phase lag frequency f_π is increased from 4.3 MHz to 11MHz with the filter.

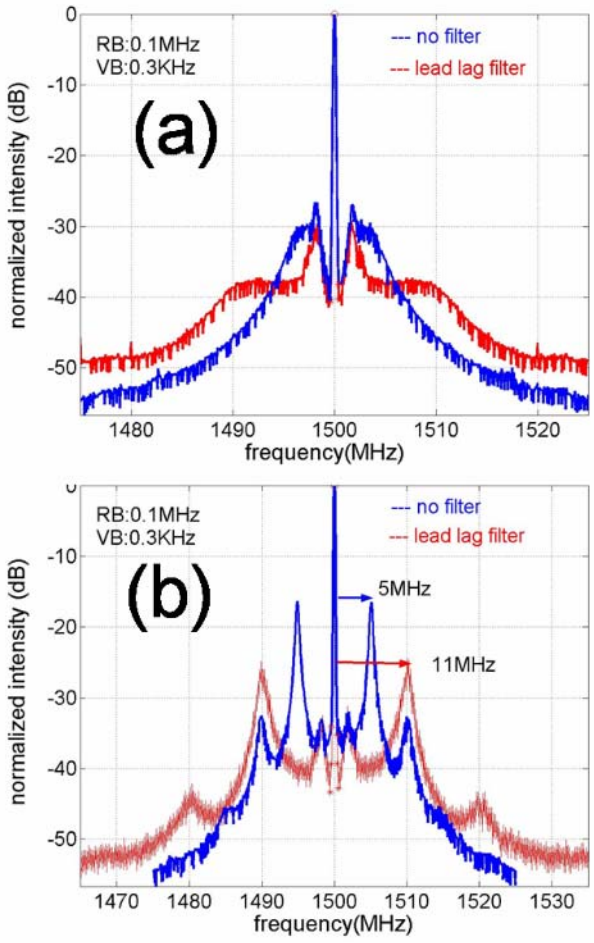

Fig. 3.13 Measured spectra of the locked beat signal of the JDSU OPLL without and with a lead-lag filter. The loop gain is increased in (b) such that the π phase lag frequency f_π can be estimated from the ringing frequency.

Fig. 3.13 is a comparison of the measured spectra of the locked beat signal with and without the lead-lag filter. In Fig. 3.13(a) one can see the noise shoulder is suppressed and broadened as predicted in Fig. 3.10(b). By integrating the double-sided noise power

spectral density, the variance of the phase noise is found to be reduced from 0.081 rad^2 to 0.053 rad^2. I further increase the loop gain until the ringing effect appears and the loop is close to oscillation, as indicated by the multiple side peaks shown in Fig. 3.13(b). The frequency difference between the central carrier and the first side peak gives a good estimate of f_π, which is increased from 5MHz to 11MHz as predicted by theory.

3.3.2 Passive lag-lead filter to increase the holding range

The frequency of SCLs strongly depends on the bias current and the temperature. E.g., the JDSU DFB laser has a current-frequency tuning sensitivity of ~500MHz/mA and a temperature-frequency tuning sensitivity of ~10GHz/C. Even with a high accuracy TEC controller and a low noise current source, I have seen that the frequency of the laser jitters by tens of MHz within a few seconds, and hundreds of MHz over tens of minutes. For external cavity SCLs, the frequency is also very sensitive to acoustic perturbation. The frequency jitter due to the current and temperature variation can throw the loop out of lock frequently, since the holding range is typically ~10MHz. In the experiment, the JDSU OPLL typically stays in lock for about 10 seconds without using a compensation filter.

In Section 2.2 I have also pointed out that the steady state differential phase error relies on the free-running frequency difference between the lasers normalized by the loop DC gain, i.e., $\Phi_{e0} = \Delta\omega / K_{dc}$. And the small signal loop gain $K'_{dc} = K_{dc}\cos\Phi_{e0}$ relates to $\Delta\omega$ through Φ_{e0}. Even when the loop stays in lock, the frequency jitter changes the steady state differential phase error Φ_{e0} and the small signal loop gain, events which should be avoided or minimized.

The frequency of SCLs can be stabilized to a very high degree by frequency locking to a stable frequency reference. The frequency reference could be a stabilized Fabry-Perot cavity[40, 41] or the absorption line of certain molecules[42]. However these solutions

require complicated systems and the advantages of SCLs, such as their small size and low cost, are lost. Also limited are the choices of molecules' absorption lines, to which the SCLs can be locked. Here I study a more attractive solution, i.e., the use of the lag-lead filter to compensate for the frequency jitter of the SCLs.

In a PLL, the acquisition range Δf_{acq} depends on the detailed shape of the open loop transfer function, and the holding range Δf_h is mainly determined by the loop DC gain $\Delta f_h = K_{dc}/2\pi$ [1]. In a practical OPLL, the loop gain is limited by the stability criterion $G_{op}(f_\pi) < 1$ and f_π is usually limited to a few MHz, due to the non-uniform FM response of SCLs and the loop delay. If one increase the loop gain only at frequencies lower than f_π and do not reduce the gain margin at f_π, the stability criterion is still maintained while the holding range Δf_h is increased. This can be achieved using a lag-lead filter. The transfer function of a lag-lead filter can be described by

$$F(s) = \frac{1+\tau_2 s}{1+\tau_1 s}, \quad \tau_1 > \tau_2 \tag{3.53}$$

Fig. 3.14(a) shows the Bode plot of a typical lag-lead filter. The filter has high gain at low frequency and reduced gain at higher frequency. In Fig. 3.14(b) I compare the open loop transfer function of the JDSU OPLL without and with a lag-lead filter. The open loop gain at low frequency, and the resulting holding range is enhanced by a factor of τ_1/τ_2. A theoretical study has demonstrated that the acquisition range can also be enhanced by approximately $\sqrt{2\tau_1/\tau_2}$ [1]. The benefit, however, comes at the cost of a reduced phase margin at the intermediate frequency($10^4 \sim 10^5 Hz$ in Fig. 3.14(b)) due to the phase lag property of the filter. Hence, care must be taken while picking the time constants τ_1 and τ_2 to maintain sufficient phase margin and avoid loop instability. In

addition, the frequency range of the phase lag induced by the filter should be kept far away from the f_π without affecting it.

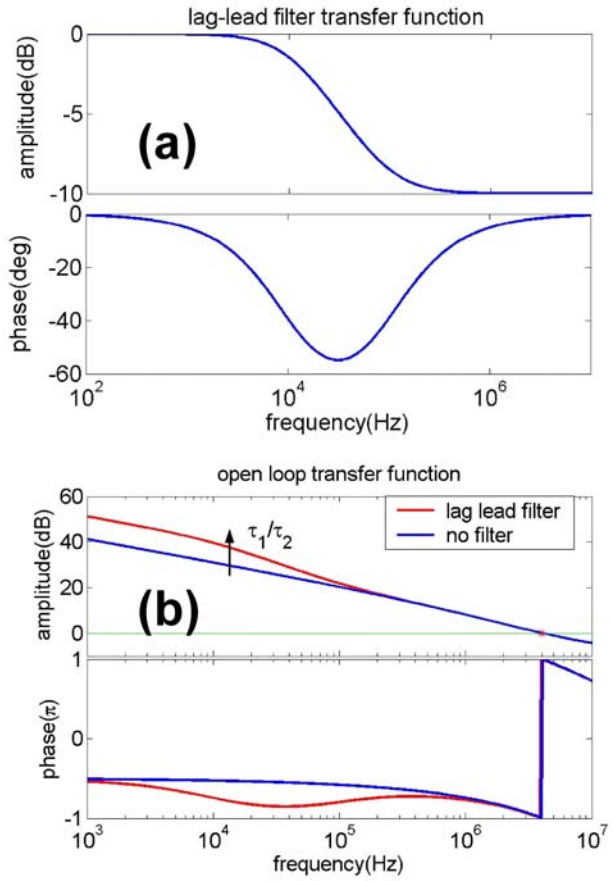

Fig. 3.14 (a) Transfer function of a lag-lead filter. (b). The open loop transfer function of the JDSU OPLL without and with a lag-lead filter. Eq. (3.47) and the parameters b = 2.6, f_c = 1MHz are used in the calculation. The transfer function of the filter is $F = (1+\tau_2 s)/(1+\tau_1 s)$ with $\tau_1 = 124\mu s$ and $\tau_2 = 6\mu s$

Experimental result

I have implemented a passive lag-lead filter illustrated in Fig. 3.15. With the parameters defined in Fig. 3.15, the feedback current is given by

$$i_L = \frac{V_o}{R_L + R_3 + R_1 + R_s}\frac{1+\tau_2 s}{1+\tau_1 s} \tag{3.54}$$

where $\tau_1 = \left[R_2 + \left(R_L + R_3 \right) \left(R_s + R_1 \right) / \left(R_L + R_3 + R_s + R \right) \right] C$ and $\tau_2 = R_2 C$. Two sets of lag-lead filter parameters were tried in the JDSU OPLL and the results are listed in table 3.1. The holding range is increased by ~6 times with filter 1 and ~16 times with filter 2. If one assumes that the frequency jitter is a random walk process, if the holding range is increased by a factor of τ_1 / τ_2, the average time required for the frequency jitter to exceed the holding range should increase by a factor of $\left(\tau_1 / \tau_2 \right)^2$. In the experiment I observed that the locking duration is increased from ~10 seconds to hours. I also implemented the lag-lead filters in the IPS OPLL and successfully increased the holding range from ~±10MHz to ±200MHz.

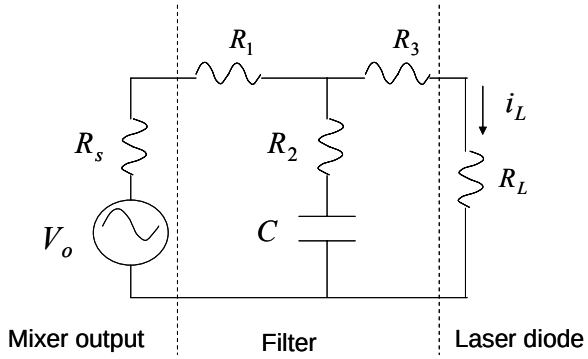

Fig. 3.15 Schematic diagram of the lag-lead filter circuit

Table 3.1 Measured single-side holding range and acquisition range of the JDSU OPLL with the lag-lead filters.

	holding range (MHz)	acquisition range (MHz)
no filter:	8 ~ 10	6 ~ 8
filter 1	50 ~ 60	~ 17
filter2	130 ~ 180	~ 30

Further increase of the holding range with the passive lag-lead filter will be

ultimately limited by the current driving capability of the RF mixer, since it is the mixer that provides the feedback current to hold the slave laser in lock. For a typical level7 mixer (e.g., the minicircuits zx05-C24), the maximum output current is about +/-2mA, which translates to a holding range of a few hundred MHz to 1GHz, depending on the current FM sensitivity of the laser. To further increase the holding range, an active filter must be used.

3.3.3 Active lag-lead filter to increase the holding range

A second-order active filter can potentially provide a current of tens of mA and thus provide a holding range of multiple GHz. It can also provide excellent low frequency noise reduction since the loop gain is significantly enhanced at low frequency. Fig. 3.16(a) is the circuit diagram of a second-order active filter with the transfer function $F(s)=(1+\tau_2 s)/\tau_1 s$. Since it is an all-pass filter for signals from DC to very high frequency, it requires a very high speed Operational amplifier(Op-Amp) with a flat phase response.

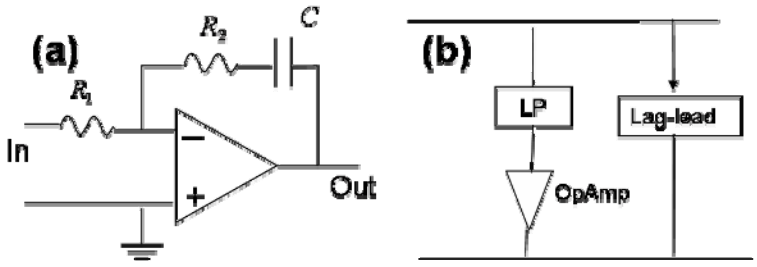

OpAmp: operational amplifier

Fig. 3.16 (a) Schematic diagram of a second-order active filter. (b) Schematic diagram of an active lag-lead filter.

I take a different approach to address the problem. Another active feedback path can be added in addition to the passive feedback path to increase the feedback current and the

loop gain at low frequency. Fig. 3.16(b) is a schematic diagram of the dual-path filter. The passive path could be the typical passive lag-lead filter I have discussed. The active path is made of a low-pass filter followed by an Op-Amp.

To analyze the total effect of this filter, one can add the transfer functions of the dual feedback paths

$$F_{tot}(s) = F_1(s) + F_2(s)A \tag{3.55}$$

where $F_1(s)$, $F_2(s)$, and A represent, respectively, the transfer function of the passive feedback path, the filter in the active feedback path, and the Op-Amp gain. For the sake of simplicity, I assume that $F_1(s) = 1$, and $F_2(s)$ is a low-pass filter described by $F_2(s) = 1/(1 + s/\omega_c)$. The gain A>>1 is a constant for frequency much lower than the bandwidth of the OpAmp. Then Eq. (3.55) becomes

$$F_{tot}(s) \approx A\frac{1 + s/A\omega_c}{1 + s/\omega_c} \tag{3.56}$$

Eq. (3.56) is essentially the transfer function of a lag-lead filter (Eq. (3.53)) except for a constant gain factor A. The advantage of this active filter design is the elimination of the need of a high speed Op-Amp. A slow and low noise Op-Amp is ideal for building this active lag-lead filter. A typical Op-Amp can easily drive 10~100mA current, which is equivalent to a holding range of multiple GHz.

An example of such an active lag-lead filter is realized and tested in an OPLL made of an external cavity laser. The schematic diagram of the circuit is given in Fig. 3.17. The OPLL has an initial holding range of around +/-50MHz. The current FM sensitivity of the laser is about 150MHz/mA. A passive lag-lead filter is first implemented to increase the holding range to ~+/-300MHz. This corresponds to ~+/-2mA current output of the RF mixer. I then add the parallel active feedback path. This filter first detects the voltage signal from a resistor in the passive lag-lead filter. The voltage signal is amplified by a differential amplifier with a gain of 40 times and filtered by a low-pass filter. A second

stage Op-Amp with adjustable gain followed by a voltage-to-current conversion circuit is then used to further amplify the signal and convert it into current feedback signal. The cutoff frequency of the low-pass filter is 8Hz. The maximum gain of this active feedback path is about 20, which in theory should increase the holding range from +/-300MHz to +/-6GHz. With this filter, I can change the laser diode bias current by +/-30mA without losing lock, which indicates the holding range is +/-4.5GHz.

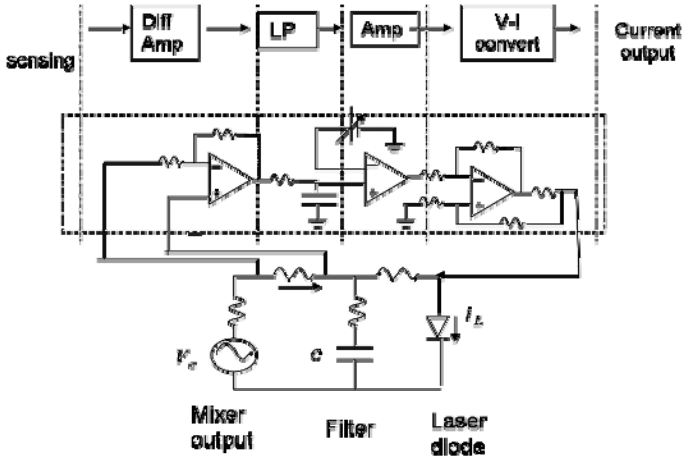

Fig. 3.17 Circuit diagram of the active lag-lead filter

If even higher holding range is desired, I can feed the current signal of the active path into the TEC controller to temperature-modulate the frequency. Due to the very high temperature FM sensitivity of SCLs, this should potentially increase the holding range by orders of magnitude. Another possible benefit of the temperature modulation is that it avoids the intensity variation caused by the feedback current modulation.

3.3.4 Aided-acquisition circuit to increase the acquisition range

So far I have discussed the use of different filters to compensate for the holding range. However the acquisition range can not be improved significantly with the lag-lead filter. To bring the laser in lock automatically upon being powered on, an aided acquisition circuit can be used. This circuit also automatically bringd the laser back to lock if the loop loses lock occasionally.

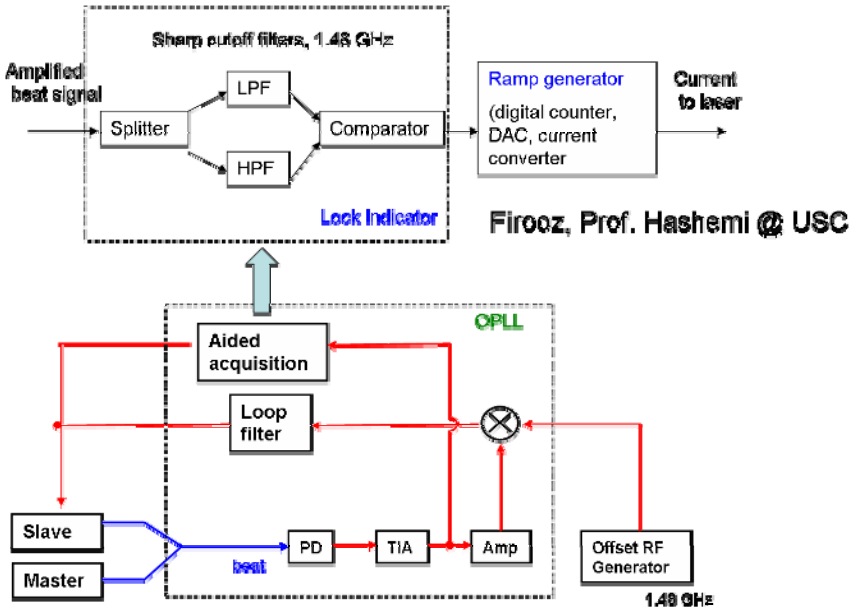

Fig. 3.18 Schematic diagram of an aided-acquisition circuit

Fig. 3.18 is a schematic diagram of an aided acquisition circuit designed and built by Firooz Aflatouni and Prof. Hossein Hashemi at USC. This circuit splits the beat signal and feeds it into a sharp low-pass filter and a high-pass filter. By comparing the output of the two filters, the circuit decides whether the frequency of the beat signal is smaller or larger than the frequency of the RF offset signal, and generates a current ramp which brings the frequency of the beat signal to be within the acquisition range of the OPLL [43]. The AAC is tested on both the QPC OPLL and the IPS OPLL. The acquisition range is increased from ±10MHz to ±1.1GHz.

3.4 Conclusion

I have successfully phase locked various commercial SCLs. The loop performance is mainly limited by the non-uniform FM response of the SCLs and the loop delay. With the use of compensation filters, the acquisition range and holding range are significantly increased. A locking efficiency of above 90% and a locking time of a few hours have been achieved. Although discrete components have been used in all the experiments demonstrated in this chapter, an integrated circuits having the function of the locking

circuits including the RF mixer, the RF amplifier, and the compensation filters can be designed and used to significantly reduce the system's dimension and cost. Research in this direction is currently being carried out by Firooz Aflatouni and Prof. Hossein Hashemi at USC.

Starting with the next chapter, I will study the applications of OPLLs, particularly in coherent beam combining and coherence cloning.

Chapter 4 Application of OPLLs in coherent beam combining

4.1 Introduction of coherent beam combining

4.1.1 Spectral beam combining vs coherent beam combining

High power, high brightness lasers with diffraction limited beam quality have been sought since the earliest days of laser technology. Today, high power gas lasers, solid state lasers and fiber lasers are able to output thousands of watts of light under continuous-wave operation. Further increase of the power will be limited by thermo-optic effects, nonlinear effects, and material damage. A promising solution to these challenges is to use beam combining techniques, meaning to combine the outputs of a number of lasers or amplifiers to obtain a single output. The goal of beam combining is not only to scale the power, but also the brightness. For this purpose the beam quality needs to be preserved. Semiconductor lasers and fiber amplifiers have attractive attributes for beam combining because of their ease in building array formats, their high efficiency, and their ability to get near diffraction-limited beams from the individual elements[44-49]. There are generally two classes of beam combining with increased brightness: spectral beam combining (SBC)[44, 49, 50] and coherent beam combining (CBC)[25, 27, 29, 51].

CBC combines an array of element beams with the same frequency and controlled relative phases such that there is constructive interference. This is analogous to phased-array transmitters in the radio-frequency (RF) and microwave portions of the electromagnetic spectrum, but in the optical domain. Beam steering by controlling the relative phase of each element beam is also possible with CBC. However CBC has proven to be difficult because of the shortness of the optical wavelength and the requirement that the phases of the array elements be controlled to a small fraction of a wavelength.

The general principle of SBC is to have several beams with non-overlapping optical

spectra and cto ombine them at some kind of wavelength-sensitive beam combiner such as a prism, a diffraction grating, a dichroic mirror, or a volume Bragg grating, which can deflect incident beams according to their wavelengths so that afterwards these all propagate in the same direction. To combine the outputs of a large number of lasers, one requires that each laser must have high wavelength stability and the beam combiner must have sufficient dispersion. Compared with CBC, SBC has the advantage of not requiring the mutual temporal coherence of the combined beams. This eliminates some important technical challenges and makes it much easier to obtain stable operation at high power levels.

4.1.2 Tiled-aperture and filled-aperture CBC

CBC is of interest, however, for applications requiring both high power and narrow spectrum. There are a few excellent reviews of CBC systems[45-48]. Depending on the combining implementation, CBC can be subdivided into tiled-aperture approach (side-by-side combining leading to a larger beam size but reduced divergence), and filled-aperture approach (where several beams are combined to a single beam with the same beam size and divergence, using e.g. beam splitters). The function of beam steering can only be realized with the tiled-aperture approach.

As an example of the side-by-side tiled-aperture combining, consider four beams with top-hat intensity profiles of rectangular cross section and flat phase profiles. One may arrange these profiles to obtain a single beam with two times the dimensions, or four times the area, and of course four times the power. If the beams are all monochromatic and mutually coherent, and the relative phases are properly adjusted to obtain essentially plane wavefronts over the whole cross section, one obtains a beam divergence which is only half that of each single beam. As a result, the beam quality is preserved, and the brightness of the far field can be sixteen times that of each single beam. In practice, the top-hat beam profile is not easily obtainable, and the gaps between the individual beams

(i.e., the non-unity fill factor) together lead to side lobes in the far-field beam pattern and reduce the beam quality and brightness.

To understand the principle of the filled-aperture techniques, consider a beam splitter with 50% reflectivity. Overlapping two input beams at this beam splitter will in general lead to two outputs, but one can obtain a single output if the two beams are mutually coherent and adjusted so that there is destructive interference for one of the outputs. This technique makes it easier to preserve the beam quality and does not require special beam shapes, but it may be less convenient for large numbers of emitters, where a series of beam combining stages is required. If any one stage fails, the performance of the whole system degrades significantly.

In any case, the constructive interference plays the key role, and the mutual coherence of the combined beams is essential. Typically the room-mean-square(rms) relative phase deviations must be well below 1 rad[47, 52]. In addition, the mismatches of the amplitudes, polarizations, pointing and alignment of the element beams all contribute to the degradation of the beam combining efficiency and the beam quality, and need to be well managed.

4.1.3 Methods to Obtain Mutual Coherence

There are a variety of techniques to obtain mutual temporal coherence between the element beams, which are briefly summarized in the following:

- The phases of multiple lasers can be synchronized by some kind of optical coupling, such as evanescent wave or leaky-wave coupling[53-56]. This approach has been extensively used, particularly with laser diode arrays [56], where optical coupling can be obtained simply by placing the waveguides sufficiently close together. This may also be applied to multi-core optical fibers. In-phase coupling of the array elements is desired to obtain high on-axis far-field intensity. However,

the coupling is often predominantly out-of-phase, giving a power null on-axis. This can be attributed to the modal gain/loss discrimination. The out-of-phase coupling gives a null between the array elements that, compared with the in-phase coupling, leads to less loss if the space between the elements is lossy, and higher gain because of better spatial overlap of the mode with the gain region. Another issue is tolerance the phase error. While scaling to a large array of N elements, the degradation of the on-axis field intensity and beam quality increases with N^2 due to the nature of the correlated phase error between the array elements[52].

- The out-of-phase coupling problem is partially avoided in the common-resonator techniques, where the beams are fully combined at the output coupler, but split within the resonator (laser resonator) to be amplified in different gain elements [57-59]. To force the lowest order transverse-mode operation (corresponding to the in-phase coupling) an intracavity spatial filter can be used to select the mode. Though this approach has been successful at low power, it is difficult to obtain the lowest order transverse mode operation as power increases due to the thermally induced variation in the optical path length.
- Another extensively studied method of obtaining mutually coherent monochromatic beams is to use active-feedback, where the differential phases among the array elements are detected and then feedback is used to equalize the optical path lengths modulo 2π [25, 28, 60, 61]. This approach has been used in master-oscillator power-amplifier (MOPA) architectures, where a single-frequency laser output is split and amplified, e.g., by high power fiber amplifiers, whose outputs are combined. It has also been used in optical injection locking architecture, where the optical power of a master laser is used to injection-lock an array of slave lasers, whose outputs are amplified by fiber amplifiers and then combined. In both cases the key issues are the detection of the differences in optical path length and the design of a phase control servo system

with sufficient bandwidth and dynamic range to correct for these variations. For example, one can adjust the pump power of each amplifier or use an optical phase modulator, a fiber stretcher, or an acoustic optical modulator in front of each amplifier input to adjust the phase of each element beam. The resulting phase-coherent beams can be combined with either the filled-aperture approach or the tiled-aperture approach.

The CBC system I am going to discuss in this thesis falls into the last category, the active feedback control. We propose that mutual coherence between the element beams be established by locking an array of slave lasers to one master laser using OPLLs. Following each slave laser, a fiber amplifier can be used to increase the power. However, the differential phase between the outputs of the fiber amplifiers varies due to optical path length variation in the fiber, which needs to be corrected for. As I have pointed out in Chapter 2, in a heterodyne OPLL, the phase of the slave laser depends on the phase of the RF offset signal. Hence, a RF phase or frequency shifter, instead of an optical phase or frequency shifter, can be used to correct for the optical path length variation. The use of OPLLs thus eliminates the need for expensive and bulky optical phase modulators or acoustic optical modulators, and enables a full electronic phase control servo, which can significantly reduce the cost and size of the CBC system.

In this chapter, I present both the theoretical and the experimental study of the frequency/phase control of the element beams with multilevel OPLLs.

4.2 Synchronizing two SCLs with OPLLs

In Chapter3 I have demonstrated the phase locking of different commercial SCLs, including a 16dBm JDSU DFB laser at 1538nm, a 1W QPC master-oscillator-power -amplifier (MOPA) at 1548nm, and a 18dBm IPS external cavity laser at 1064nm. To demonstrate the idea of CBC with OPLLs, I combined two OPLLs in which the two slave

lasers are locked to the same master laser and have the same frequency.

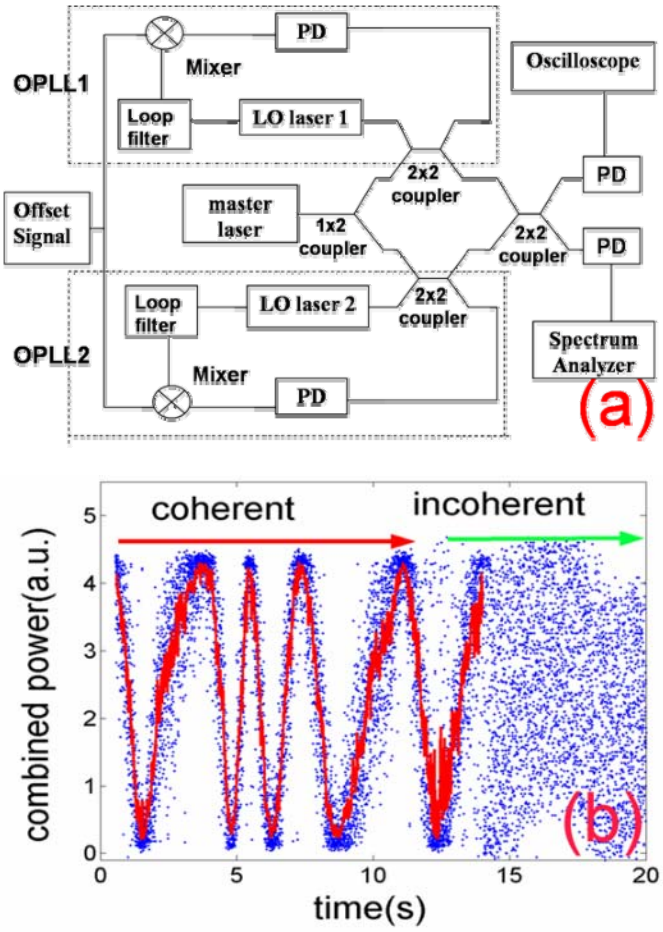

Fig. 4.1 (a) Schematic diagram of coherent beam combining of two SCLs locked to a common master laser. (b) Time domain measurement of the combined power. The blue dots are the measured data, the red solid line is the smoothed data.

Fig. 4.1(a) shows the schematic diagram of combining two OPLLs using the filled-aperture approach. OPLL1 and OPLL2 share the same master laser, which is an Agilent 81640A tunable laser, and the slave lasers are JDSU DFB lasers. The power of the master laser distributed to the OPLLs is typically -3dBm and could be reduced to -15dB since a RF amplifier can be used to compensate for the loop gain. A 1.48GHz RF offset signal provided by the HP 8565E signal generator is split and distributed to both OPLLs. The optical signals of the two slave lasers are combined with a 3dB fiber optical coupler. The locking status of the two OPLLs is monitored in the frequency domain with

the HP 8565E spectrum analyzer. The combined signal is detected by a photodetector whose output is displayed in the time domain(Fig. 4.1(b)) using a Tektronix TDS3052B oscilloscope. If one assumes that the amplitudes and the polarization of the two optical signals are matched, the combined power received by the photodetector is

$$P = 2I \cdot \left(1 + \cos\left(\Delta\omega \cdot t + \phi_e\right)\right) \tag{4.1}$$

where I stands for the power of the individual beams, $\Delta\omega$ is the frequency difference, and $\phi_e = \phi_2 - \phi_1$ is the differential phase error between the individual beams. ϕ_2 and ϕ_1 are, respectively, the phases of the signals of slave laser 2 and 1 at the combining point. When at least one of the two slave lasers is not locked to the master laser, the output of the photodetector is an AC signal (the right part of Fig. 4.1(b)) at the frequency $\Delta\omega$. The data appears as a scatter of points, since $\Delta\omega$ is in the MHz range while the time resolution of the oscilloscope is set at 2 seconds. When both the slave lasers are locked ($\Delta\omega = 0$), the individual beams have the same frequency and are coherently added. The output of the photodetector ideally consists of a DC signal which in our case varies slowly on the time scale of seconds as can be seen on the left part of Fig. 4.1(b). This slow variation reflects, as it should, the change of the difference in the optical path lengths experienced by the two individual optical signals due to the slow variation of temperature and environment. The spreading of the coherently combined signal reflects the residual differential phase noise in the OPLLs that I analyzed in Section 2.4. From the degree of scattering of the data I estimate that the rms differential phase error between the two individual signals is about 30 degrees. In Chapter3, based on the measured power spectrum of the locked beat signal, I have calculated that the rms differential phase error between the slave laser and the master laser in a single OPLL is about 19 degrees. Assuming the differential phase errors in two OPLLs are uncorrelated, the rms differential phase error between the two slave lasers should be approximately $\sqrt{2} \times 19 = 27$ degrees. Thus the rms phase error calculated from the frequency domain measurement agrees with that obtained from the time domain measurement.

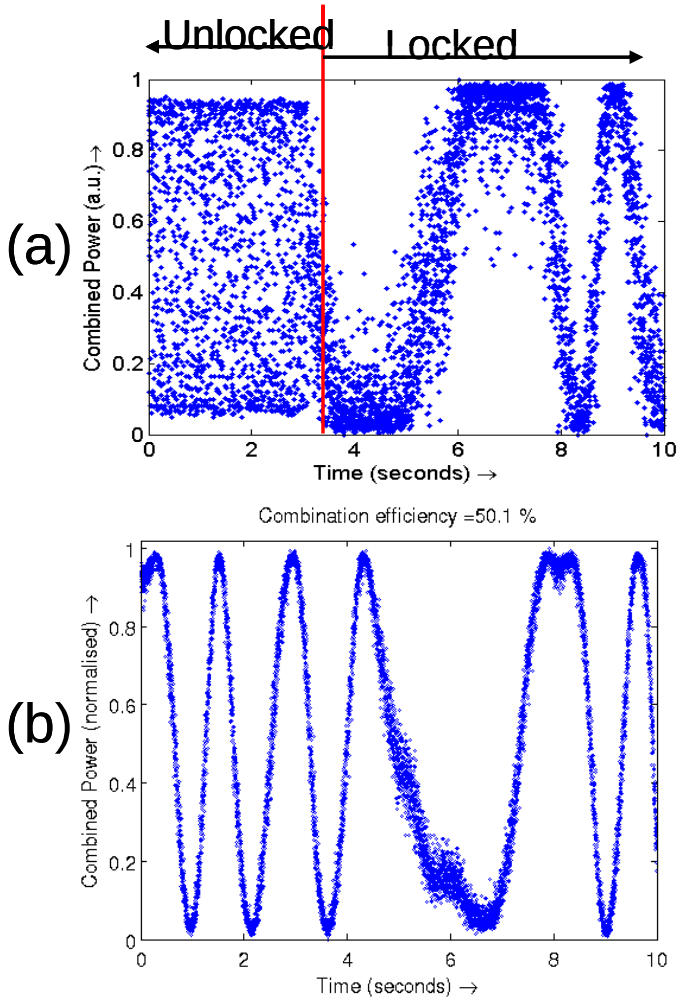

Fig. 4.2 Time domain measurement of the coherently combined power of (a) two QPC MOPAs, (b) two IPS external cavity SCLs

Based on the similar experimental scheme, I repeated the same experiment with the QPC MOPAs and the IPS external cavity SCLs. The Agilent tunable laser is still used as the master laser for the QPC MOPAs. A spectrally stabilized NP Photonics fiber laser with a 3 dB linewidth of 2.5 kHz is used as the master laser for the IPS lasers. The measured combined power in the time domain is shown Fig. 4.2. From the degree of scattering of the data, I estimate that the rms differential phase error between the two individual lasers is about 22 degrees for the QPC MOPAs and 10 degrees for the IPS lasers.

4.3 Correction for the optical path-length variation

Thus far, I have demonstrated the use of OPLLs to synchronize and combine two slave lasers. However one critical issue remains, i.e., the slow variation of the differential phase between the element beams due to the change of the optical path-length in the fibers. A servo system is required to detect this differential phase variation and correct for it. An optical phase shifter (phase modulator or Piezo fiber stretcher) or frequency shifter (an acoustic optical modulator) has previously been used as the phase actuator to correct for the differential phase variation[25, 62]. However these optical phase actuators are typically very expensive (a few thousand dollars each), bulky and can not handle very high optical powers. In the heterodyne OPLLs analyzed in Chapter 2, the phase of the slave laser follows the phase of the RF offset signal within the loop bandwidth. Thus a RF phase shifter can be used to correct for the optical path-length variation.

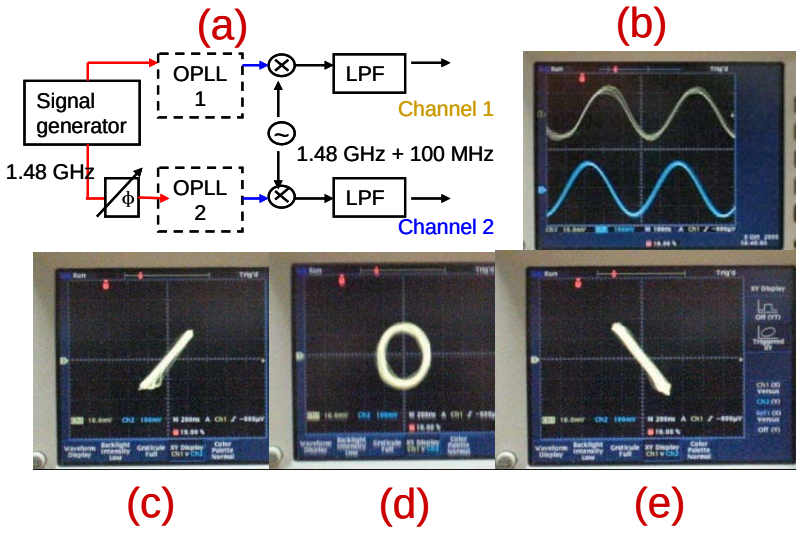

LPF: low pass filter

Fig. 4.3 (a) Schematic diagram of the phase control of the individual MOPA. (b) Comparison of the output waveforms of the two independent OPLLs. (c)-(d) Lissajou curves reflecting the control of the relative phase between the two OPLLs' output signals

4.3.1 Phase control using an RF phase shifter

Fig. 4.3(a) is a schematic diagram depicting the phase control of an individual QPC MOPA using a RF phase shifter. The HP signal generator is still used to provide the RF offset signals (1.48GHz) for the two OPLLs, however the RF signal sent to OPLL2 is now followed by a mechanical RF phase shifter. The beat signals between the master laser and the slave lasers in the two OPLLs are down-converted to 100MHz and the waveforms are compared on the oscilloscope (Fig. 4.3(b)). By adjusting the mechanical RF phase shifter, one can control the relative phase between the beat signals in the two OPLLs, as seen in the Lissajou curves of Fig. 4.3(c)-(e).

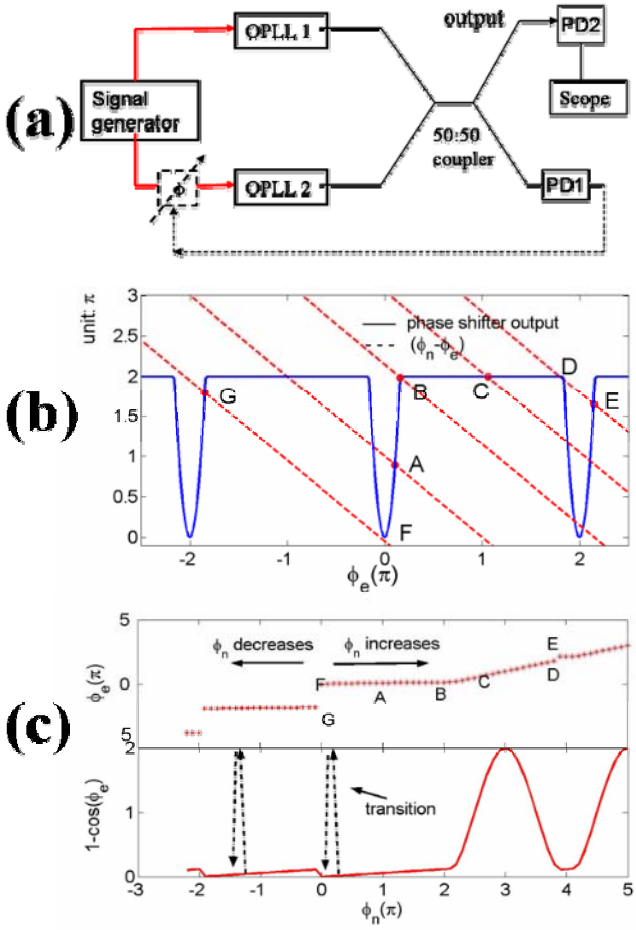

Fig. 4.4(a) Schematic diagram of combining two OPLLs with an additional RF phase shifter loop. (b) Graphic tools to find the steady-state solution of the RF phase shifter

feedback loop. (c) Steady state solution of the differential phase error ϕ_e between the combined individual beams as a function of the phase noise ϕ_n induced by the differential optical path-length variation. The solution depends on both the value and the history of ϕ_n.

Fig. 4.4(a) is a schematic diagram of the combining experiment with a RF phase shifter loop to correct for the optical path-length variation. The details of the OPLLs are given in Fig. 4.1(a) and thus not plotted here. In the filled-aperture scheme the combining element, which is a fiber coupler here, has two outputs. Our goal is to minimize one of the outputs and maximize the other output. The output we want to minimize is detected by a null detector (PD1 in Fig. 4.4(a)), whose output is fed back to the RF phase shifter. Assume the amplitudes, and polarization states of the two individual optical signals are matched, and that their phase difference is $\phi_e(t)$, the output of the null detector is proportional to $1-\cos\phi_e(t)$. Our goal is to maintain $\phi_e(t)$ as close to zero as possible. This signal is amplified and applied to the phase shifter. The resulting phase change of the RF offset signal seen by OPLL2 is

$$f(\phi_e) = G(1-\cos\phi_e), \quad 0 \le f(\phi_e) \le 2\pi \tag{4.2}$$

where *G* is the phase shifter loop gain, and the phase shifter's dynamic range is from 0 to 2π. Note in Eq. (2.4) of Section 2.2, the phase of the slave laser is inversely related to the phase of the RF offset signal by $\phi_s \sim -\phi_r$. Therefore the phase of the slave laser changes by $-f(\phi_e)$ when the phase of the RF offset signal is changed by $f(\phi_e)$. If the differential optical path-length in the fiber varies by $\phi_n(t)$, the differential phase error between the combined individual beams satisfies

$$\phi_e = \phi_2 - \phi_1 = -f(\phi_e) + \phi_n \tag{4.3}$$

Eq. (4.3) can be solved graphically as illustrated in Fig. 4.4(b). I have assumed that the phase change given by the phase shifter is limited from 0 to 2π and the loop gain is 50. Eq. (4.3) is modified to the form $f(\phi_e) = \phi_n - \phi_e$. The blue solid line in Fig. 4.4(b) represents the RF phase shifter output $f(\phi_e)$, the groups of dashed lines represent $\phi_n - \phi_e$ for different values of ϕ_n. The point of intersection between the blue line and a dashed line satisfies Eq. (4.3) for the particular value of ϕ_n. Two critical issues of this servo system can be deduced from Fig. 4.4(b): First, the limited dynamic range requires a complicated phase unwrapping circuit to control the RF phase shifter once it saturates, e.g., as ϕ_n increases from point F to B, the phase shifter is tracking ϕ_n and ϕ_e is kept small. At the saturation point B, if ϕ_n continues to increase, ϕ_e will increase linearly with ϕ_n and a phase unwrapping circuit is necessary to bring the steady state back to point F. The second issue is that of cycle slips. A small reduction in ϕ_n moves the locking point from point F to G and the loop experiences a cycle slip. In Fig. 4.4(c) I plot the trace of the differential phase error ϕ_e as a function of the fiber path-length variation induced phase noise ϕ_n. If ϕ_n increases monotonously, the phase shifter loop stops tracking after ϕ_n exceeds its dynamic range. If ϕ_n decreases monotonously, frequent cycle slips are expected. A combination of tracking, loss of tracking and cycle slips will be expected in practice, since ϕ_n varies randomly. I performed the CBC experiment with a phase shifter using the IPS lasers, without a phase unwrapping circuit. Fig. 4.5 shows the combined signal measured on the oscilloscope. Comparing this to the result shown in Fig. 4.2(b), one can see that the servo system works only when the phase shifter operates within its dynamic range and is not saturated.

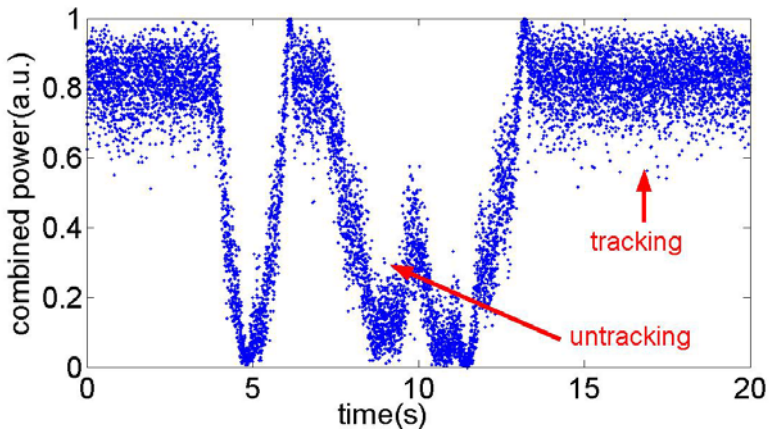

Fig. 4.5 Coherently combined power of two IPS lasers with the servo system made of a RF phase shifter feedback loop without the use of an unwrapping circuit (Fig. 4.4(a))

The issue of the limited dynamic range can be solved by replacing the phase shifter with a frequency shifter, e.g., a voltage-controlled oscillator (VCO), which acts as an integrating phase shifter and has infinite dynamic range.

4.3.2 Phase control using an RF VCO

Fig. 4.6 is a schematic diagram of using a VCO in the servo system. As before, the signal generator provides the RF offset signal for OPLL2. However the RF offset signal of OPLL1 is now provided by a VCO (dashed red line) instead of the signal generator (dashed line (1)). The output of the null detector (PD2) is fed back to the VCO. The VCO feedback loop has two functions. First, it forces the VCO to track the frequency of the signal generator, so that the slave lasers in the two OPLLs have the same frequency. Secondly, it automatically corrects the differential optical path-length variation in the fiber. In this section I analyze this servo system in detail.

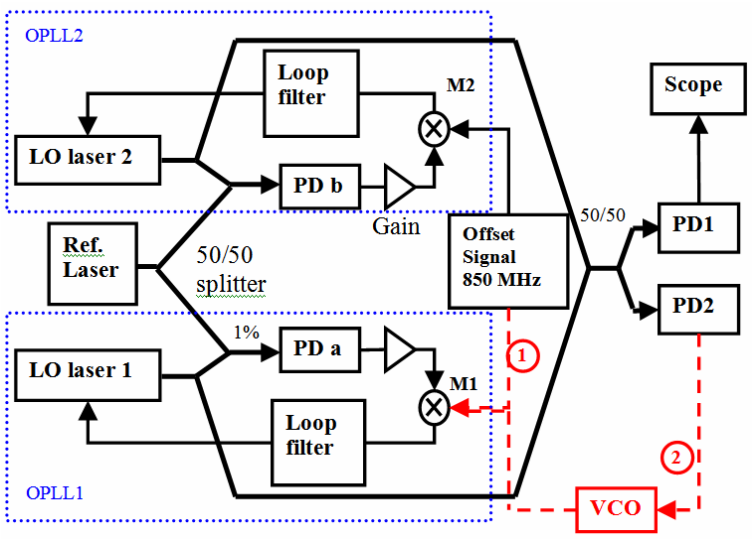

PD: photodetector M: mixer VCO: voltage-controlled-oscillator Scope: oscilloscope

Fig. 4.6 Schematic diagram of combining two OPLLs using a VCO feedback loop to correct for the optical path-length variation

Coupled PLLs picture

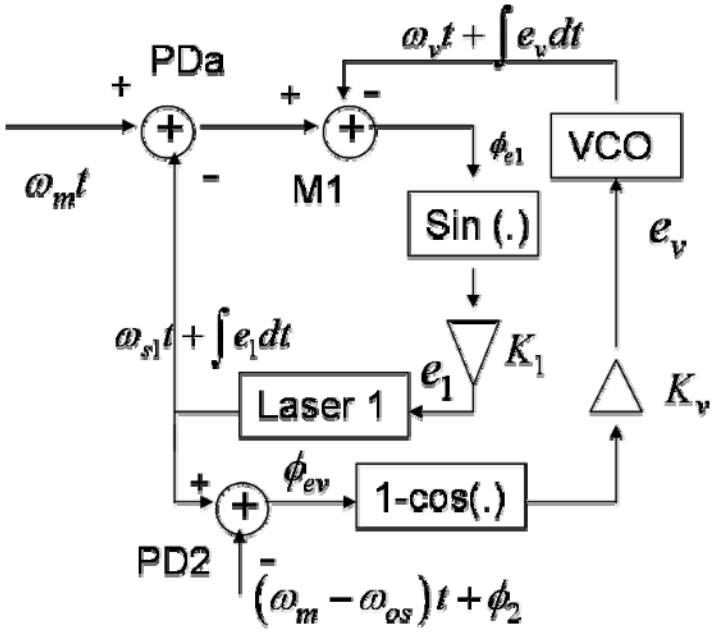

Fig. 4.7 Steady state phase model of the combining system with the VCO loop. The LO laser 2 is locked to the master laser in OPLL2, and is not shown here.

A rigorous analysis of the servo system needs to consider OPLL1 and the VCO loop as a coupled system. The steady state phase model of the VCO combining scheme is shown in Fig. 4.7. The LO laser 2 is locked to the master laser (of frequency ω_m) at a frequency offset of ω_{os}, and has a residual phase noise of $\phi_2(t)$. ω_{s1} and ω_v are the free-running frequencies of the slave laser 1 and the VCO, respectively. K_1 is the OPLL gain given by the product of the gains of the photodetector PDa, mixer, and the loop filter, and the FM responsivity of the laser. Similarly, K_v is the net gain in the VCO branch given by the product of the gains of the photodetector PD2, the FM responsivity of the VCO, and the loop filter. Referring to Fig. 4.7, the differential phase error $\phi_{e1}(t)$ in the OPLL1 and $\phi_{ev}(t)$ in the VCO loop are given by

$$\phi_{e1}(t) = \omega_m t - \underbrace{\left(\omega_{s1} t + \int_{-\infty}^{t} K_1 \sin\phi_{e1}(t)dt \right)}_{\text{phase of slave laser 1}} - \underbrace{\left(\omega_v t + \int_{-\infty}^{t} K_v \left(1-\cos\phi_{ev}(t)\right) dt \right)}_{\text{phase of the VCO}} \tag{4.4}$$

$$\phi_{ev}(t) = \underbrace{\left(\omega_{s1} t + \int_{-\infty}^{t} K_1 \sin\phi_{e1}(t)dt \right)}_{\text{phase of slave laser 1}} - \underbrace{\left\{ \left(\omega_m - \omega_{os}\right)t + \phi_2 \right\}}_{\text{phase of slave laser 2}} \tag{4.5}$$

Differentiating Eqs. (4.4) and (4.5), one obtains

$$\dot{\phi}_{e1}(t) = \left(\omega_m - \omega_{s1} - \omega_v\right) - K_1 \sin\phi_{e1} - K_v\left(1-\cos\phi_{ev}\right) \tag{4.6}$$

$$\dot{\phi}_{ev} = \left(\omega_{s1} - \omega_m + \omega_{os}\right) + K_1 \sin\phi_{e1} - \dot{\phi}_2 \tag{4.7}$$

The steady state operating point of the system is obtained by setting the time derivatives of the mixer (M1) and photodetector (PD2) outputs $\phi_{e1}(t)$ and $\phi_{ev}(t)$, to zero in Eqs. (4.6) and (4.7), giving

$$\phi_{e1,ss} = \sin^{-1}\left(\frac{\omega_m - \omega_{s1} - \omega_{os}}{K_1} \right) \tag{4.8}$$

$$\phi_{ev,ss} = \cos^{-1}\left(1 - \frac{\omega_{os} - \omega_v}{K_v}\right) \tag{4.9}$$

The total combined power detected at the photodetector PD1 is

$$P = P_0\left(1 + \cos\phi_{ev}\right) \tag{4.10}$$

where P_0 is the power of one beam. For maximum power combining efficiency (the useful combined output power divided by the input optical power), $\phi_{ev,ss}$ should be as close to zero as possible. Combining Eq. (4.9) and Eq. (4.10), the power combining efficiency can be tuned by varying ω_v, the free-running frequency of the VCO. 100% efficiency is achieved when the VCO free-running frequency is made equal to the offset signal frequency ω_{os}. However, there is a trade-off between the combining efficiency and the frequency of cycle slips, as can be seen from Eq. (4.9). As $\phi_{ev,ss}$ approaches zero, the frequency jitter of the VCO can cause the quantity $\omega_{os} - \omega_v$ to take a negative value, in which case there is no solution to Eq. (4.9) and the VCO loop loses lock. Therefore, the frequency noise of the free-running VCO compared to the loop gain K_v limits the minimum value that $\phi_{ev,ss}$ can take.

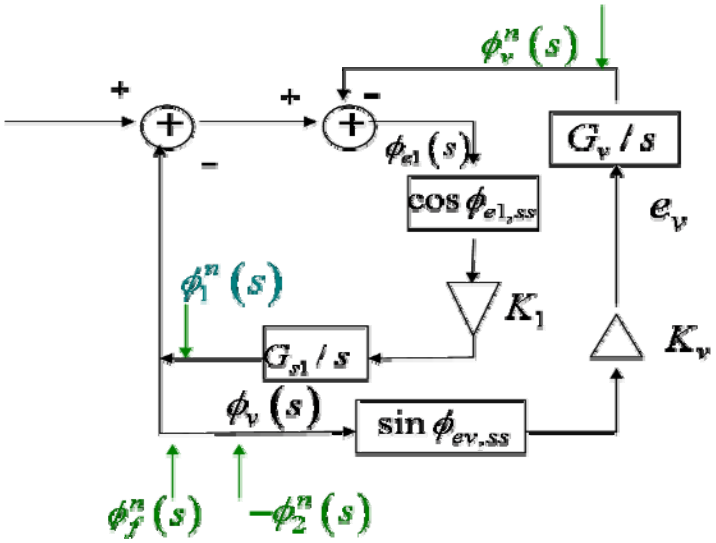

Fig. 4.8 Schematic diagram of the phase noise propagation in the coupled OPLLs

Small signal analysis

Next, I linearise the system about the steady state operating point, in order to analyze its small signal noise property. Strictly speaking, this linearisation is inappropriate because the photodetector output (Eq.(4.10)) is highly nonlinear at the null point. However, a linear analysis is useful in obtaining some physical insight into the problem. The linearised model for the system is shown in Fig. 4.8. One can write down the loop equations

$$\begin{cases} -\left(K_1' \dfrac{\phi_{e1}(s)}{s} + \phi_1^n(s) \right) - \dfrac{K_v'}{s}\phi_{ev}(s) - \phi_v^n(s) = \phi_{e1}(s) \\ K_1' \dfrac{\phi_{e1}(s)}{s} + \phi_1^n(s) + \phi_f^n(s) - \phi_2^n(s) = \phi_{ev}(s) \end{cases} \tag{4.11}$$

where $\phi_1^n(s)$ and $\phi_v^n(s)$ are the intrinsic phase noise of the slave laser 1 and the VCO, $\phi_2^n(s)$ is the phase noise of the locked slave laser 2, and $\phi_f^n(s)$ is the phase noise resulting from the differential optical path-length variation of the combining fibers. K_1' and K_v' are the small signal "loop gains" defined as

$$\begin{cases} K_1' \triangleq K_1 \cos\phi_{e1,ss} \\ K_v' \triangleq K_v \sin\phi_{ev,ss} \end{cases} \tag{4.12}$$

where $\phi_{e1,ss}$ and $\phi_{ev,ss}$ are given in Eqs. (4.8) and (4.9). After some algebra, one can simplify Eq. (4.11) to obtain

$$\begin{cases} \phi_{e1}(s) = \dfrac{-\phi_1^n(s)(1+K_v'/s) + \left(\phi_2^n(s) - \phi_f^n(s)\right)K_v'/s - \phi_v^n(s)}{1 + K_1'/s + K_1'K_v'/s^2} \\ \phi_{ev}(s) = \dfrac{\phi_1^n(s) - \left(\phi_2^n(s) - \phi_f^n(s)\right)(1+K_1'/s) - \phi_v^n(s)K_1'/s}{1 + K_1'/s + K_1'K_v'/s^2} \end{cases} \tag{4.13}$$

In principle Eq. (4.13) should be used to analyze the residual phase noise and the performance of the OPLL and the VCO loop. This picture is very complicated and does not provide an intuitive understanding of the servo system. In the next part I will use a

simplified picture to analyze the servo system to gain a better intuitive understanding.

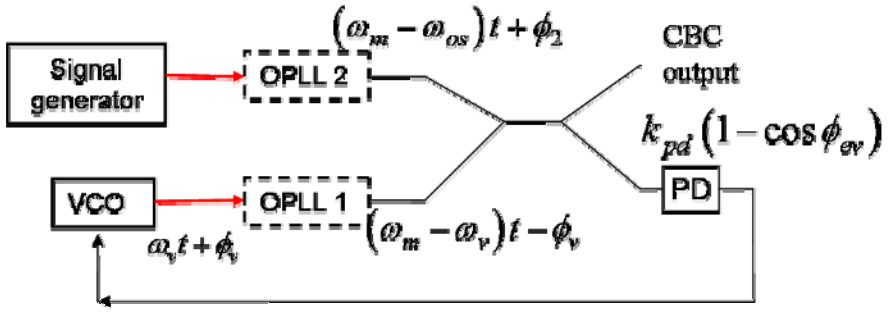

Fig. 4.9 Simplified picture of the VCO servo system.

A simplified picture— the decoupled PLLs

To obtain an intuitive picture of the function of the servo system using the VCO loop, one can simplify the analysis by decoupling OPLL1 and the VCO loop and studying them separately. This simplified picture is illustrated in Fig. 4.9. The validity of this picture can be justified using the following argument: OPLL1, which locks the slave laser 1 to the master laser, typically has a bandwidth of ~10MHz. The VCO loop is used to correct the phase variation in fiber (~Hz) and can be much slower compared to OPLL1. Actually the VCO loop delay, mainly the length of fiber in the fiber amplifier is more than 30m. This long delay, combined with the phase delay of the other electronics, limits the bandwidth of the VCO loop to a few hundred kHz. Thus one can assume that OPLL1 always tracks the phase of the VCO instantly when the phase of the VCO is adjusted to correct for the optical path length variation. Thus the two loops can be studied separately. The analysis of OPLL1 is already given in Chapter 2. In Fig. 4.9, one observes that the VCO loop is similar to a standard PLL, except that the output of the phase detector is proportional to $(1-\cos\phi_{ev})$ instead of $\sin\phi_{ev}$. Following the standard PLL analysis[1], the evolution equation of the VCO loop is

$$\underbrace{\omega_m t - \omega_{v,f} t - K_v \int (1-\cos\phi_{ev})dt}_{\text{phase of beam 1}} - \underbrace{\left[(\omega_m - \omega_{os})t + \phi_2\right]}_{\text{phase of beam 2}} = \phi_{ev} \qquad (4.14)$$

where $\omega_m, \omega_{os}, \omega_{v,f}$ are, respectively, the frequency of the master laser, the RF offset signal, and the free-running VCO, K_v is the VCO loop gain, ϕ_{ev} is the phase difference between the two individual beams at the combining point, and ϕ_2 is the phase of beam 2. In obtaining Eq. (4.14) I have used the equality $\phi_v = K_v \int (1 - \cos\phi_{ev}) dt$. Differentiating Eq. (4.14) and setting the time derivatives of ϕ_2 and ϕ_{ev} to zero, one finds the steady state phase error:

$$\phi_{ev,ss} = \cos^{-1}\left(1 - \frac{\omega_{os} - \omega_{v,f}}{K_v}\right) \tag{4.15}$$

So the steady state solution obtained in this decoupled picture is the same as the one obtained in the coupled loops picture (Eq. (4.9)). As long as $0 < \left(\omega_{os} - \omega_{v,f}\right) / K_v < 2$, Eq. (4.15) has a solution and the VCO frequency can be locked to the frequency of the offset signal. It is important to note that the steady state phase error under lock, $\phi_{ev,ss}$, which controls the CBC efficiency, can be adjusted by tuning the frequency difference $\omega_{os} - \omega_{v,f}$. High combining efficiency is achieved by minimizing $\phi_{ev,ss}$. However, this comes at the cost of increased cycle-slips caused by the residual phase noise in the OPLLs and frequency jitter of the VCO. The smallest feasible $\phi_{ev,ss}$ is mainly limited by the intrinsic frequency jitter of the free-running VCO and the equivalent frequency jitter of the phase noise in fiber compared to the loop gain K_v. Generally a clean VCO will be helpful in reducing $\phi_{ev,ss}$ and increasing the CBC efficiency. The CBC efficiency can also be increased by increasing the loop gain K_v. However, as I have pointed out, the loop gain of the VCO loop is limited by the long fiber delay if a fiber amplifier is to be used. This dilemma is very similar to the situation I analyzed in Section 3.3.2, where the OPLL bandwidth is limited by the thermal crossover of the FM response and is not

enough to hold the loop in lock due to the frequency jitter of SCLs. If the frequency jitter of the VCO is much slower than the bandwidth of the VCO loop, I can use similar strategies to those given in Section 3.3.2, i.e. the use of a lag-lead filter to increase the loop gain at low frequency and reduce $\phi_{ev,ss}$ to a smaller number.

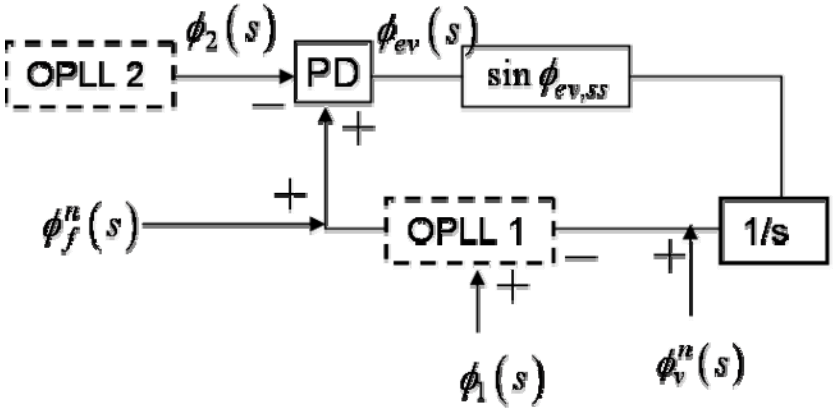

Fig. 4.10 Linearized model of the VCO loop

Next I linearize the system about the steady state point and perform the small signal analysis. A small signal linearized model is presented in Fig. 4.10. $\phi_f^n(s)$ and $\phi_v^n(s)$ are the optical path length variation in fiber and the phase noise of the free-running VCO respectively. ϕ_1 and ϕ_2 denote the residual phase noise of OPLL1 and OPLL2 respectively. Following the standard PLL analysis, one obtains

$$\phi_f^n(s)+\phi_1(s)-\left[\frac{K_v\sin\phi_{ev,ss}}{s}\cdot\phi_{ev}(s)+\phi_v^n(s)\right]-\phi_2(s)=\phi_{ev}(s) \tag{4.16}$$

Solving for $\phi_{ev}(s)$ gives

$$\phi_{ev}(s)=\frac{\phi_1(s)+\phi_f^n(s)-\phi_v^n(s)-\phi_2(s)}{1+\dfrac{K_v\sin\phi_{ev,ss}}{s}} \tag{4.17}$$

In Eq. (4.17) one first observes that a nonzero $\phi_{ev,ss}$ is needed to provide a non-zero small signal loop gain. Secondly, the residual phase noises from OPLL1 and OPLL2 are

mostly concentrated at frequencies of a few MHz as I have shown in Chapter 3. Since the bandwidth of the VCO loop is ≤ 100kHz, the VCO feedback loop does not greatly affect the residual phase noise of the OPLLs. A typical high quality VCO possesses very low phase noise compared to a SCL. The optical path length variation $\phi_f^n(s)$ is at very low frequency, according to our experimental observation (~Hz). These noises can be significantly suppressed by the VCO loop with a bandwidth of ~100kHz.

Experimental result

I performed the CBC experiment with the IPS lasers as shown in Fig. 4.6. A MinCircuits ZX95-2150 VCO is used in the experiment. Fig. 4.11(b) shows the combined power using the VCO feedback scheme, and demonstrates the high combining efficiency achieved. Compared with Fig. 4.2(b), the combined power is held at constant with a power combining efficiency of about 94%. The loss of the combining efficiency (6%) can be attributed to the residual differential phase noise in the individual OPLLs, the frequency jitter of the VCO, and the nonzero steady state phase error in the VCO control loop. Mathematically the combining efficiency is expressed as

$$\eta = \left(1 + \overline{\cos\left(\phi_{ev,ss} + \Delta\phi_{ev} + \phi_2 - \phi_1\right)}\right)/2 \tag{4.18}$$

where $\phi_{ev,ss}$ is the steady state phase error in the VCO loop, $\Delta\phi_{ev}$ is the phase jitter caused by the frequency jitter of the VCO, and ϕ_1 and ϕ_2 are the residual phase noises in OPLL1 and OPLL2 respectively. Assuming $\phi_{ev,ss}$, $\Delta\phi_{ev}$, ϕ_1, and ϕ_2 are small numbers and not correlated, and that $\Delta\phi_{ev}$, ϕ_1, ϕ_2 all have zero means, one can expand Eq. (4.18) and reduce it to

$$\eta \approx 1 - \left(\phi_{ev,ss}^2 + \overline{\Delta\phi_{ev}^2} + \overline{\phi_2^2} + \overline{\phi_1^2}\right)/4 \tag{4.19}$$

$\overline{\phi_1^2}$ and $\overline{\phi_2^2}$ can be calculated from the measured power spectrum of the locked beat signal (Section 3.2.1), i.e. $\overline{\phi_n^2} = P_n / P_s$. Where P_s is the power of the central carrier

signal and P_n is the power of the phase noise and can be obtained by integrating the double-sided power spectral density excluding the central carrier. Fig. 4.11(a) shows a typical power spectrum of the locked beat signal in an IPS laser OPLL. Based on the measured spectrum, the typical values of $\overline{\phi_2^2}$ and $\overline{\phi_1^2}$ are 0.02~0.05. Substituting the numbers in Eq. (4.19), I estimate 1~2% of the combined power is lost due to the residual phase noise in the OPLLs. Another 4% is lost due to the non-zero steady state value $\phi_{ev,ss}$ and the frequency jitter of the VCO. In Fig. 4.11(b), one observes that the mean value of the combined signal slowly increases with time and more cycle slips are seen. This can be attributed to the slow drift of the VCO frequency which reduces $\phi_{ev,ss}$ and leads to more frequent cycle slips.

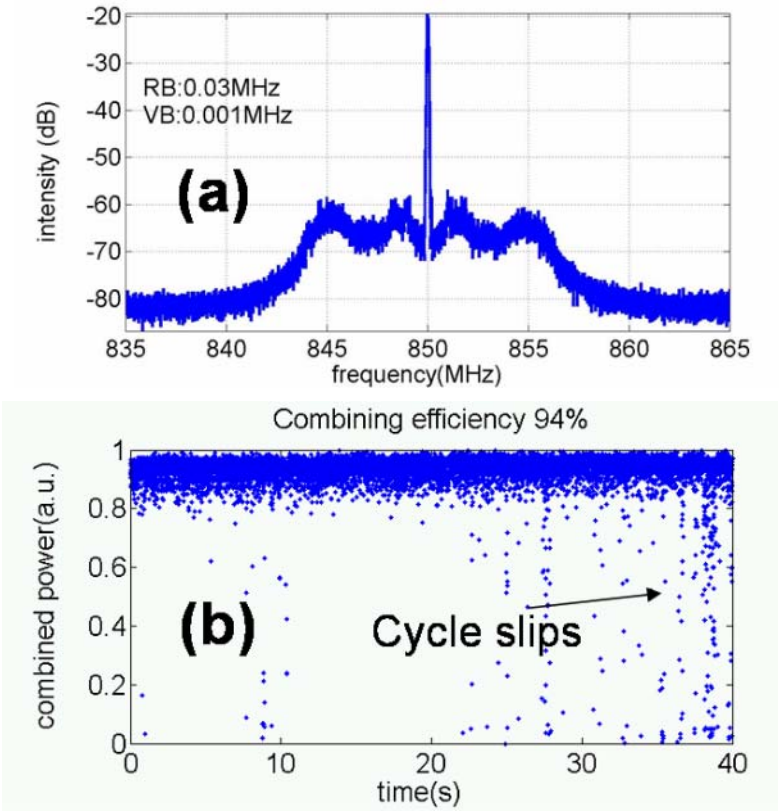

Fig. 4.11 (a) A typical power spectrum of the locked beat signal in an IPS laser OPLL. (b) Measured combined signal of two IPS lasers. The differential optical path-length variation in the fiber is corrected for by the VCO loop.

In conclusion, I have demonstrated the coherent power combining of two commercial SCLs in fiber with the filed-aperture approach using the OPLLs. An additional feedback loop with a VCO has been used to compensate for fluctuations of the differential optical path lengths of the combining optical waves. This full electronic servo scheme eliminates the need for optical feedback or expensive optical components such as optical phase/frequency modulators[3, 4]. However, as I have pointed out in this chapter, that the combining efficiency is reduced by various factors, such as the residual phase noise of the OPLLs and the non-zero steady-state operating point of the VCO loop. It is not clear to what extent these factors will affect the CBC system when this technology is scaled to the combination of a large number of beams. This will be the topic of study in the next chapter.

Chapter 5 Analysis of the scalability of a cascaded filled-aperture coherent beam combining system

5.1. Introduction

Coherent beam combining (CBC) has been implemented with both tiled-aperture and filled-aperture schemes. In both schemes, the combining efficiency (the useful combined output optical power divided by the input optical power) is degraded by various noise and loss sources, including the relative phase error between the element beams, the polarization mismatch, the intensity mismatch, the relative element beam pointing error, the absorption and scattering loss of optical components, and a less-than-unity fill factor in the tiled-aperture scheme or non-ideal near-field overlap in the filled-aperture scheme. Influence of the relative phase error and the less-than-unity fill factor on the combining efficiency and beam quality has been studied for the tiled-aperture scheme[52]. Among all the factors, the control of the relative phase between the element beams remains the most critical and difficult task. In the last chapter, we proposed, analyzed, and demonstrated using a full electronic servo system made of multilevel PLLs to address this issue. However, the OPLLs introduce some residual phase error between the element beams, and the VCO loop introduces a non-zero steady state phase error between the element beams. In the presence of these phase errors, a combining efficiency of 94% is achieved when combining two beams in fiber. In this chapter, I will study to what extent these phase errors will affect a CBC system of combining a large number of beams.

The OPLL servo system can be applied to both the tiled-aperture and the filled-aperture schemes. Analysis of the combining efficiency of a tiled-aperture scheme has been given in [52]. Here I focus on analyzing the combining efficiency of the filled-aperture scheme in the presence of various noise sources, particularly the residual phase noise of the OPLLs, the frequency jitter of the VCO and the resulting non-zero

steady state phase error in the VCO loops, the phase front deformation due to the combining beam splitters and mirrors, and the intensity noise. Our analysis will focus on the scalability of the system given all the noise sources. A rigorous analysis should consider the coupling of all the different factors, which is a very difficult task. Here I will assume that they do not affect each other and that one can consider them separately. Since high power fiber amplifiers will be used to boost the optical power, the phase noise introduced by the fiber amplifier will also be discussed and characterized.

5.2 Combining efficiency of the filled-aperture scheme

In a filled-aperture CBC scheme, multiple beams can be combined with a combiner such as a $N \times 1$ fiber coupler. Alternatively two beams are overlapped and combined with a beam splitter. A cascaded binary-tree scheme can then be used to scale the system to combine a large number of beams. Now consider combining N beams at a combiner. The combined intensity at the output of the combiner, averaged over time and space, $\overline{I_p}$, is given by

$$\overline{I_p} = \overline{\left| \sum_i \vec{E}_i \left[r_\perp, \Phi_i \left(r_\perp, t \right) \right] \right|^2} \tag{5.1}$$

where $\vec{E}_i \left[r_\perp, \Phi_i \left(r_\perp, t \right) \right]$ is the complex electric field of the individual beam *i* having a phase fluctuation $\Phi_i \left(r_\perp, t \right)$. $\Phi_i \left(r_\perp, t \right)$ is a function of both time *t* and the transverse coordinate $\vec{r}_\perp$. The $\vec{r}_\perp$ dependence of $\vec{E}_i$ allows for the consideration of wave-front overlap, e.g., alignment mismatch. The temporal and spatial dependence of $\Phi_i \left(r_\perp, t \right)$ allows for the consideration of the degree of mutual coherence and the phase front error between the element beams due to the OPLL residual phase noise, the surface deformation of the optical components, and the pointing error.

Fig. 5.1 shows an example of combining two beams using a beam splitter. Two plane

waves, E_1 and E_2, at the same frequency with fixed relative phase are incident upon a beam splitter having an amplitude reflectivity *r*. At the outputs of the beam splitter there are two pairs of waves propagating at right angles, whose intensities are given by

$$\begin{aligned} I_{P1} &= \alpha\left[E_1^2 r^2 + E_2^2\left(1-r^2\right) + 2E_1E_2r\left(1-r^2\right)^{1/2}\cos\left(\Delta\phi\right)\right] \\ I_{P2} &= \alpha\left[E_2^2 r^2 + E_1^2\left(1-r^2\right) + 2E_1E_2r\left(1-r^2\right)^{1/2}\cos\left(\Delta\phi+\pi\right)\right] \end{aligned} \tag{5.2}$$

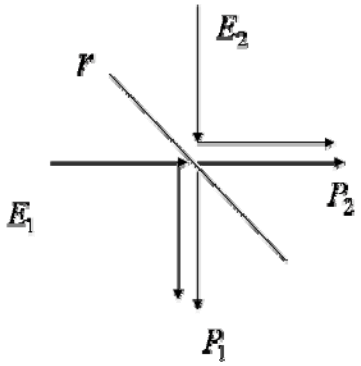

Fig. 5.1 Example of coherent beam combining using a beam splitter. *r* is the reflectivity of the beam splitter.

where $\Delta\phi$ is the phase difference between the two incident waves and α is a constant factor. In the simplest case the two beams possess equal amplitudes, and the beam splitter has a 50:50 splitting ratio, i.e., $r = 1/\sqrt{2}$, $E_1 = E_2 = E_0$. In this case Eq. (5.2) is simplified to

$$I_{P1} = E_0^2\left[1+\cos\left(\Delta\phi\right)\right],\ I_{P2} = E_0^2\left[1-\cos\left(\Delta\phi\right)\right] \tag{5.3}$$

In the ideal case, $\Delta\phi = 0$, all the input power comes out of output 1 and the combining efficiency is 100%. When a position and time dependent phase noise and an intensity variation are present, the combining efficiency becomes

$$\begin{aligned} \eta &= \frac{\overline{I_p}}{\overline{I_1}+\overline{I_2}} = \frac{1}{4}\overline{\left|\sqrt{1+r_1}+\sqrt{1+r_2}\,\exp\left(i\phi\right)\right|^2} \\ &\approx 1-\frac{1}{4}\overline{\phi^2}-\frac{1}{8}\left(\overline{r_1^2}+\overline{r_2^2}\right) \end{aligned} \tag{5.4}$$

where r_1, r_2 stands for the relative intensity noise (RIN) of beam 1 and 2, and ϕ represents the differential phase error between the two beams. The bar over r_1, r_2, and ϕ stands for the averaging over either time or space depending on the situation. In obtaining Eq. (5.4) I have assumed that the noises have zero mean and are small enough so that the higher order expansion terms can be ignored. To the second-order, the phase noise and the intensity noise are not coupled to each other and hence their effects will be studied separately. Having understood the effect of noises on combining two beams, I will proceed to the analysis of the combination of any number of beams.

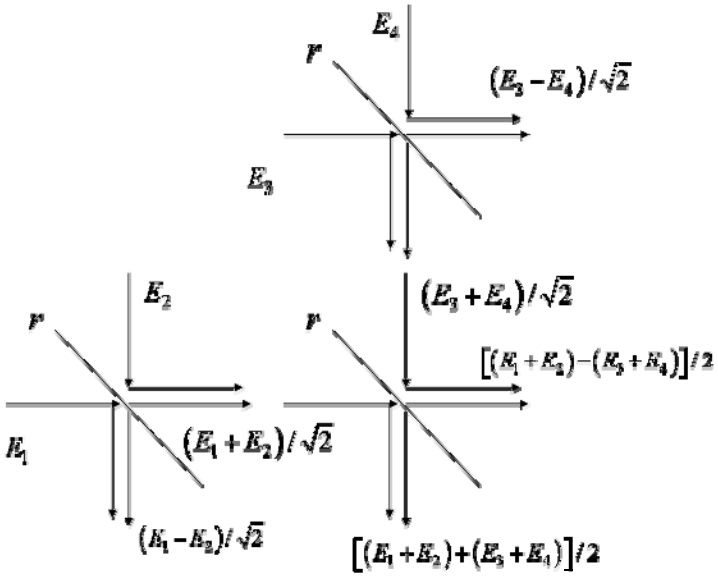

Fig. 5.2 Schematic diagram of a 2-level binary-tree filled-aperture CBC system

5.2.1 Effect of OPLLs residual phase noise

Fig. 5.2 shows a schematic diagram of a 2-level binary-tree filled-aperture CBC system. This scheme can be scaled to an arbitrary number of beams $N = 2^n$ where n is the number of levels in the binary tree structure. Assuming all the beams have equal amplitudes and are perfectly aligned, the combined field takes the form of

$$E_t = E_0 \sum_{i=1}^{N} e^{i\phi_i} \tag{5.5}$$

where $\phi_i(t)$ represents the phase of the individual beam *i* referred to a common reference phase plane. The intensity of the combined field is proportional to the square of the electric field. Normalizing the combined power by the total input power, one obtains the CBC efficiency

$$\eta = \frac{1}{N^2} \overline{\sum_{i,j=1}^{N} e^{i(\phi_i - \phi_j)}} \tag{5.6}$$

I further assume that ϕ_i obeys a Gaussian distribution with zero mean and variance $\overline{\phi_i^2(t)} = \sigma^2$. If ϕ_i and ϕ_j are uncorrelated, then $\overline{\exp\left[i(\phi_i - \phi_j)\right]} = e\left(-\delta_{i,j}\sigma^2\right)$ [52, 63] where $\delta_{i,j}$ is the Kronecker's delta. Eq. (5.6) then becomes

$$\eta = 1 - \frac{N-1}{N}\left(1 - e^{-\sigma^2}\right) \tag{5.7}$$

Assuming $\sigma^2 << 1$, Eq. (5.7) further reduces to

$$\eta = 1 - \frac{(N-1)}{N}\sigma^2 \tag{5.8}$$

As can be seen, the combining efficiency converges to $1-\sigma^2$ for a large number of beams. In Chapter 2 I have obtained the phase noise of the *i*th locked slave laser as

$$\phi_i(s) = \frac{G_{op}}{1+G_{op}}\phi_m^n(s) + \frac{1}{1+G_{op}}\phi_{fr,i}^n(s) \tag{5.9}$$

where ϕ_m^n and $\phi_{fr,i}^n$ are, respectively, the phase noise of the master laser and the *i*th slave laser the under free-running condition, and G_{op} is the open loop transfer function of the *i*th OPLL. If one takes the inverse Fourier transform of Eq. (5.9) and plug it into

$\overline{\phi_i(t)-\phi_j(t)}$ of Eq. (5.6), the first term relating to the phase noise of the master laser ϕ_m^n will cancel out as long as G_{op} is the same for different OPLLs. Thus, one concludes that the phase noise of the master laser does not affect the combining efficiency, since it acts as a common phase reference for all the slave lasers. The second term of Eq. (5.9) is uncorrelated among different slave lasers. If the corresponding variance is σ^2, Eqs. (5.7) and (5.8) can be used to calculate the degraded combining efficiency. In Fig. 5.3 I plot the combining efficiency calculated with the small signal approximation as a function of the rms phase error σ for N=2 and N=8. The small signal approximation agrees well with the Monte Carlo simulation results for small σ.

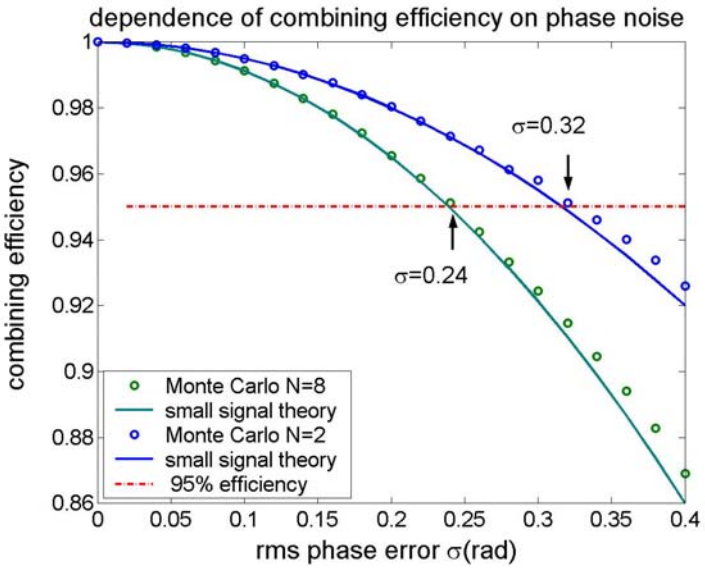

Fig. 5.3 Calculated combining efficiency as a function of the residual differential phase noise

From Eq. (5.8), for a given number of beams and a desired combining efficiency, the rms phase error has to satisfy

$$\sigma \le \sqrt{(1-\eta)\frac{N}{N-1}} \tag{5.10}$$

e.g, if 8 beams are to be combined with an efficiency $\eta = 95\%$, the rms phase error has to be smaller than $0.24rad$. For the IPS OPLL the smallest rms phase error I have measured is around $0.13rad$, which ultimately limits the combining efficiency to ~98%.

5.2.2 Effect of the frequency jitter of the VCO

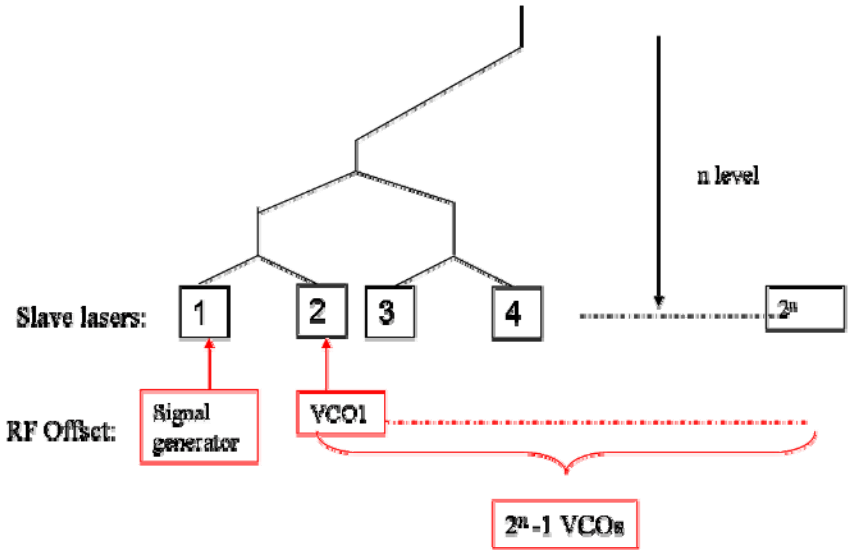

Fig. 5.4 Schematic diagram of a binary-tree filled-aperture CBC system using the VCO loops to correct for the optical path-length variation in fibers

In Chapter 4 I discussed the use of a VCO loop to correct for the optical path-length variation in fibers. I pointed out that a non-zero steady state phase error between the element beams is required to tolerate the frequency jitter of the VCO, and leads to a reduced combining efficiency. In this section I will evaluate the influence of the frequency jitter of the VCO and the nonzero steady-state phase error on the combining efficiency of a cascaded filled-aperture CBC system.

In Chapter 4 I derived that the steady state solution of the phase error in the VCO loop is

$$\phi_{ev,ss} = \cos^{-1}\left(1 - \frac{\omega_{os} - \omega_{v,f}}{K_v}\right) \tag{5.11}$$

where ω_{os} is the frequency of the RF offset signal provided by the signal generator and $\omega_{v,f}$ is the frequency of the free-running VCO, and K_v is the VCO loop gain. Eq. (5.11) has a solution when

$$0 < \left(\omega_{os} - \omega_{v,f}\right) / K_v < 2 \tag{5.12}$$

The combining efficiency is given by $\left(1+\cos\phi_{ev}\right)/2$, therefore one wants to minimize $\phi_{ev,ss}$ to maximize the combining efficiency. However, if the steady state frequency difference $\omega_{os} - \omega_{v,f}$ takes a negative value, Eq. (5.11) has no solution which means the VCO loop will lose lock. Assume that the frequency jitter of the free-running VCO has Gaussian distribution with zero mean and variance σ_ω. Obviously, if $\omega_{os} - \omega_{v,f} = 0$ the VCO could only acquire lock half of the time. If one sets $\omega_{os} - \omega_{v,f}$ equal to $x\sigma_\omega$, where x is a positive number, the quantity $\omega_{os} - \omega_{v,f}$ obeys the Gaussian distribution with mean value $x\sigma_\omega$ and variance σ_ω. The probability for $\left(\omega_{os} - \omega_{v,f}\right)/K_v$ to take a negative value is described by the cumulative distribution function of Gaussian distribution

$$F\left(-x;0,1\right) = \frac{1}{\sqrt{2\pi}} \int_{-\infty}^{-x} \exp\left(-\frac{u^2}{2}\right) du \tag{5.13}$$

If x is small and $\sigma_\omega << K_v$, the probability that $\left(\omega_{os} - \omega_{v,f}\right)/K_v > 2$ is very small and can be ignored. Then the probability that Eq. (5.11) has a solution, or equivalently, that the VCO loop can acquire lock, is given by $1 - F\left(-x;0,1\right)$. E.g, if one lets $\left(\omega_{os} - \omega_{v,f}\right)_{ss} = 2\sigma_\omega$, the probability that the VCO loop is in lock is given by $1 - F\left(-2;0,1\right) = 97.72\%$.

In the binary-tree cascaded filled-aperture scheme, a VCO loop is needed each time two beams are combined. If $N = 2^n$ beams are to be combined, the number of VCO

loops will be $2^n - 1$ (refer to Fig. 5.4). If any one of the VCO loops loses lock, the whole system will be disrupted. To simplify the analysis, I assume that the VCO loops are uncorrelated, so that the probability that all the VCO loops are in lock is given by

$$P_{lock} = \left[1 - F\left(-x; 0, 1\right)\right]^{2^n - 1} \tag{5.14}$$

Meanwhile, the combining efficiency is reduced due to the frequency jitter and the non-zero $\phi_{ev,ss}$ even when the system is in lock. At each combining level of the binary-tree scheme, the combining efficiency is

$$\begin{aligned} \eta &= \left(1 + \overline{\cos\phi_{ev}}\right)/2 \\ &= 1 - \frac{\omega_{os} - \omega_{v,f}}{2K_v} \end{aligned} \tag{5.15}$$

In deriving Eq. (5.15) I have used Eq. (5.11). Assuming $\omega_{os} - \omega_{v,f} = x\sigma_\omega$, the combining efficiency of a locked system with *n* levels is

$$\eta_{lock} = \left(1 - \frac{x\sigma_\omega}{2K_v}\right)^n \tag{5.16}$$

Now one takes into account the fact that the system stays in lock only with a certain probability. Therefore the true combining efficiency should be the product of P_{lock} and η_{lock}

$$\eta = \left[1 - F\left(-x; 0, 1\right)\right]^{2^n - 1} \cdot \left(1 - \frac{x\sigma_\omega}{2K_v}\right)^n \tag{5.17}$$

P_{lock} is a monotonously increasing function of x, while η_{lock} is a monotonously decreasing function of x in the range $0 < x\sigma_\omega / K_v < 2$ where Eq. (5.11) has a solution. Hence an optimal value of x can be chosen to maximize the efficiency described by Eq. (5.17). In Fig. 5.5(a) I plot the combining efficiency as a function of the normalized frequency detuning $x = \left(\omega_{os} - \omega_{v,f}\right)/\sigma_\omega$ for a given normalized frequency jitter $\sigma_\omega / K_v = 0.05$. For each value of *n*, an appropriate value of *x* can be chosen to maximize

the overall combining efficiency.

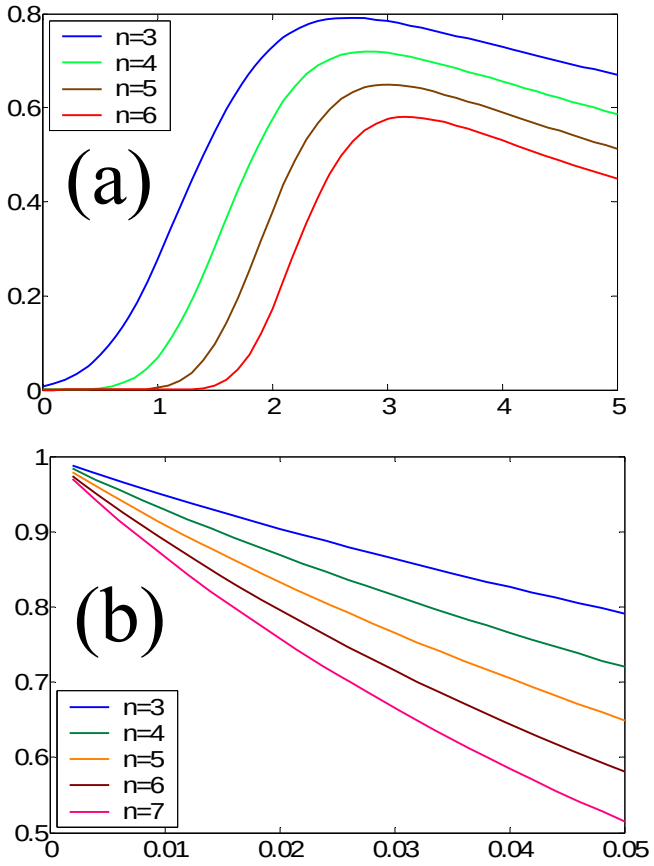

Fig. 5.5 (a) Combining efficiency as a function of the normalized frequency detuning $x = \left(\omega_{os} - \omega_{v,f}\right)/\sigma_{\omega}$ given $\sigma_{\omega}/K_v = 0.05$. A maximum value can be reached by picking the appropriate value of *x*. (b) Maximum combining efficiency as a function of the normalized VCO frequency jitter σ_{ω}/K_v. ω_{os} is the frequency of the RF offset signal provided by the signal generator, $\omega_{v,f}$ is the frequency of the free-running VCO, σ_{ω} is the rms frequency jitter of the VCO, and K_v is the VCO loop gain. The number of element beams is 2^n.

In Fig. 5.5(b) I plot the maximum combining efficiency as a function of the

normalized frequency jitter σ_ω / K_v for different values of *n*. The combining efficiency drops quickly with the increase of both σ_ω / K_v and *n*. To combine a large number of beams, it is therefore critical to have a small value of σ_ω / K_v to achieve a high combining efficiency. In the CBC experiment with one VCO loop presented in Section 4.3.2, I estimate the combining efficiency lost about 2% due to the residual phase error in the OPLLs and 4% due to the non-zero steady state phase error due to the frequency jitter of the VCO. The corresponding value of σ_ω / K_v is about 0.03. As I have pointed out in Section 4.3.2.c, one solution to reduce σ_ω / K_v is to reduce σ_ω, e.g., to use a cleaner VCO with smaller frequency jitter. Another solution is to increase K_v using a lag-lead filter. With such a filter σ_ω / K_v can be reduced by an order of magnitude, and the combining efficiency penalty due to this steady state phase error can be reduced to less than 10% even for n = 7 (128 element beams).

5.2.3 Effect of phase front deformation due to optical components

Optical components such as beam splitters and reflection mirrors used in the combining system introduce phase front deformations in addition to absorption and scattering losses. Though this noise source has nothing to do with the OPLL servo system, I would like to emphasize it here because its influence on the combining efficiency could be more significant than that of the phase error in the OPLLs and the VCO loops I have analyzed.

I use Eqs. (5.6) and (5.7) to calculate the combining efficiency. In this case the bar in Eq. (5.6) represents averaging over space instead of time. Two beams passing through the same beam splitter or reflected by the same mirror will see the same phase front deformation. Thus the phase front deformations of the two beams are correlated. This scenario is illustrated in Fig. 5.6(a). Beam 1 and 2 are combined at beam splitter 1 and

see the same phase front deformation ϕ_1. Beam 3 and 4 see the same phase front deformation ϕ_2, and beam 1,2,3 and 4 also see the same phase front deformation ϕ_3, etc. A second scenario is illustrated in Fig. 5.6(b). This happens, for example, when two beams are combined at a beam splitter, where one beam is transmitted through it and the other one is reflected. Hence the two beams see different phase front deformations.

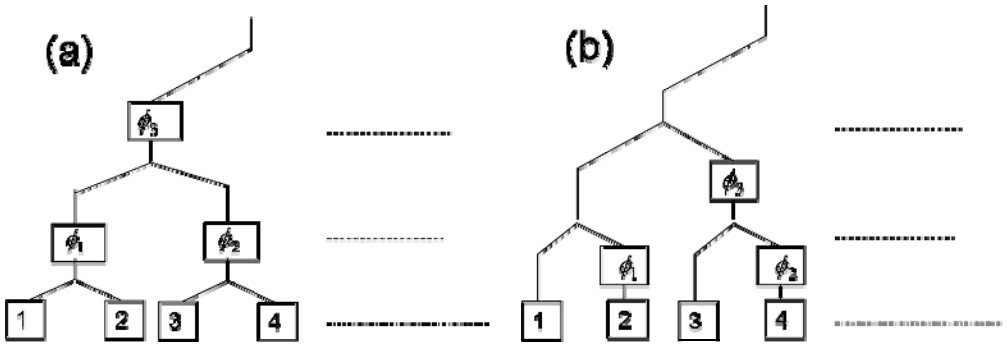

Fig. 5.6 Two scenarios of phase front deformation caused by the combining optics

I first look at scenario 1. The phase front deformations caused by different beam splitters should be uncorrelated and I will assume that the deformations obey Gaussian distribution with zero mean and variance σ^2. One can define a distance function between any two individual laser beams labeled by index *i* and *j*,

$$D(i,j)=\begin{cases}2\left[\log_2|i-j|\right], & i\neq j\\ 0, & i=j\end{cases} \tag{5.18}$$

$D(i,j)$ indicates the number of different beam splitters (or mirrors) which the beams *i* and *j* go through. For example, in Fig. 5.6(a) $D(1,2)=0$ because beam 1 and 2 go through the same beam splitters, and $D(1,3)=2$ because beam 1 and 3 go through two different beam splitters. The combining efficiency can then be calculated as

$$\eta=\frac{1}{N^2}\overline{\sum_{i,j=1}^{N}e^{i(\phi_i-\phi_j)}}=\frac{1}{N^2}\sum_{i,j=1}^{N}e^{-\frac{1}{2}D(i,j)\sigma^2} \tag{5.19}$$

where the total number of beams is $N = 2^n$. An analytical result can be obtained using mathematical recursion if the small error approximation is assumed

$$e^{-\frac{1}{2}D(i,j)\sigma^2} \approx 1-\frac{1}{2}D(i,j)\sigma^2, \quad \frac{1}{2}D(i,j)\sigma^2 << 1 \tag{5.20}$$

Eq. (5.19) then reduces to

$$\eta = \frac{1}{2^{2n}}\left(2^{2n} - \frac{\sigma^2}{2}\sum_{i,j=1}^{2^n} D(i,j)\right) \tag{5.21}$$

If one defines the function $f(n) = \sum_{i,j=1}^{2^n} D(i,j)$, then

$$f(n+1) = \sum_{i,j=1}^{2^{n+1}} D(i,j) = \left(\sum_{i,j=1}^{2^n} + \sum_{i,j=2^n+1}^{2^{n+1}} + \sum_{i=1}^{2^n}\sum_{j=2^n+1}^{2^{n+1}} + \sum_{i=2^n+1}^{2^{n+1}}\sum_{j=1}^{2^n}\right) D(i,j) \tag{5.22}$$

Since $D(i,j)$ only depends on the difference of the indices $|i-j|$, the first two terms in Eq. (5.22) are the same and are equal to $f(n)$. The other two terms are also equal to each other. Therefore Eq. (5.22) becomes

$$\begin{aligned} f(n+1) &= 2f(n) + 2\sum_{i=1}^{2^n}\sum_{j=2^n+1}^{2^{n+1}} 2\left[\log_2|i-j|\right] \\ &= 2f(n) + 2\sum_{i=1}^{2^n}\sum_{j=2^n+1}^{2^{n+1}} 2n \end{aligned} \tag{5.23}$$

Using mathematical recursion one obtains

$$f(n+1) = 2^{n+3}\sum_{i=1}^{n} i2^{i-1} \tag{5.24}$$

Using the mathematical relation

$$\sum_{i=1}^{n} ix^{i-1} = \left(\sum_{i=0}^{n} x^i\right)' = \left(\frac{1-x^{n+1}}{1-x}\right)' = \frac{(nx-n-1)x^n+1}{(x-1)^2} \tag{5.25}$$

and after some algebra one obtains

$$f(n) = (n-2)2^{2n+1} + 2^{n+2} \tag{5.26}$$

Substituting Eq. (5.26) back into Eq. (5.21) gives us the combining efficiency

$$\eta = 1 - \left[(n-2) + 2^{1-n} \right] \sigma^2 \tag{5.27}$$

For the second scenario described in Fig. 5.6(b), calculating the combining efficiency is not so straightforward. However one can make a slight modification of the diagram Fig. 5.6(b) to make it similar to Fig. 5.6(a). Take any triangle in the tree structure of Fig. 5.6(b), one can split the phase front error ϕ in one arm into two uncorrelated phase front errors ϕ_1 and ϕ_2 on both arms and let $\overline{\phi_1^2} = \overline{\phi_2^2} = \frac{1}{2}\overline{\phi^2} = \frac{1}{2}\sigma^2$, as displayed in Fig. 5.7. Next I will prove that Fig. 5.7(a) and Fig. 5.7(b) have equivalent contribution to the combining efficiency calculated using Eq. (5.19).

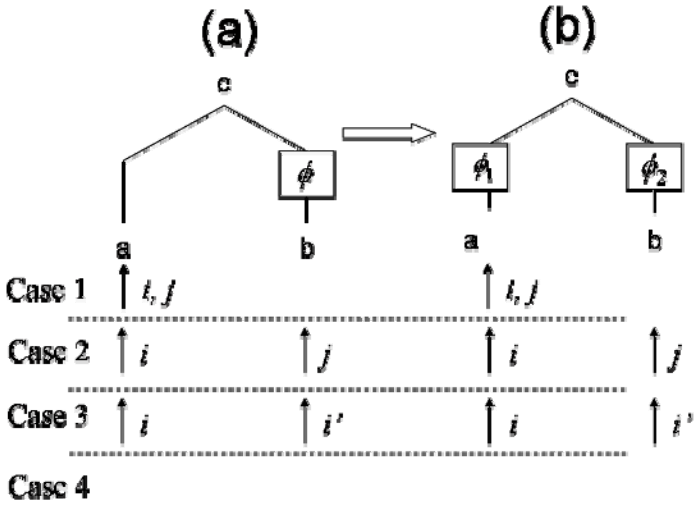

Fig. 5.7. Splitting (a) the one-side phase error into (b) two-side phase errors. Four cases need to be considered to calculate the combining efficiency (Eq. (5.19)). Case 1: both beams *i* and *j* are from the same node a or b. Case 2: one beam is from node a and the other beam is from node b. Case 3: one beam (e.g. *i*) is from this triangle and the other beam is not. *i*' is the image of beam *i* in this triangle. Case 4: neither *i* nor *j* goes through this triangle.

There are four cases that arise while calculating the contribution of this triangle to

any two beams *i* and *j* in Eq. (5.19). In the first case, both the beams *i* and *j* come in through the same node in Fig. 5.7 (either a or b). This triangle adds a common phase front error to the beams *i* and *j*. Therefore both Fig. 5.7(a) and Fig. 5.7(b) have no contribution to the quantity $\overline{\left(\phi_i-\phi_j\right)^2}$ in Eq. (5.19). In the second case, where one beam comes in through node a and the other beam through node b, both triangles in Fig. 5.7(a) and Fig. 5.7(b) contribute the same amount $\overline{\phi_1^2+\phi_2^2}=\overline{\phi^2}$ to $\overline{\left(\phi_i-\phi_j\right)^2}$. The third case happens when one beam (e.g. *i*) goes through either node a or node b, and the other beam (e.g. *j*) does not go through this triangle. In this case one can always find the image beam *i*' of beam *i* going through this triangle. If we calculate the contribution of this triangle to the quantity $\overline{\left(\phi_i-\phi_j\right)^2}+\overline{\left(\phi_{i'}-\phi_j\right)^2}$, Fig. 5.7(a) and Fig. 5.7(b) are the same. The fourth case is when neither beam *i* nor *j* goes through this triangle, and splitting the phase front error does not change anything. Therefore Fig. 5.7(a) and Fig. 5.7(b) are equivalent under the small signal approximation.

With the above modification, scenario 2 (Fig. 5.7(b)) is similar to scenario 1 (Fig. 5.7(a)) and Eq. (5.21) accordingly changes to

$$\eta=\frac{1}{2^{2n}}\left(2^{2n}-\frac{\sigma^2/2}{2}\sum_{i,j=1}^{2^n}D(i,j)\right) \tag{5.28}$$

with

$$D(i,j)=\begin{cases}2\left[\log_2|i-j|+1\right], & i\neq j\\ 0, & i=j\end{cases} \tag{5.29}$$

Using the same mathematical recursion one obtains

$$\sum_{i,j=1}^{2^n}D(i,j)=(n-2)2^{2n+1}+2^{n+2}+2\left(2^n-1\right)2^n=(n-1)2^{2n+1}+2^{n+1} \tag{5.30}$$

and the combining efficiency is

$$\eta=1-\left[\frac{n-1}{2}+2^{-n-1}\right]\sigma^2 \tag{5.31}$$

One can observe from Eqs. (5.27) and (5.31) that the combining efficiency drops linearly with the number of levels in the tree structure n=$\log_2$N. Typical rms phase front deformations of optical components are about $\lambda/40$ [64]. If N = 8 beams are to be combined, the maximum efficiency limited by phase front deformation is about $\eta \sim 97\%$. This efficiency penalty is comparable to that caused by the residual phase noise in OPLLs and the non-zero steady state phase error in the VCO loops. Since it increases linearly with $\log_2$N, optical components of superior surface flatness have to be used if a large number of beams are to be combined.

5.2.4 Effect of intensity noise

The combining efficiency can also be degraded by intensity noise, as indicated in Eq. (5.4). The intensity noise could arise from the relative intensity noise (RIN) of the slave lasers, the fiber amplifiers, or just the amplitude mismatch errors between the element beams. Assume that there is no phase noise and that the amplitude of the *i*th beam takes the form of $E_i = E_0(1+r_i)$, where r_i is the relative amplitude fluctuation with zero mean and variance $\overline{r_i^2} = \delta^2$. The efficiency of combining N beams affected by the intensity noise can then be calculated as

$$\eta = \overline{I_p} / \sum_{i=1}^{N} \overline{I_i} \approx 1 - \frac{1}{N}\left(1 - \frac{1}{N}\right)\sum_{i=1}^{N} \overline{r_i^2} \tag{5.32}$$

If all the beams have similar intensity fluctuations, the combining efficiency converges to $\eta = 1 - \delta^2$ for a large number N and the efficiency penalty does not increase with the number of beams.

The free-running RIN of state-of-the-art SCLs is typically very small. I have

characterized the RIN of the IPS lasers used in CBC by detecting the power with a photodetector and measuring the output on an oscilloscope. The bandwidth of the photodetector is 12GHz and the bandwidth of the oscilloscope is 500MHz. The measured rms RIN is 2e-4, which is limited by the shot noise and photodetector electronic noise. Since the rms residual phase noise in the OPLLs is about 0.12rad, in Eq.(5.4) the third term is much smaller than the second term and can thus be ignored safely.

Additional intensity noise can also be introduced by the OPLL feedback current. Since the current feedback is used to control the relative phase error between the slave laser and the master laser, the intensity of the slave laser can also be modulated and the magnitude needs to be carefully checked.

Here I only want to estimate the magnitude of the intensity noise caused by the feedback current. Assuming that the FM responses of the circuit and the laser are flat, the current fed back into the SCL is

$$i = i_0 \sin \phi_e \tag{5.33}$$

where ϕ_e is the detected phase difference between the master laser and the slave laser, and i_0 is a constant deciding the loop gain. Assume the intensity modulation responsivity is K_{AM}, the intensity modulation is $\Delta P = K_{AM} i_0 \sin \phi_e$ and the RIN is

$$r_s = \Delta P / P_0 = \frac{K_{AM}}{P_0} i_0 \sin \phi_e \tag{5.34}$$

where P_0 is the DC optical power. K_{AM} can be estimated from the slope of the P-I curve of the slave laser, i.e.,

$$K_{AM} = P_0 / \left(I - I_{th} \right) \tag{5.35}$$

where I_{th} is the threshold current. In Eq. (5.33) i_0 determines the holding range of the OPLL and can thus be calculated by

$$i_0 = \Delta f_h / K_{FM} \tag{5.36}$$

where Δf_h is the holding range and K_{FM} is the FM responsivity of the SCL. Substituting Eqs. (5.35) and (5.36) in Eq. (5.34) one obtains the RIN

$$r_s(t) = \frac{\Delta f_h}{(I - I_{th}) K_{FM}} \sin \phi_e(t) \tag{5.37}$$

Using the typical parameters of the IPS laser OPLL $\Delta f_h \approx 200MHz$, $I - I_{th} \approx 300mA$, $K_{FM} \approx 200MHz/mA$, Eq. (5.37) gives $r_s(t) = \frac{1}{300} \sin \phi_e(t)$. Thus the RIN introduced by the feedback current is at least two orders of magnitude smaller than the residual phase noise of the OPLL, and its effect on the combining efficiency can be neglected.

5.2.5 Effect of fiber amplifier phase noise

SCLs have relatively low output power. To achieve high average power, tens of thousands of SCLs need to be combined, which is very difficult to do. State-of-the-art fiber lasers or fiber amplifiers can emit single frequency beams of hundreds of watts with diffraction limited beam quality. An alternative option to obtain high average power is to use the locked slave laser to seed tens of high power fiber amplifiers, whose output beams are then coherently combined. Since CBC is very sensitive to phase noise, the phase noise introduced by the fiber amplifiers needs to be examined.

Historically there have been two different models proposed to explain the effects of fiber amplifier phase noise. The first model assumes that the amplified spontaneous emission (ASE) in the fiber amplifier adds a multiplicative phase term to the electrical field at the output of the optical amplifier[65, 66], i.e.,

$$E_{out}(t) = \sqrt{G} E_0 e^{i\phi(t)} . e^{i\omega t} . e^{i\phi_a(t)} \tag{5.38}$$

where E_0 is the amplitude of the signal at the amplifier input，G is the optical gain of the amplifier，$\phi(t)$ is the phase of the input signal, and $\phi_a(t)$ is the phase noise

introduced by the amplifier.

This multiplicative phase noise model predicts a linewidth broadening of the signal. Following the derivation in [66], one arrives at an expression for the linewidth broadening due to ASE in the fiber amplifier:

$$\delta\nu = \sqrt{\frac{n_{sp}^2 h\nu.\Delta\nu_s^3\left(G-1\right)^2}{4\pi G P_{in}}} \tag{5.39}$$

where n_{sp}~1 is the spontaneous emission factor, $\Delta\nu_s$ is the input signal linewidth, ν is the optical frequency, and P_{in} is the power of the input signal.

It was further pointed out in [66] that if the effect of ASE is taken into account only over the fiber amplifier bandwidth B_0, the predicted linewidth broadening is much smaller, given by

$$\delta\nu = \frac{n_{sp} h\nu B_0\left(G-1\right)}{4\pi G P_{in}} B_0 \tag{5.40}$$

However, more recent investigations into fiber amplifier phase noise have revealed that this multiplicative model may not be accurate[67, 68]. Instead, an additive noise model has been proposed, where the output field is given by

$$E_{out}(t) = \sqrt{G}E_0 e^{i\phi(t)}.e^{i\omega t} + E_n.e^{i\omega t}.e^{i\phi_a(t)} \tag{5.41}$$

where E_n is the amplitude of the ASE noise within the signal bandwidth. The signal-to-noise ratio of an unsaturated fiber amplifier is given by [39]

$$\left(\frac{S}{N}\right)_{output} = \frac{P_{in}}{\mu h\nu\,\Delta\nu_s}\frac{G}{G-1} \tag{5.42}$$

where μ is the population inversion factor ($\mu \approx 1$).

Since the predicted linewidth broadening (Eq. (5.39) or (5.40)) of the first model can be much smaller than the signal linewidth, a self-heterodyne balanced interferometer experiment as shown in Fig. 5.8(a) is usually employed to measure the linewidth broadening. This measurement removes the phase noise of the laser source, and is therefore more sensitive[68]. In this measurement, when the fiber amplifier is turned off,

one should see a delta function as shown in Fig. 5.8(b). When the amplifier is on, if the phase noise is multiplicative, one expects to see a Lorenzian lineshape as given in Fig. 5.8(c). If the phase noise is additive, one expects to see a delta function with a Lorenzian pedestal, whose width is determined by the sum of the laser and amplifier phase noise. The ratio of the signal power to the noise power (area under the Lorenzian pedestal) is given by Eq. (5.42).

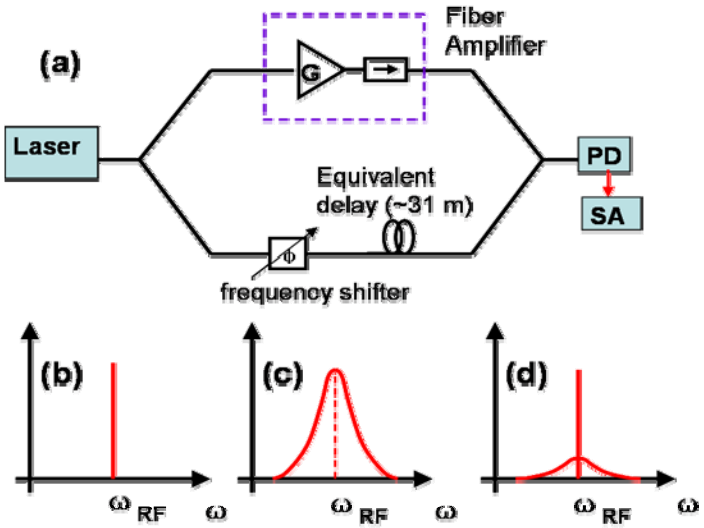

SA: Spectrum analyzer, PD: photodetector

Fig. 5.8 (a) Self-heterodyne fiber amplifier phase noise measurement setup. (b)-(d) Predicted beat spectra with (b) no amplifier noise, (c) multiplicative phase noise, and (d) additive phase noise

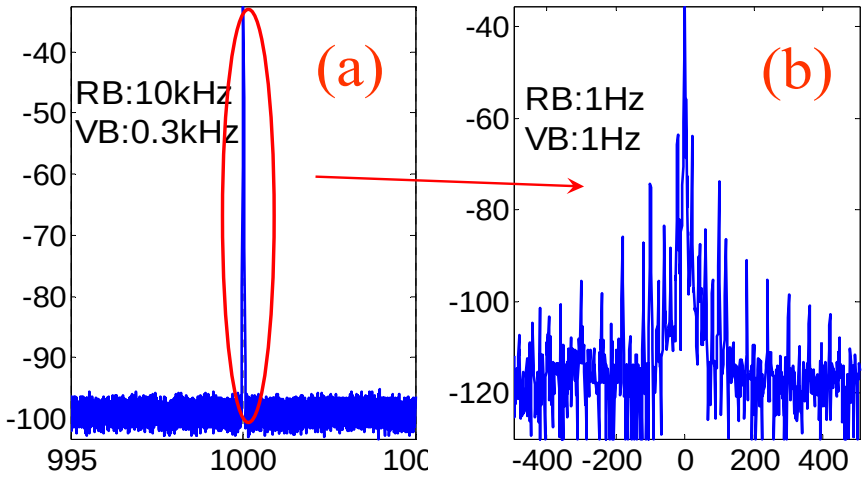

Fig. 5.9 Experimental results of the self-heterodyne fiber amplifier phase noise

measurement with span of (a) 10MHz and (b) 1kHz

I conducted a self-heterodyne balanced interferometer experiment as shown in Fig. 5.8(a). A 1064 nm IPS external cavity SCL is used to seed a Nufern 3 W Yb-doped fiber amplifier. A phase modulator is used as the frequency shifter. In Fig. 5.9, I plot the measured spectrum with a span of 10 MHz and 1kHz. I see neither any observable linewidth broadening down to the resolution limit of the spectrum analyzer (~ 1 Hz) nor a noise pedestal down to the noise floor (67 dB below the signal level). However Fig. 5.9(b) shows the presence of many noise peaks, which are mainly the harmonics of the power line frequency (60 Hz) and are more than 20dB lower than the signal. This noise results from the acoustic noise picked up by the fiber. I replaced the amplifier with a passive fiber of equivalent length (~30m) and observed the same noise peaks.

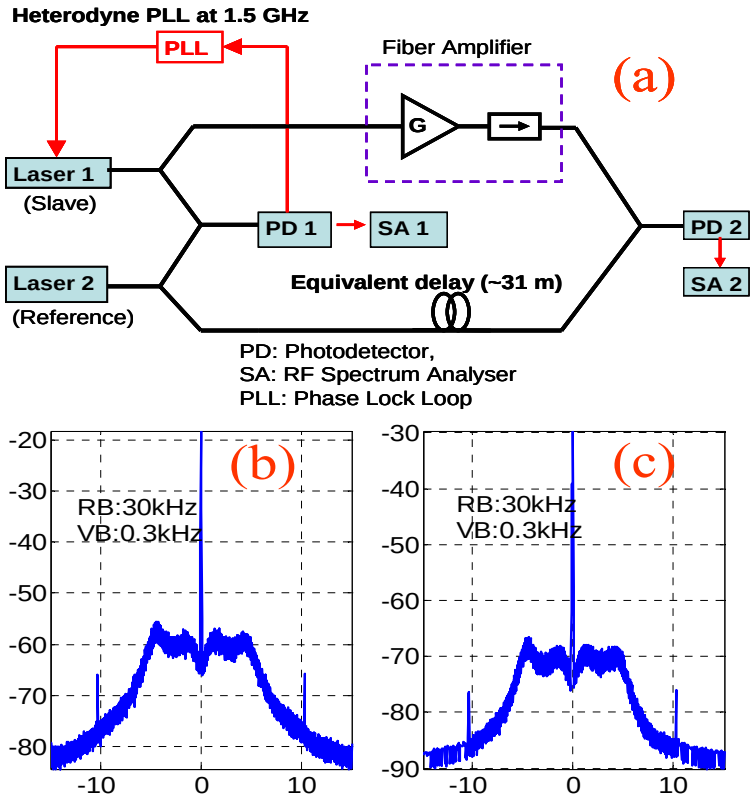

Fig. 5.10 (a) Experimental setup to measure the fiber amplifier phase noise added to the OPLL. (b) and (c) Beat spectra at the photodetectors PD1 and PD2 in (a).

I also performed a direct measurement of the amplifier phase noise added to the OPLL as shown in Fig. 5.10(a). The slave laser is phase locked to the master laser with a frequency offset ω_{os}, amplified and then beat with the master laser in a balanced interferometer to remove the effect of the master laser phase noise. Comparing Fig. 5.10(b) to Fig. 5.10(c), I do not see any effect of phase noise added by the amplifier. In fact, the multiplicative phase noise model[66] predicts a linewidth broadening of less than 1Hz for an laser linewidth of 500 kHz, fiber amplifier gain of 40, and an input power level of 75 mW in our case. The additive phase noise model predicts a signal-to-noise ratio[39] of ~120 dB. In either case, the effect of ASE in the fiber amplifier is far below our measurement sensitivity and can be safely neglected compared to the other factors reducing the combining efficiency. While the amplifier does introduce a lot of thermal phase variation [25] and picks up acoustic noise, these variations are at very low frequency compared to the VCO loop bandwidth of ~100kHz discussed in chapter 4 and should be significantly suppressed by the VCO loops.

5.3 Conclusion

In Chapters 4 and 5, I have presented a detailed study using OPLLs to coherently combine optical beams. The full electronic servo system enabled by the OPLLs technology eliminates the need for optical phase shifters and should significantly reduce the cost and size of the system. In the preliminary experiment of combining two laser beams, a promising combining efficiency of 94% is achieved. This approach can be applied to both tiled-aperture and filled-aperture CBC implementations. In either case, the efficiency penalty due to the residual phase noise of the OPLLs is less than 2% if IPS external cavity lasers are used. In the filled-aperture approach, the efficiency penalty caused by the phase error in the VCO loops and the phase front deformation scales up as $\sim\log_2 N$. This poses a serious challenge if a large number of beams are to be combined.

Fortunately, with the power of single-mode fiber amplifiers reaching hundreds of watts and even kilowatts, combining tens of beams can scale the power up to the regime of 10kW or even 100kW.

Chapter 6 Coherence cloning using OPLLs

6.1 Introduction

Ultra-stable lasers with narrow linewidth and long coherence length are required for applications such as various types of interferometric sensing, Doppler LIDAR, gas detection, frequency metrology, RF signal generation, and coherent communications[4, 40, 69, 70]. The requirement of the linewidth could vary from MHz to sub Hz, depending on the particular application. For the short distance fiber optical sensing, linewidths of a few kHz might be enough. For ground based or space borne gravitational wave detection (VIRGO, LIGO) [71], or RF reference signal distribution in large radiotelescope arrays (ALMA) [71], accurate measurement of tens to millions of km with a resolution of sub micrometer requires the laser to have a sub-Hz linewidth[71].

To achieve a narrow linewidth, an extended optical cavity with very high quality factor is usually used. For example, gas lasers, solid state lasers or fiber lasers with long cavity can have linewidth of a few kHz [72]. Electrical feedback can also be used to further narrow the linewidth of the laser. Very stable Fabry-Perot intefereometers with very high finesse, or the narrow absorption lines of certain gases have been used as frequency discriminators to detect and reduce a laser's frequency noise over a limited frequency bandwidth[40, 70]. Using this approach, lasers with linewidths of sub-Hz have been demonstrated for precision frequency standard synthesis with optical clocks[30, 31]. However these lasers are typically bulky and very expensive due to the complexity of the frequency stabilizing system.

Semiconductor lasers typically have linewidth of between a few hundred kHz and a few MHz due to the low reflectivity of the laser waveguide facet and the linewdith broadening effect[73-76]. Using optical feedback from an external cavity, their linewidths can be reduced to a few kHz. However, the long laser cavity makes it more challenging to achieve stable single frequency operation, and a great deal of effort is necessary for packaging to mechanically isolate the cavity. The linewidth of SCLs has also been

reduced with the electric feedback approach using either a Fabry-Perot interferometer or the absorption line of gases[40, 70]. No matter which approach is used, the advantages of SCLs such as their small size and low cost are lost.

In an ideal OPLL, the slave laser tracks the phase of the master laser instantaneously and thus inherits the coherence property of the master laser. It only takes low cost SCLs and electronic circuits to make OPLLs, which provides an economic way of cloning the superior coherence property of an expensive master laser. This could be very attractive for applications where a large number of coherent laser sources are needed.

Another advantage of heterodyne OPLL is the additional flexibility of controlling the frequency of the slave laser by using an RF offset signal. Once a fixed frequency standard is established, e.g., using a gas absorption line or an optic clock, a tunable narrow linewidth laser source can be made using the heterodyne OPLL technology. A frequency tuning range of up to 100GHz can be achieved with the state-of-the-art RF electronics[21].

In this chapter I will study the cloning of the coherence of a narrow linewidth laser to inexpensive off-the-shelf commercial SCLs with the OPLLs. I will first summarize the description of the frequency stability and the coherence of a single frequency laser. Different experimental methods of characterizing the frequency stability will also be discussed. Afterwards I shall give the theoretical calculation of the frequency or phase noise, the Allan deviation, the degree of coherence, and the lineshape of a SCL phase locked to a cleaner master laser. Finally the experimental measurements will be presented and discussed.

6.2 Phase noise and frequency stability of a single frequency laser

6.2.1 Phase and frequency fluctuations of an oscillator

The optical field of a single frequency laser is modeled as a quasimonochromatic field

$$E(t) = E_0 \exp j\left[2\pi v_0 t + \phi(t)\right] \tag{6.1}$$

where v_0 is the average optical frequency and $\phi(t)$ is the phase fluctuation. The intensity noise is not considered here because in semiconductor lasers its integrated power is much smaller than that of the phase noise.

The frequency stability of a laser can be characterized in both the time domain and the frequency domain. In the time domain, traditionally two random variables are widely used to characterize the frequency stability of an oscillator. They are the fractional phase fluctuation $x(t)$ and the fractional frequency fluctuation $y(t)$, which are defined as[77]

$$x(t) = \frac{\phi(t)}{2\pi v_0} \quad \text{and} \quad y(t) = \frac{\dot{\phi}(t)}{2\pi v_0} \tag{6.2}$$

Note that $x(t)$ also represents the time jittering of the clock signal described by Eq. (6.1). The absolute phase fluctuation is related to $x(t)$ by $\phi(t) = 2\pi v_0 x(t)$ and the absolute frequency fluctuation is $\dot{\phi}(t)/2\pi = v_0 y(t)$.

6.2.2 Power spectral density of the phase or frequency fluctuation

In actual experimental measurement people typically measure the single-sided power spectral density (PSD) of the fractional frequency fluctuation, i.e. , $S_y(f)$. The PSD of the fractional phase fluctuation, the absolute phase fluctuation, and the absolute frequency fluctuation are related to $S_y(f)$ by

$$S_x(f) = \frac{S_y(f)}{(2\pi f)^2}, \quad S_\phi(f) = (2\pi v_0)^2 S_x(f), \quad S_v(f) = v_0^2 S_y(f) \tag{6.3}$$

Actual experimental practice shows that the single-sided PSD of the fractional frequency fluctuations in most oscillators generally takes a polynomial form[2, 78]

$$S_y(f) = \sum_{\alpha=-2}^{2} h_\alpha f^\alpha \tag{6.4}$$

with
- α=2: white phase noise
- α=1: flicker phase noise
- α=0: white frequency noise
- α=-1: flicker frequency noise
- α=-2: random walk frequency noise

Depending on the detailed composition of an oscillator, the PSD of the frequency fluctuation can have a few non-zero polynomial components. Low values of "a" have not been clearly identified yet because of experimental difficulties related to very long term data acquisition and to the control of experimental conditions for long time. In practice the finite duration of measurements introduces a low frequency cutoff which prevents the divergence of $S_y(f)$ as $f \to 0$ for a<0. Furthermore, low pass filtering is always present in the measuring instruments, which ensures convergence conditions at the higher-frequency side of the power spectrum.

Experimental studies of the power spectral density of frequency noise and the lineshape have shown that the main contributions in single-mode semiconductor lasers are the white frequency noise due to spontaneous emission, and the 1/f flicker noise due to the fluctuation of charge carriers[32, 79-82]. The white frequency noise leads to the well known Lorentzian lineshape and the presence of the 1/f noise leads to a Voigt profile resulting from the convolution of a Lorentzian lineshape with a Gaussian lineshape[32, 80]. The 1/f noise dominates at low frequency and becomes pronounced only in measurements of long duration. In the following theoretical description I only consider the white frequency noise for the sake of simplicity.

6.2.3 Autocorrelation, coherence and linewidth of an optical field

The autocorrelation of the field and its temporal coherence are very important concepts widely used in many interferometric measurements. The optical field autocorrelation function is a measurement of the coherence between an optical signal and the delayed

version of itself, i.e.,

$$G_E^{(1)}(\tau) = \left\langle E^*(t)E(t+\tau)\right\rangle = \left\langle \exp\left[j\Delta\phi(t,\tau)\right]\right\rangle \exp(j\omega_0\tau) \tag{6.5}$$

where τ is the delay time, $\Delta\phi(t,\tau) = \phi(t+\tau) - \phi(t)$ is the phase jitter between time t and $t+\tau$, and $\langle\ \rangle$ represents averaging over infinite time. The Fourier transform of $G_E^{(1)}(\tau)$ gives the spectrum, or the lineshape, of the optical field.

In general it is very difficult to calculate the field autocorrelation function given by Eq. (6.5). For the spontaneous emission induced quantum phase noise, the phase jitter $\Delta\phi(t,\tau)$ is assumed to be a zero-mean stationary random Gaussian process[83-86]. With this assumption, one can use the well known relation [87]

$$\left\langle \exp\left[\pm j\Delta\phi(t,\tau)\right]\right\rangle = \exp\left[-\left\langle\Delta\phi^2(\tau)\right\rangle/2\right] \tag{6.6}$$

and the laser field autocorrelation function is simplified to

$$G_E^{(1)}(\tau) = \exp\left[-\frac{1}{2}\left\langle\Delta\phi^2(\tau)\right\rangle\right]\exp(j\omega_0\tau) \tag{6.7}$$

The absolute value of $G_E^{(1)}(\tau)$ as a function of τ can be used to measure the degree of coherence of an optical field. The mean square phase jitter $\left\langle\Delta\phi^2(\tau)\right\rangle$ is related to the single-sided frequency noise spectrum $S_\nu(f)$ by[87]

$$\left\langle\Delta\phi^2(\tau)\right\rangle = 4\int_0^{+\infty}\sin^2(\pi f\tau)S_\nu(f)\frac{df}{f^2} \tag{6.8}$$

Next I will use two examples to illustrate how the degree of coherence and the lineshape of the field can be obtained from the PSD of the frequency fluctuation.

6.2.4 Example: white frequency noise

White frequency noise due to spontaneous emission is the primary noise source in semiconductor lasers. The corresponding single-sided PSD is $S_\nu(f) = \Delta f/\pi$ [39, 73, 84],

leading to the mean square phase jitter $\left\langle \Delta\phi^2(\tau) \right\rangle$ increasing linearly with the delay τ

$$\left\langle \Delta\phi^2(\tau) \right\rangle = 2\pi\Delta f |\tau| \tag{6.9}$$

where Δf is the FWHM of the laser spectrum. Substituting Eq. (6.9) into Eq. (6.7), the degree of coherence is simply an exponentially decaying function

$$\left| G_E^{(1)}(\tau) \right| = \exp\left[-\pi\Delta f \tau \right] \tag{6.10}$$

By taking the Fourier transform of the autocorrelation function, the normalized lineshape corresponding to the white frequency noise exhibits the well known Lorentzian shape

$$S_E(f) = \frac{\Delta f / 2\pi}{(\Delta f / 2)^2 + (f - f_0)^2} \tag{6.11}$$

6.3 Experimental methods of measuring the frequency stability

The experimental characterization of the frequency stability or coherence of a single frequency laser can be conducted both in the time domain and the frequency domain. In the time domain, a frequency counter can be used to record the beat note between two independent lasers, where either the reference laser has significantly lower noise than the device under test, or both lasers have similar performance. This method can achieve very high resolution. However, it requires a second laser and can be inconvenient. In the frequency domain, one can convert frequency fluctuations into intensity fluctuations using a frequency discriminator, such as an unbalanced Mach Zehnder interferometer or a high-finesse reference cavity[38]. By measuring the PSD of the resultant intensity fluctuations, one obtains the PSD of the frequency fluctuations.The linewidth or lineshape of the optical field is another indicator of the coherence of a single frequency laser. To measure the linewidth or lineshape, one often uses the delayed self-heterodyne inteferometer (DSHI) technique, which involves measuring the beat note between the

laser output and a frequency-shifted and delayed version of itself.

6.3.1 Time domain measurement of the frequency fluctuation

Assuming that a frequency counter is used to measure the fractional frequency averaged over time interval $[t_k, t_k + \tau]$

$$\bar{y}_k = \frac{1}{\tau}\int_{t_k}^{t_k+\tau} y(t')\,dt' \tag{6.12}$$

If the time interval between two consecutive measurements is *T*, the *N*-sample variance of $\bar{y}_k$ will be

$$\sigma_y^2(N,T,\tau) = \frac{1}{N-1}\sum_{k=0}^{N-1}\left(\bar{y}_k - \frac{1}{N}\sum_{k=0}^{N}\bar{y}_k\right)^2 \tag{6.13}$$

The dependence of the expectation value of the *N*-sample variance on the number of samples *N*, the sample time τ, and the power spectral density has been considered by Allan[88]. It can be shown that the computation of the average of the *N*-sample variance introduces a filtering of the PSD $S_y(f)$ [77]

$$\left\langle \sigma_y^2(N,T,\tau)\right\rangle = \int_0^\infty S_y(f)\left|H(f)\right|^2 df \tag{6.14}$$

where $H(f)$ is the transfer function of a linear filter

$$H(f) = \frac{N}{N-1}\left[\frac{\sin \pi f\tau}{\pi f\tau}\right]^2\left\{1-\left[\frac{\sin \pi fNT}{N\sin \pi fT}\right]^2\right\} \tag{6.15}$$

The expectation value of the two-sample variance without dead time, i.e., $N = 2$ and $T = \tau$, is called the Allan variance and is generally accepted as the measure of frequency stability in the time domain. One sets

$$\begin{aligned}\sigma_y^2(\tau) &= \left\langle \sigma_y^2(2,\tau,\tau)\right\rangle = \frac{1}{2}\left\langle \left(\bar{y}_{k+1}-\bar{y}_k\right)^2\right\rangle \\ &= 2\int_0^\infty S_y(f)\frac{\sin^4(\pi f\tau)}{(\pi f\tau)^2}df\end{aligned} \tag{6.16}$$

The square root of the Allan variance is called the Allan deviation $\sigma_y(\tau)$.

The Allan deviation is useful for characterizing a frequency source because of the type of phase noise present is revealed by the dependence of $\sigma_y(\tau)$ on τ. For example, for white frequency noise, $\sigma_y(\tau) \propto \tau^{-1/2}$. For the Allan deviation to reliably reflect the type of noise present, it is crucial that there should be no dead time between consecutive average frequency measurements used to determine $\sigma_y(\tau)$.

6.3.2 Frequency domain measurement

In this section I introduce the different methods of measuring the frequency fluctuation and lineshape of lasers in the frequency domain.

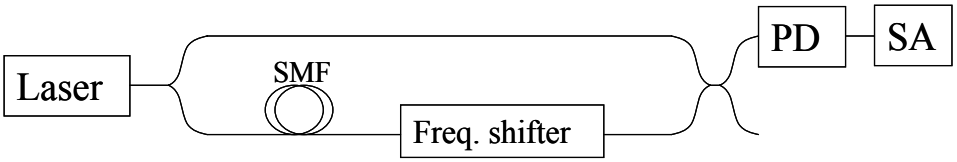

Fig.6.1 Schematic diagram of the delayed self-heterodyne interferometer lineshape measurement setup

Fig. 6.1 gives a schematic diagram of the delayed self-heterodyne interferometer setup. The delay line must be longer than the coherence length of the laser to measure the lineshape. It can also be used as a frequency discriminator to measure the frequency noise spectrum if the delay is kept much shorter than the coherence length and the frequency shifter is removed. Assume the detected total field is a superposition of a laser field $E(t)$ expressed by Eq. (6.1) with a time-delayed and frequency-shifted image of itself[89]

$$E_T(t) = E(t) + \alpha E(t+\tau_0)\exp j2\pi\Omega t \tag{6.17}$$

α is a real factor which accounts for the amplitude ratio between the two mixed fields, Ω is the mean frequency difference between the two mixed fields.

The photo current is proportional to the optical field intensity. Assuming stationary fields, to find the spectrum of the photo current, one can calculate the autocorrelation function of the photocurrent

$$R_I(\tau) = e\eta G^{(2)}_{E_T}(0)\delta(\tau) + \eta^2 G^{(2)}_{E_T}(\tau) \tag{6.18}$$

where e is the electronic charge, η is the detector sensitivity, and $G^{(2)}_{E_T}(\tau)$ is the second-order optical field correlation function defined as

$$G^{(2)}_{E_T}(\tau) = \left\langle E_T(t) E_T^*(t) E_T(t+\tau) E_T^*(t+\tau) \right\rangle \tag{6.19}$$

The first term in Eq. (6.18) is the short noise associated with the DC component of the photocurrent.

6.3.2.1 Power spectral density of the frequency noise

A rigorous analysis of the output of a homodyne frequency discriminator can be obtained by taking the Fourier transform of Eq. (6.19), which is studied in detail in [89]. It involves multiple integrations and is numerically complicated to calculate. A much simpler relation between the photocurrent spectrum and the laser frequency noise spectrum can be found if certain requirements are met.

Assuming that the mixed fields have the same amplitudes, and ignoring the shot noise, the photocurrent generated by the photodetector at one output of the homodyne FM discriminator is[38]

$$I = \eta E_T E_T^* = \eta E_0^2 \left\{ 2 + 2\cos\left[\omega_0 \tau_0 + \Delta\phi(t, \tau_0) \right] \right\} \tag{6.20}$$

where ω_0 is the average frequency of the optical field and τ_0 is the differential delay of the interferometer. The interferometer is typically biased at the quadrature point $\omega_0 \tau_0 = 2\pi N \pm \pi/2$ where the frequency discrimination sensitivity is the highest. If the phase jitter is small $\Delta\phi(t, \tau_0) << 1$, Eq. (6.20) can be simplified to

$$I \approx \pm 2\eta E_0^2 \Delta\phi(t,\tau_0) \tag{6.21}$$

Taking the Fourier transform of Eq. (6.21), the relation between the photocurrent spectrum and the frequency noise spectrum is found to be

$$S_I(f)/(2\eta E_0^2)^2 = 4\pi^2\tau_0^2 \sin c^2(f\tau_0) S_\nu(f) \tag{6.22}$$

where $\sin c(x) = \sin \pi x / \pi x$. For frequencies much smaller than the free spectral range of the interferometer, i.e., $f\tau_0 << 1$, $\sin c^2(f\tau_0) \approx 1$ and $S_I(f)$ is proportional to $S_\nu(f)$. Thus the spectrum of the photocurrent is a direct measurement of the frequency noise spectrum of the laser. The sensitivity of the interferometer is proportional to τ_0. Therefore a long delay time τ_0 is preferred as long as it satisfies $f\tau_0 << 1$ in the frequency range of interest.

6.3.2.2 Self-delayed heterodyne measurement of the lineshape

In the case of the self-delayed heterodyne lineshape measurement, following Eq. (6.19) the second-order optical field autocorrelation function is [89]

$$G_{E_T}^{(2)}(\tau)/E_0^4 = \left[\left(1+\alpha^2\right)^2 + 2\alpha^2 \cos(2\pi\Omega\tau)\cdot\exp(-A)\right] \tag{6.23}$$

where A is

$$A = \left\langle\phi^2(\tau)\right\rangle + \left\langle\phi^2(\tau_0)\right\rangle - \left\langle\phi^2(\tau+\tau_0)\right\rangle/2 - \left\langle\phi^2(\tau-\tau_0)\right\rangle/2 \tag{6.24}$$

If the spectrum of the frequency noise is known, the mean-square phase jitter $\left\langle\Delta\phi^2(\tau)\right\rangle$ and thus the autocorrelation of the photocurrent can be calculated using Eq. (6.8) and Eq. (6.23). As an example, for white frequency noise, one can plug Eq. (6.9) in Eq. (6.23) to get

$$\frac{G_{E_T}^{(2)}(\tau)}{E_0^4} = \left(1+\alpha^2\right)^2 + 2\alpha^2 \cos\Omega\tau\cdot\exp\begin{cases} -|\tau| & \text{for } |\tau| < \tau_0 \\ -|\tau_0| & \text{for } |\tau| > \tau_0 \end{cases} \tag{6.25}$$

Assuming that the mixed signals have equal amplitudes, i.e. $\alpha = 1$ and ignoring the shot noise term, the spectrum of the photocurrent is obtained by taking the Fourier transform of Eq. (6.25)

$$\frac{S_I(f)}{\eta^2 E_0^4} = 4\delta(f) + \exp(-2\pi\Delta f \tau_0)\cdot\delta(f-\Omega) + \frac{\Delta f/\pi}{\Delta f^2 + (f-\Omega)^2}\cdot \left\{1 - e\exp(-2\pi\Delta f\tau_0)\cdot\left[\cos 2\pi(f-\Omega)\tau_0 + \Delta f\frac{\sin 2\pi(f-\Omega)\tau_0}{(f-\Omega)}\right]\right\} \tag{6.26}$$

For delay times much longer than the coherence time $\Delta f \tau_0 >> 1$, Eq. (6.26) reduces to

$$\frac{S_I(f)}{\eta^2 E_0^4} = \frac{\Delta f/\pi}{\Delta f^2 + (f-\Omega)^2} \tag{6.27}$$

which is a Lorentzian shape with a FWHM of $2\Delta f$.

6.4 Coherence cloning using OPLLs

In Chapter 2 I pointed out that the slave laser is forced to track the phase and frequency of the master laser in an OPLL. In an ideal OPLL with infinite bandwidth, the slave laser has the same phase as the master laser and thus should inherit the coherence property of the master laser. In Section 2.4 I derived the phase noise of the locked slave laser without taking into account the relative intensity noise (RIN). As a matter of fact, the RIN of the master laser could transfer to the phase variation of the slave laser through the feedback loop, particularly if the RIN of the master laser is significant within the bandwidth of the loop. Due to the gain saturation effect of semiconductor lasers, the RIN of SCLs in an OPLL is significantly lower than the residual phase noise and can be ignored. This assumption will be further justified later by our experimental observations. Taking into account the RIN of the master laser, I will derive the phase noise of the slave laser in the OPLL.

If one assumes that the master laser has a power of $P_m = P_{m0}(1+r)$ where r

represents the RIN, and that the slave laser has a power of P_s, the feedback current reflecting the phase error is

$$i(t) = R_{pd}\sqrt{P_{m0}(1+r)P_s}\sin\phi_e(t) \tag{6.28}$$

where R_{pd} is the responsivity of the photodetector, and $\phi_e = \phi_m - \phi_s$ is the differential phase error between the master laser and the slave laser. ϕ_e can be written as the sum of a steady state value and the fluctuation, i.e., $\phi_e = \phi_{e0} + \phi_e^n$. Assuming small errors r, ϕ_e^n <<1, one can expand Eq. (6.28) to first order

$$i(t) = K_{pd}\left[\sin\phi_{e0}\cdot\left(1+\frac{r(t)}{2}\right)+\cos\phi_{e0}\cdot\phi_e^n(t)\right] \tag{6.29}$$

where K_{pd} is the photodetector gain. The constant term $K_{pd}\sin\phi_{e0}$ compensates for the free-running frequency difference between the master laser and the slave laser. Using Eq. (6.29) one can perform a small signal noise analysis similar to the analysis in Section 2.4. Fig. 6.2 is a schematic diagram of the small signal noise propagation in OPLLs. Here the shot noise of the photodetector is ignored. In addition to the phase error signal $K_{dc}\cos\phi_{e0}\cdot\phi_e^n(t)$, another term, $K_{dc}\sin\phi_{e0}\cdot r(t)/2$, is added due to the RIN of the master laser. The closed loop noise relation can be obtained as

$$\phi_s(s) = \phi_s^n(s) + G_{op}\cos\phi_{e0}\cdot\left[\phi_m(s)-\phi_s(s)\right]+G_{op}\sin\phi_{e0}\cdot r(s)/2 \tag{6.30}$$

where the open loop gain is defined as $G_{op} = K_{dc}F_f(s)F_{FM}(s)\exp(-s\tau_d)/s$, and K_{dc} is a constant representing the DC loop gain. After some algebra one obtains

$$\phi_s(s) = \phi_m\cdot\frac{G_{op}\cos\phi_{e0}}{1+G_{op}\cos\phi_{e0}}+\phi_s^n\cdot\frac{1}{1+G_{op}\cos\phi_{e0}}+\frac{r(s)}{2}\frac{G_{op}\sin\phi_{e0}}{1+G_{op}\cos\phi_{e0}} \tag{6.31}$$

The PSD of the phase noise of the locked slave laser is thus

$$S_\phi^s = S_\phi^m\cdot\left|\frac{G_{op}\cos\phi_{e0}}{1+G_{op}\cos\phi_{e0}}\right|^2+S_\phi^{s,fr}\cdot\left|\frac{1}{1+G_{op}\cos\phi_{e0}}\right|^2+\frac{S_{RIN}^m}{4}\left|\frac{G_{op}\sin\phi_{e0}}{1+G_{op}\cos\phi_{e0}}\right|^2 \tag{6.32}$$

where $S_{\phi}^{s,fr}$, S_{ϕ}^{m}, and S_{RIN}^{m}, are respectively, the PSD of the phase noise of the free-running slave laser, the master laser, and the RIN of the master laser. The PSD of the frequency noise is simply $S_{\nu}(f) = f^2 S_{\phi}(f)$.

Comparing with the phase noise of the locked slave laser derived in Section 2.4, in Eq. (6.31) and Eq. (6.32) contain an additional term, due to the RIN of the master laser. In general, the steady state phase error ϕ_{e0} is not zero and the RIN-induced residual phase noise needs to be carefully evaluated.

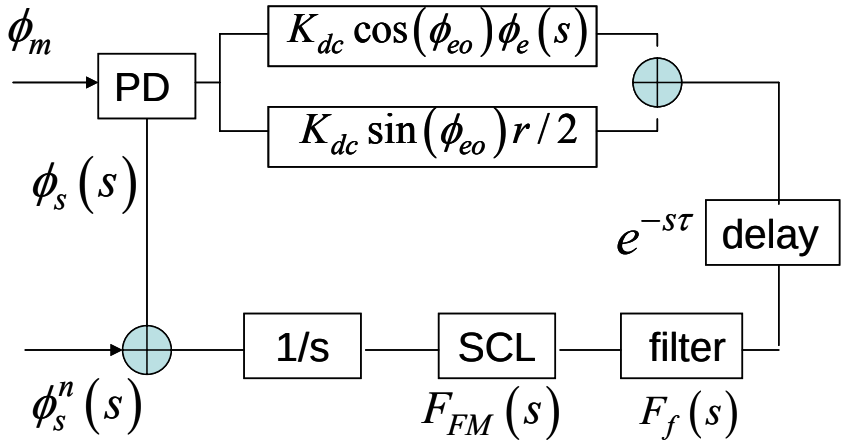

Fig. 6.2 Small signal noise propagation in an OPLL with the RIN of the master laser being considered

ϕ_m : phase of the master laser

ϕ_s : phase of the slave laser

ϕ_s^n : free-running phase noise of the slave laser

K_{dc} : loop DC gain

ϕ_{e0} : steady state differential phase error

$\phi_e(s)$: small signal differential phase error

r : relative intensity noise of master laser

$F_f(s)$: normalized transfer function of the loop filter

$F_{FM}(s)$: normalized transfer function of the current-frequency modulation response of the semiconductor laser

I will use the JDSU DFB laser as an example to simulate the frequency noise of a slave laser phase locked to a narrow linewidth master laser. For the purpose of simplicity, I assume that the frequency noises of both the master laser and the slave laser are white Gaussian and the RIN of the master laser can be ignored. The current-frequency modulation response of the JDSU laser obtained in section 3.1.2 is used in the simulation. In Fig. 6.3(a) the frequency noise of a free-running JDSU laser, a narrow linewidth master laser, and the locked JDSU laser are plotted. The frequency noises of the free-running lasers are assumed to be white Gaussian. In Fig. 6.3(b)-(d) the corresponding Allan deviation, degree of coherence and single-sided lineshape are also shown. The frequency noise of the JDSU laser tracks that of the master laser within the bandwidth of the loop, as does the Allan deviation, the degree of coherence, and lineshape. For frequencies bigger than the loop bandwidth, the frequency noise goes back to the free-running level and is even amplified at a few MHz, due to the insufficient phase margin of the feedback loop.

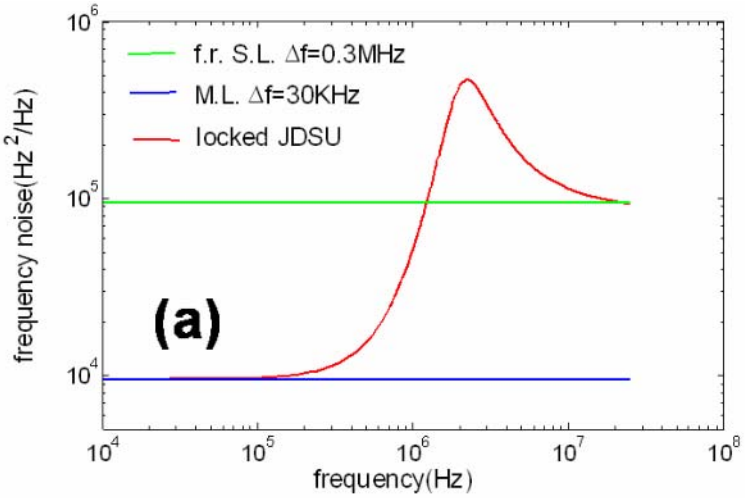

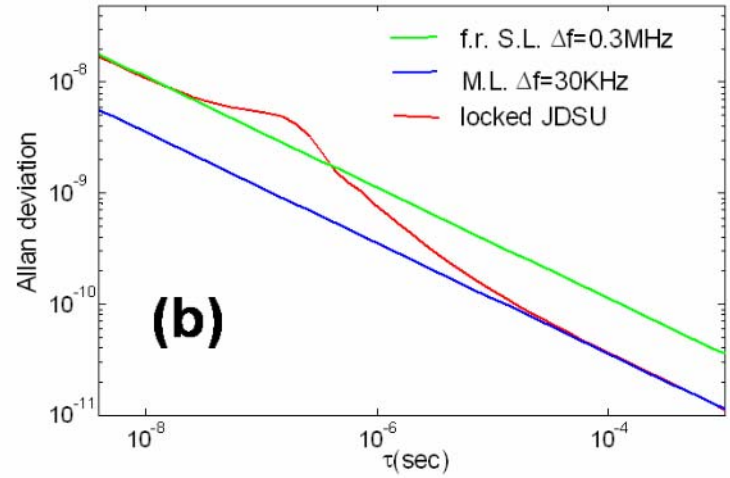

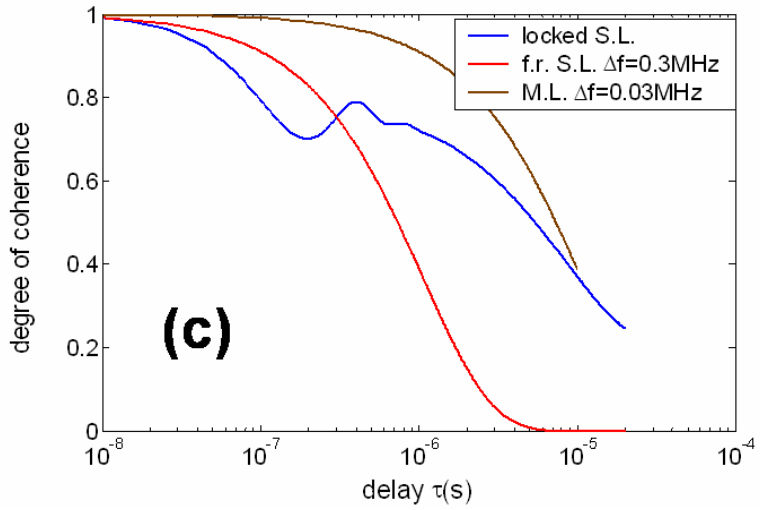

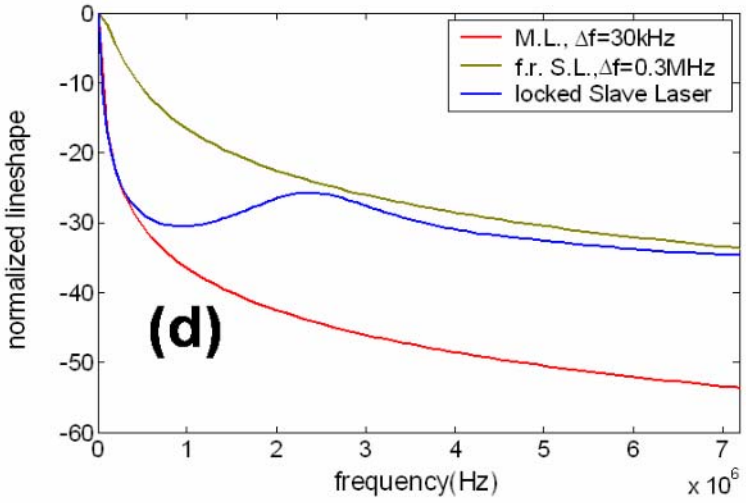

M. L.: master laser; S. L.:slave laser; f.r.: free-running

Fig. 6.3(a) Frequency noise, (b) Allan deviation, (c) degree of coherence and (d) single-sided lineshape of the free-running and phase locked JDSU DFB laser. White frequency noise is assumed for the free-running master and slave lasers. In the simulation I have assumed a loop gain margin of G_{mg}=10dB and used the FM response of the JDSU laser obtained in Section 3.1.2.

6.5. Experimental measurement

In this section, I will present the experimental measurement of the relative intensity noise (RIN), the frequency noise, and the lineshape of the master laser, the free-running slave laser and the locked slave laser. To measure the RIN, the optical signal is fed into a photodetector, whose output is then measured with a RF spectrum analyzer. The lineshape is measured using the delayed self-heterodyne interferometer displayed in Fig. 6.1. A similar setup is used to measure the frequency noise where the frequency shifter is removed and the delay length of the fiber is much shorter than the coherence length of the laser.

6.5.1 Measurement of the Agilent laser

6.5.1.1 RIN of the Agilent laser

I first measure the RIN of the Agilent laser, which will be used as the master laser to lock the JDSU DFB laser. Fig. 6.4(a) shows the measured RIN of the Agilent laser. The Agilent tunable laser is an external cavity semiconductor laser of relatively long cavity length and the RIN is significant from a few hundreds of kHz to a few MHz due to the relaxation resonance effect[39, 90].

I have pointed out in Section 6.4 that the RIN of the master laser can transfer to the frequency noise of the slave laser through the feedback loop. One can use Eq. (6.32) to evaluate the residual frequency noise of the locked slave laser due to the RIN of the master laser, and compare it with the residual frequency noise due to the free-running

frequency noise of the slave laser. In the calculation I use $\sin\phi_{e0}=1$ for an upper bound estimation. I also use the JDSU DFB as the slave laser and assume that it has a white frequency noise corresponding to a FWHM of 0.3MHz. The results are plotted in Fig. 6.4(b). As can be seen, the blue curve is orders of magnitude lower than the red curve. Thus the residual frequency noise coupled from the RIN of the Agilent laser can be neglected.

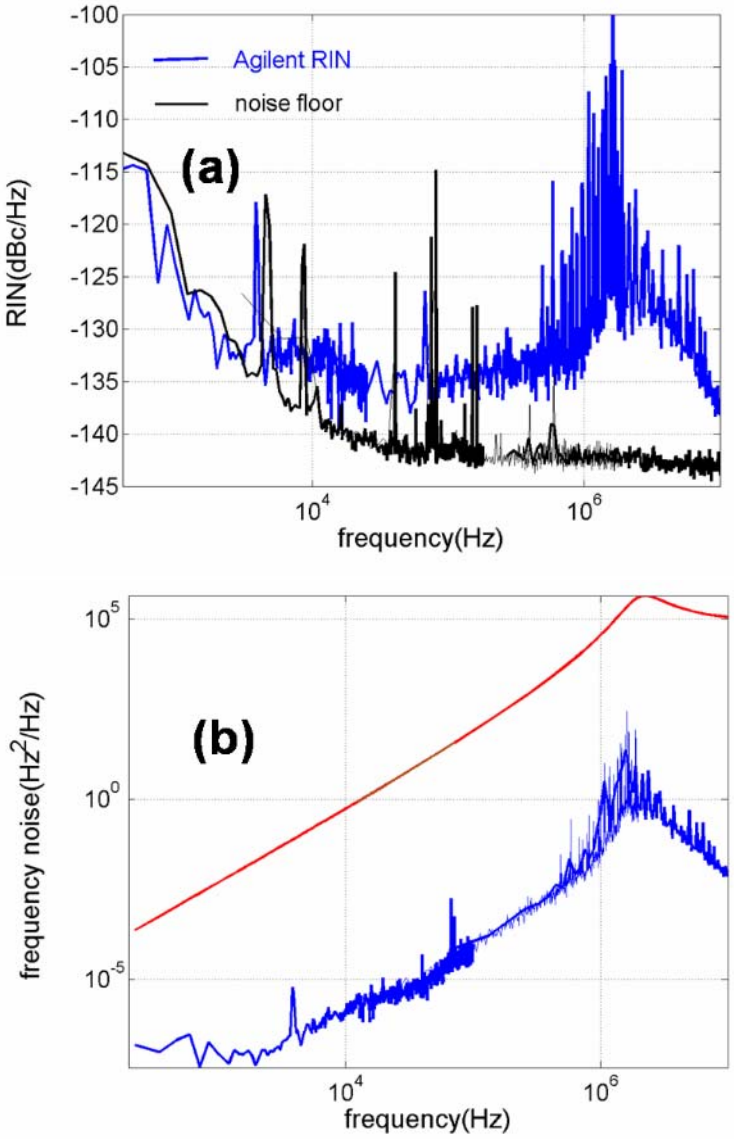

Fig. 6.4(a) Measured RIN of the Agilent laser. The black curve is the instrument noise floor. (b) Comparison of the residual frequency noise of the locked slave laser due to

the free-running noise of the slave laser (red curve) and the RIN of the Agilent laser (blue curve). In the calculation I have used Eq. (6.32) and assumed that the slave laser possesses a FWHM of 0.3MHz.

6.5.1.2 Frequency noise of the Agilent laser

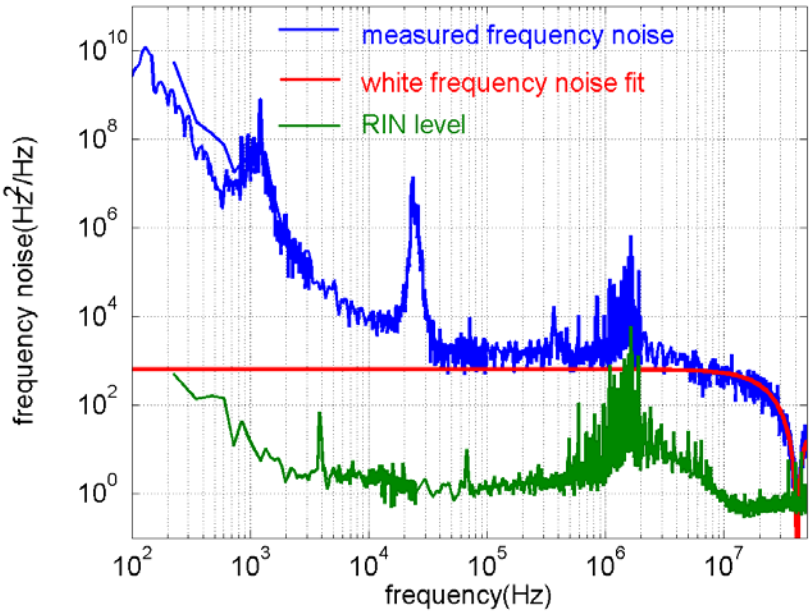

Fig. 6.5. Measured frequency noise (blue curve) of the Agilent laser. The red curve is a theoretical fitting assuming a white frequency noise corresponding to 2kHz FWHM linewidth. The dip at about 40MHz is given by the free-spectral-range of the Mach Zehnder interferometer of ~5m differential delay. The green curve represents the contribution of the RIN in the frequency noise measurement.

To measure the frequency noise of the Agilent laser I use a Mach Zehnder interferometer with a differential delay of ~5m. The blue curve in Fig. 6.5 is the measured frequency noise $S_\nu(f)$ (Hz^2/Hz) after the calibration. The red curve is a theoretical fit using Eq. (6.22), assuming a white frequency noise corresponding to a FWHM of 2kHz. In deriving Eq. (6.22), I have ignored the intensity noise. To consider the intensity noise one can

modify the quadrature-biased interferometer output (Eq. (6.22)) to

$$S_I(f)/(2\eta E_0^2)^2 = S_{RIN}(f) + 4\pi^2\tau_0^2 \sin c^2(f\tau_0) S_\nu(f) \tag{6.33}$$

Eq. (6.33) indicates that the calibrated frequency noise shown in Fig. 6.5 is actually the summation of the RIN $S_{RIN}(f)$ multiplied by a factor of $1/\left(4\pi^2\tau_0^2\right)$, and the frequency noise $S_\nu(f)$ multiplied by a factor of $\sin c^2(f\tau_0)$. Using the measured RIN shown in Fig. 6.4(a), I also calculate the normalized RIN $S_{RIN}(f)/4\pi^2\tau_0^2$ and plot it in Fig. 6.5. As can be seen, the contribution of the RIN is at least two orders of magnitude lower than the measured frequency noise. Thus one can neglect the effect of the RIN in the frequency noise measurement.

The frequency noise of the Agilent laser at frequency above ~30kHz is mainly white with significantly higher noise between ~100kHz and ~10MHz due to the intensity-frequency noise coupling. At frequency lower than 30kHz, higher order frequency noises such as f^{-1} and f^{-2} noises dominate.

6.5.1.3 Lineshape of the Agilent laser

To measure the lineshape I use the delayed self-heterodyne interferometer. Due to the frequency jitter, the measured lineshape and linewidth depend on the differential delay time of the interferometer[32, 82]. With a fiber delay of 500m, the mixed signals are still coherent and interference fringes can be seen on the spectrum. When the delay length is increased to 4km, the signals are almost incoherent. Fig. 6.6 gives the measured lineshape(green curve) of the Agilent laser with a fiber delay of 4km. The 20dB full width is about 0.46MHz.

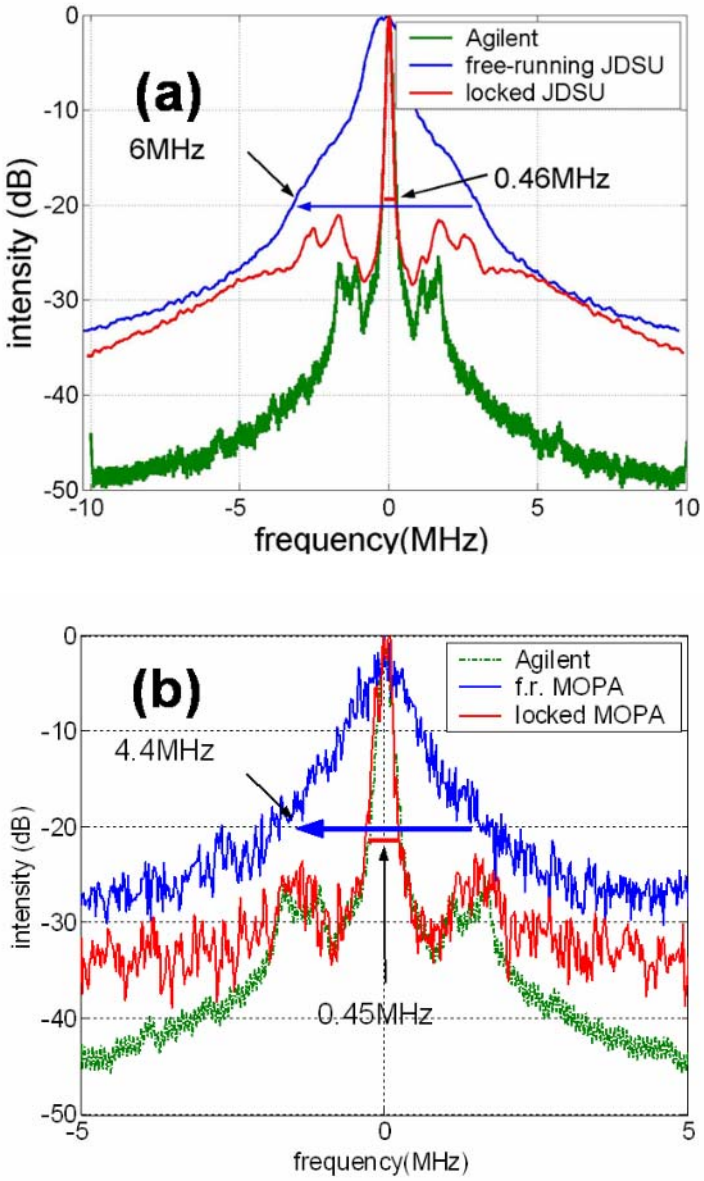

Fig. 6.6 Delayed self-heterodyne lineshape measurement of the master laser, the free-running slave laser, and the locked slave laser. (a) A JDSU DFB is used as the slave laser and (b) A QPC MOPA is used as the slave laser. The master laser is an Agilent tunable laser.

6.5.2 Measurement of the free-running and locked JDSU DFB laser

I repeated similar measurements on the JDSU DFB laser. The measured RIN and

frequency noise of the free-running JDSU DFB laser are plotted in 6.7(a) and 6.7(b). The RIN measurement is limited by the instrument noise floor at frequency smaller than ~1MHz and by the shot noise at higher frequencies. As seen in Fig. 6.7(b), the frequency noise agrees well with the theoretical fit assuming a white frequency noise corresponding to a FWHM of 0.3MHz. The lineshape is measured with the same interferometer of 4km differential delay and plotted by the blue curve in Fig. 6.6(a).

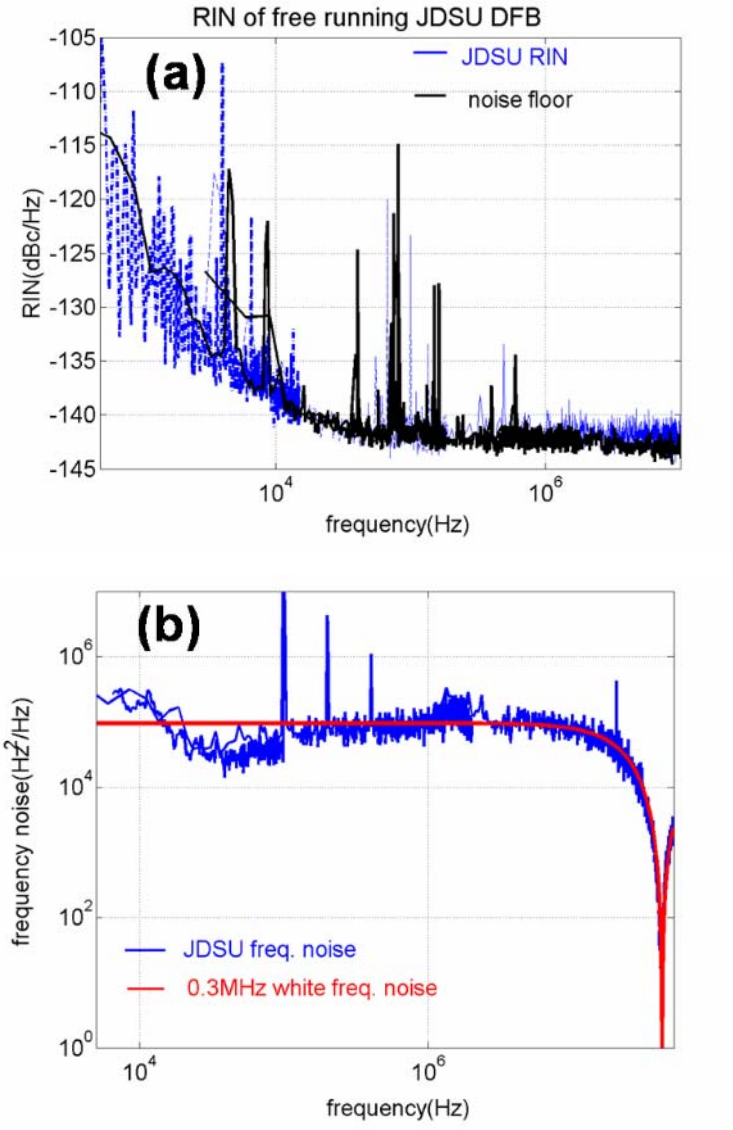

Fig. 6.7 Measured (a) RIN and (b) frequency noise of the free-running JDSU DFB laser. In (b), the red curve is a theoretical fitting assuming a white frequency noise corresponding to a FWHM linewidth of 0.3MHz.

I next phase locked the JDSU laser to the Agilent laser and measured its RIN, frequency noise, and lineshape. The RIN of the locked JDSU laser is similar to the free-running case and its measurement is limited by the instrument and shot noise floor. The low RIN justifies the assumption in deriving Eq. (6.28) that the RIN of the slave laser can be neglected when one analyze the residual frequency noise of the slave laser in the OPLLs.

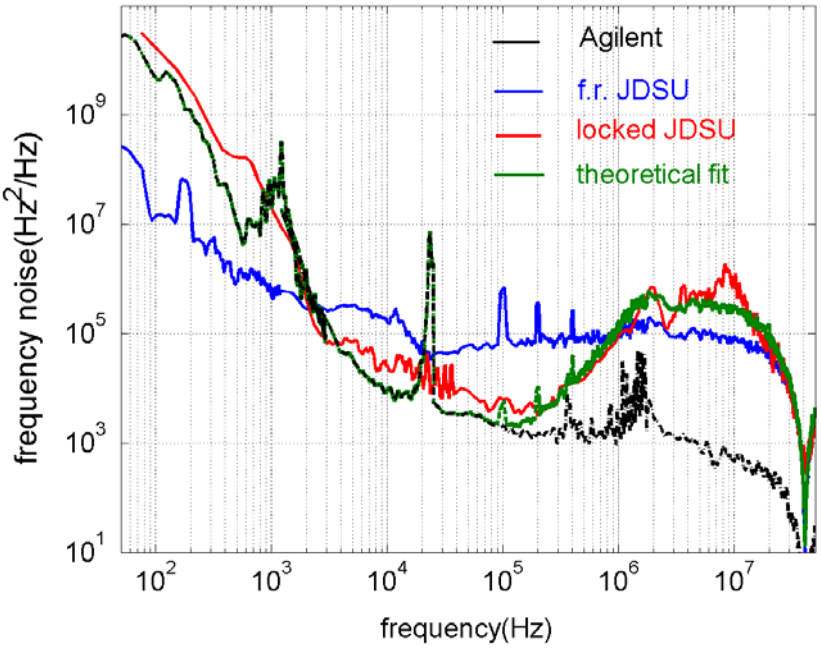

Fig. 6.8 Comparison of the frequency noise of the Agilent master laser (black curve), the free-running (blue curve), and the phase locked JDSU slave laser(red curve). The green curve is a theoretical fitting of the frequency noise of the locked JDSU laser using the measured frequency noise of the free-running JDSU laser, the Agilent laser, and the loop transfer function. The measured data shown here are smoothed with a 5 points moving average algorithm.

The measured frequency noise of the locked JDSU laser is plotted in Fig. 6.8 and compared to the free-running JDSU laser and the Agilent laser. As can be seen, the frequency noise of the locked slave laser follows that of the master laser for frequencies

smaller than ~100kHz. The frequency noise is reduced between ~2kHz and ~1MHz and increased for frequency less than ~2kHz due to the higher frequency noise of the master laser at low frequency. It is also amplified between 1MHz and 20MHz due to the insufficient phase margin of the loop.

With the knowledge of the frequency noises of the free-running JDSU laser, the Agilent master laser and the loop transfer function, one can theoretically calculate the frequency noise of the locked JDSU laser using Eq. (6.32) and compare it to the measurement. The calculation is also plotted in Fig. 6.8 by the green curve. The theoretical calculation agrees reasonably well with the measured result (red curve).

The measured lineshape of the locked JDSU laser is plotted in Fig. 6.6(a) as the red curve. Compared to the free-running case (blue curve), the lineshape of the locked JDSU laser is significantly narrowed within the bandwidth of the OPLL(<1MHz). The 20dB full width is reduced from 6MHz to 0.46MHz. The linewidth of the locked slave laser is limited by the linewidth of the master laser.

6.5.3 Measurement of the NP fiber laser and the locked JDSU laser

Fiber lasers are well known for their narrow linewidth and low phase noise[72]. In this section I will use a spectrally stabilized NP photonics fiber laser as the master laser to lock the JDSU DFB laser, then measure and compare their noise properties.

I first measured the RIN, the frequency noise, and the lineshape of the NP fiber laser. Fig. 6.9(a) is the measured RIN of the NP fiber laser under the free-running mode operation (red curve) and the RIN suppression mode operation (blue curve). The spectral peak at ~1MHz is caused by the relaxation resonance effect[39, 90] of the fiber laser. The black curve is the instrument noise floor. I further use Eq. (6.32) to calculate and compare the residual frequency noise of the locked slave laser due to its free-running frequency noise and to the RIN of the NP fiber laser under the RIN suppression mode operation.

The results are plotted in Fig. 6.9(b). The RIN-induced residual frequency noise is significantly lower and can be neglected.

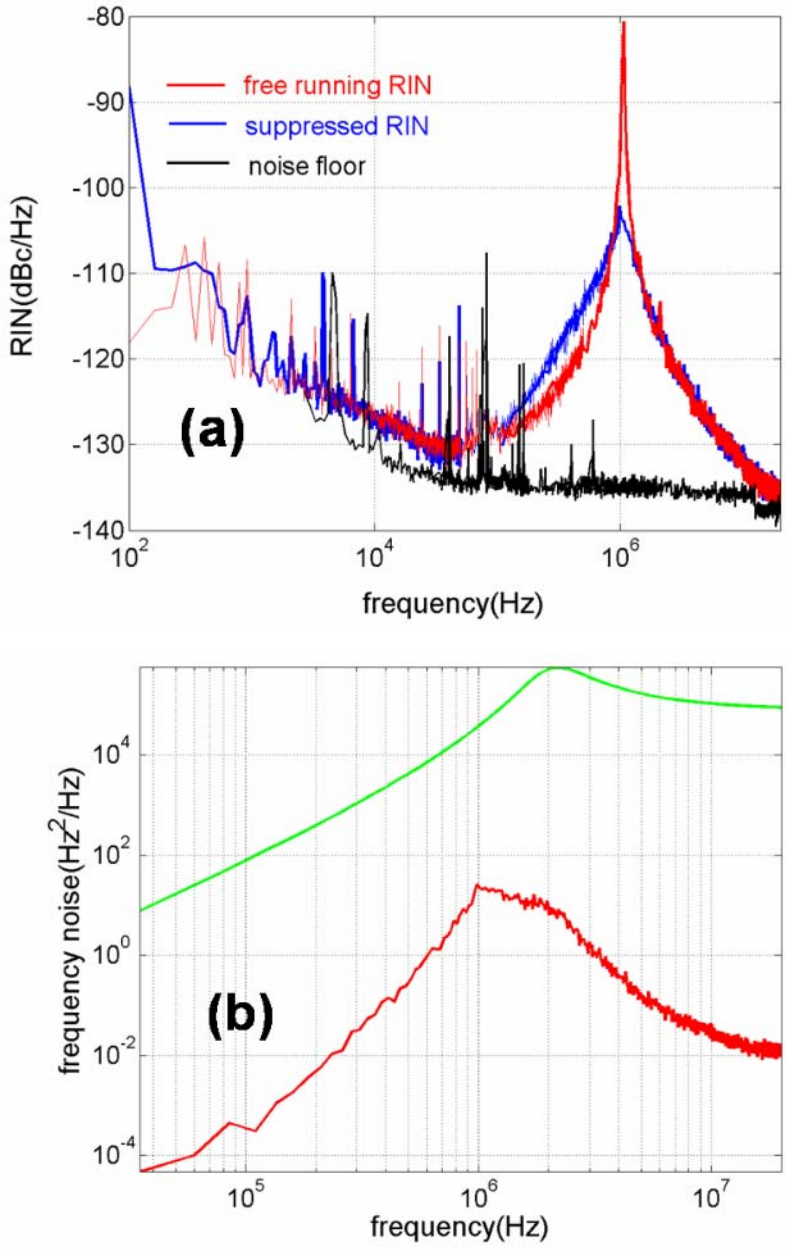

Fig. 6.9(a) Measured RIN of the NP fiber laser under both the free-running and the RIN suppression modes. (b) Calculated residual frequency noise of the locked slave laser (JDSU DFB) due to its free-running frequency noise (green curve) and to the RIN of the master laser(red curve). A white frequency noise corresponding to a FWHM of 0.3MHz

is assumed for the free-running slave laser.

I then use a fiber Mach-Zehnder interferometer to measure the frequency noise of the NP fiber laser. Because the fiber laser has significantly lower frequency noise compared to the Agilent laser and the JDSU DFB laser, a differential delay of ~50m has to be used to enhance the sensitivity of the interferometer. However, the small free spectral range of the interferometer, combined with the frequency jitter of the NP laser, makes it very difficult to bias the Mach Zehnder interferometer at the quadrature point long enough to take a measurement of the frequency noise spectrum with a small enough resolution and video bandwidth. To solve this problem, I measure a large number of traces of the frequency noise spectrum at random times and average these traces. In order to prove that this method works, I expand Eq. (6.20) to

$$I/\left(2\eta E_0^2\right) \simeq 1+\cos\omega_0\tau_0\cos\Delta\phi\left(t,\tau_0\right)-\sin\omega_0\tau_0\sin\Delta\phi\left(t,\tau_0\right) \tag{6.34}$$

Under the small differential phase error assumption $\Delta\phi\left(t,\tau_0\right)<<1$, one keeps only the last term of Eq. (6.34), which leads to the relation Eq. (6.22) at the quadrature point $\omega_0\tau_0=\left(N+1/2\right)\pi$. In general $\omega_0\tau_0$ varies with time and can be any value due to the frequency jittering of the laser and the variation of the interferometer, and the measured frequency noise spectrum has an additional multiplication factor $\sin^2\left(\omega_0\tau_0\right)$. If one takes the average of a large number of traces, it is equivalent to averaging the factor $\overline{\sin^2\left(\omega_0\tau_0\right)}=1/2$. Thus one only needs to calibrate the averaged frequency noise spectrum by a factor of 2 to get the right answer. However care must be taken if the small differential phase error assumption $\Delta\phi\left(t,\tau\right)<<1$ is not satisfied, since the second term in Eq. (6.34) is highly nonlinear away from the quadrature point, and can spread the spectral energy of the frequency noise and skew the measurement. An example of such a case will be given later.

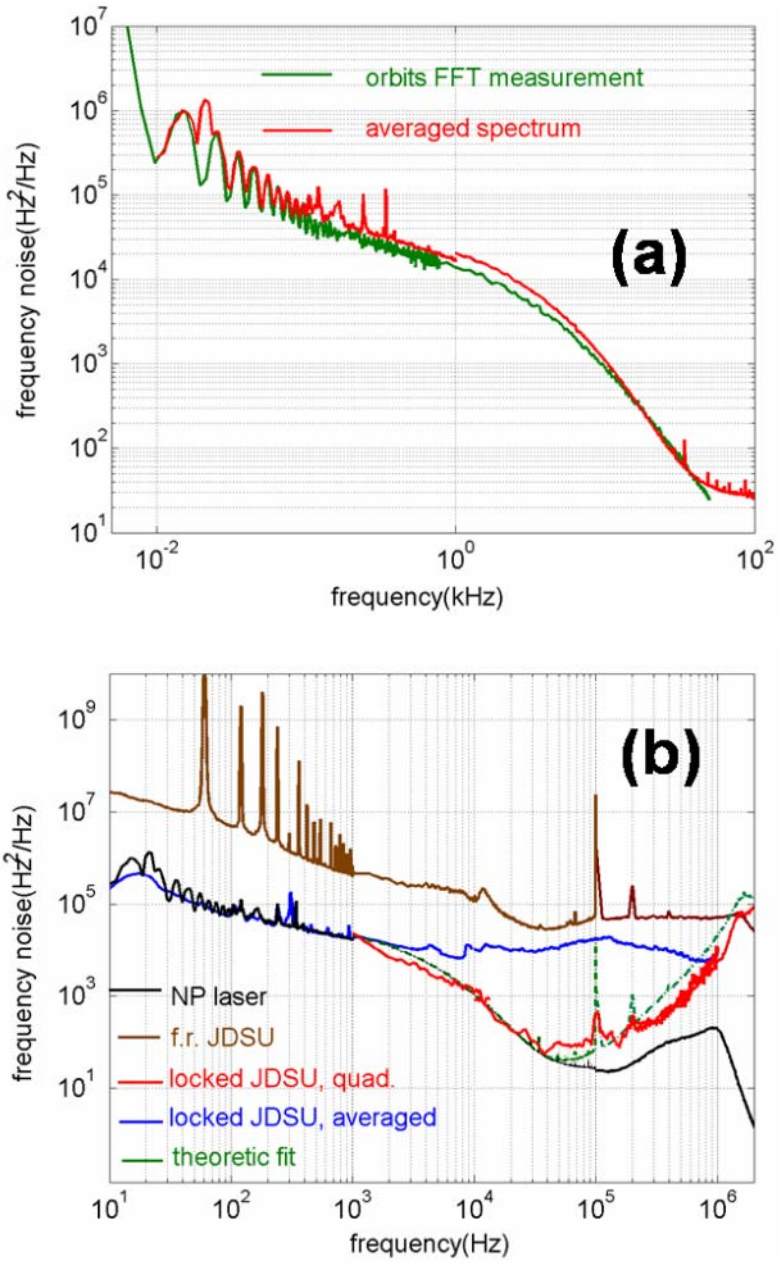

Fig. 6.10(a) Comparison of the measured frequency noises of the NP fiber laser. The green curve is measured in Orbitslightwave. Inc using a real-time spectrum analyzer, by taking the FFT of the output of the Mach Zehnder interferometer near the quadrature point. The red curve is measured by averaging a large number of traces taken by a sweep-filter type spectrum analyzer. In both measurements the differential delay of the interferometer is ~50m. (b) Comparison of the measured frequency noise of the master laser(NP fiber laser), the free-running and the locked JDSU laser. The red curve between

1kHz and 1MHz is measured at the quadrature point of an interferometer of 5m differential delay. The blue line is measured by averaging a large number of the frequency noise spectra using an interferometer of 50m differential delay. The green curve is a theoretical fitting of the frequency noise of the locked JDSU laser using Eq. (6.32).

Using the spectrum averaging approach, I measured the frequency noise of the NP fiber laser using an interferometer of 50m and plot it in Fig. 10(a). The green curve is measured using a real-time spectrum analyzer by taking the FFT of the output of the Mach Zehnder interferometer near the quadrature point. The results of the two approaches agree well with each other between 10Hz and 100kHz. Using the same approach, I also measured the frequency noise of the NP laser, the free-running and the locked JDSU laser from 10Hz to a few MHz. They are plotted in Fig. 10(b), respectively, as the black, the brown, and the blue curves. I also measured the frequency noise of the locked JDSU laser between 1kHz and 1MHz at the quadrature point of an interferometer of 5m delay. The data is plotted as the blue curve in Fig. 10(b). Using Eq. (6.32), I also calculate the expected frequency noise of the locked slave laser and plot it as the green curve. As can be seen, the spectrum averaging approach works well at frequency lower than ~30kHz and bigger than ~800kHz. In the range 30kHz-800kHz, the measured noise level is much higher than the expected value. Instead, the measurement taken at the quadrature point is close to the expected value. This is due to the significant nonlinearity of the second term in Eq. (6.34) when the interferometer drifts away from the quadrature point. The energy of the frequency noise at higher frequency spreads out to the lower frequency range through the nonlinear effect of the interferometer. The detailed study of the phenomenon is out of the scope of this thesis.

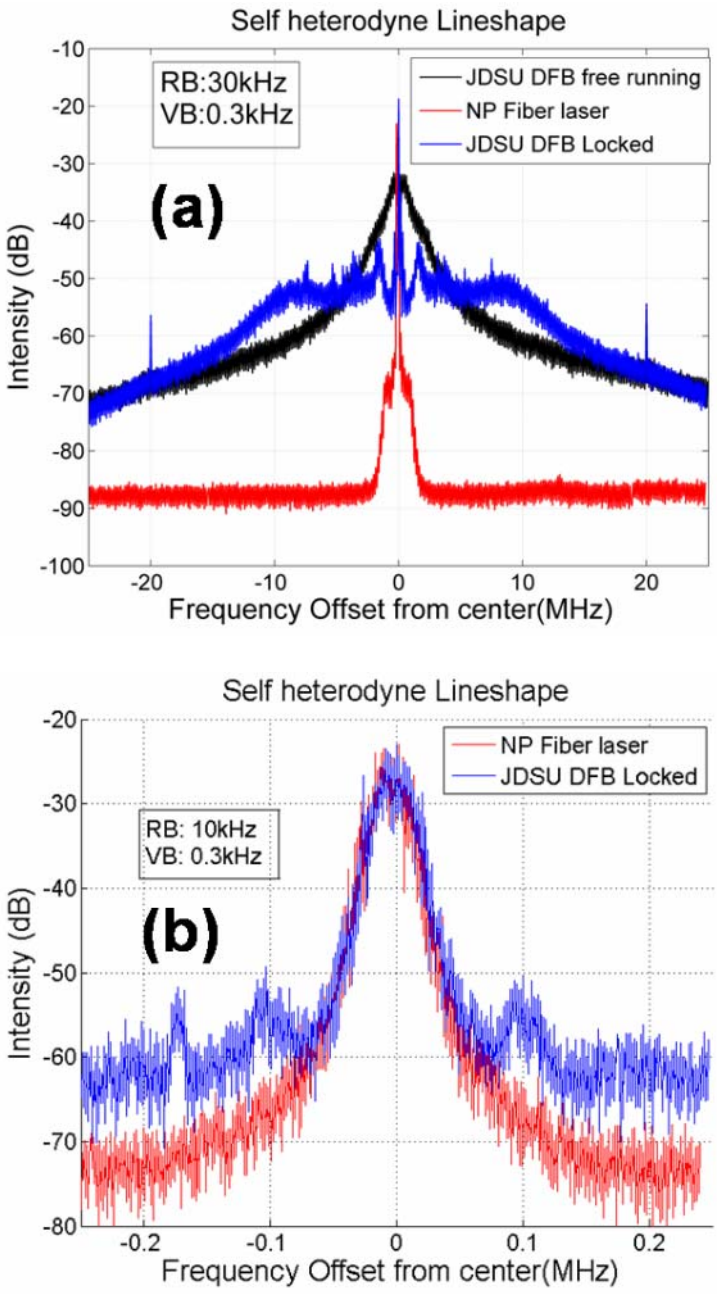

Fig. 6.11 Measured lineshapes of the master laser (NP fiber laser), the free-running and the locked slave laser (JDSU DFB) on a (a) 5MHz span and (b) 0.5MHz span

I also measured the lineshape of the NP fiber laser and the locked JDSU DFB laser. Using a delay line of 25km, the measured lineshapes of the NP fiber laser, the free-running JDSU DFB laser and the locked JDSU DFB laser are plotted and compared

in Fig. 6.11(a) on a span of 50MHz and in Fig. 6.11(b) on a span of 0.5MHz. One can see that the lineshape of the JDSU DFB laser follows that of the NP fiber laser within ± 50kHz frequency range and the 20dB full linewidth is reduced from ~5MHz to ~50kHz. The linewidth of the locked slave laser is still limited by the linewidth of the master laser. The part of the lineshape at higher frequencies is not affected due to the limited noise correction bandwidth of the OPLL. This observation is also consistent with the frequency noise measurement shown in Fig. 10(b), where the frequency noise of the locked JDSU laser follows that of the NP laser only for frequencies lower than ~50kHz.

Conclusion

In this chapter I have studied the application of OPLL in cloning the coherence property of a low phase noise fiber laser to an inexpensive commercial semiconductor DFB laser. Compared to fiber lasers, SCLs have very low RIN but much higher frequency noise. When the SCLs are phase locked to the fiber laser, they have essentially the same frequency noise as the fiber laser, meanwhile their RIN remains very low. Nevertheless, due to the insufficient loop bandwidth limited mainly by the non-uniform current-frequency modulation response of the SCLs, the coherence property of the fiber laser can only be cloned to the SCLs within a limited bandwidth. If multisection SCLs are used to remove this barrier, one can use the OPLL technology to obtain high power laser source of both low RIN and low phase noise for a number of critical applications.

Chapter 7 Conclusion

Most of the applications in the field of optics today utilize the intensity information of optical signals. The phase of an optical signal is at least equally, if not more, important than the intensity information. The tremendous potential of phase coherent optics is yet to be realized. OPLL provides a powerful tool to manipulate the phase of an optical signal. In this thesis I have studied OPLLs based on semiconductor lasers and the applications in coherent beam combining and coherence cloning. Looking into the future, significant amount of work needs to be done to bring this technology into practical applications.

First, similar to the PLL in electronic domain, OPLL is a technology platform that can enable numerous applications. Nevertheless, only a few applications based on OPLLs have been explored by researchers so far. The applications of this technology need to be significantly broadened by researchers to promote its further development.

Second, the performance of the OPLLs needs to be improved to bring them into practical applications. For OPLLs made from single section SCLs, the relatively small loop bandwidth(~MHz) limited by the phase reversal of the current-frequency modulation response presents the main obstacle toward achieving high performance OPLLs[22, 23, 36]. Firstly, the relatively small loop bandwidth combined with the large linewidth of SCLs leads to significant residual differential phase error between the master laser and the locked slave laser[10, 11, 91]. The smallest residual phase error I have shown in this thesis is about 0.1*rad*, which is far from being useful for certain applications requiring very low residual phase noise such as coherent optical communication, RF signal generation and delivery etc. For coherent beam combining, the residual phase error can significantly reduce the combining efficiency and the combined beam quality. For coherence cloning, the small loop bandwidth limits the frequency range in which the frequency noise of the slave laser can be reduced. Secondly, the large frequency jitter and drift of SCLs due to temperature variations, current noise, and mechanical vibration, require additional compensation circuits to stably lock the lasers.

To solve the problem, one has to come up with a better laser design for flat frequency modulation response up to 1GHz. For example, one can make a laser of multiple sections and drive each section with modulation currents of different amplitudes and phases. Multi-section lasers have been designed with a reasonably flat FM response up to a few GHz[24]. However, their FM response depends on the bias current and is likely to change during aging[23].

Another approach to get around the problem is to add an external phase/frequency modulator in addition to the slave laser. The combined FM response of the laser plus the external phase/frequency modulator can be made flat by driving them separately. A similar concept has already been applied to lock fiber lasers by adding an acoustic optical modulator[21]. Modulation of fiber laser is typically realized with PZT fiber stretcher and the bandwidth is usually limited to a few kHz. The AOM acts as a frequency shifter and has much higher modulation speed. The loop bandwidth of the combined system can thus be enhanced but still limited to less than 1MHz because of the relatively long traveling time of the acoustic wave in the AOM. Using a similar idea, one can add a phase modulator in order to increase the loop bandwidth of the SCL OPLL.

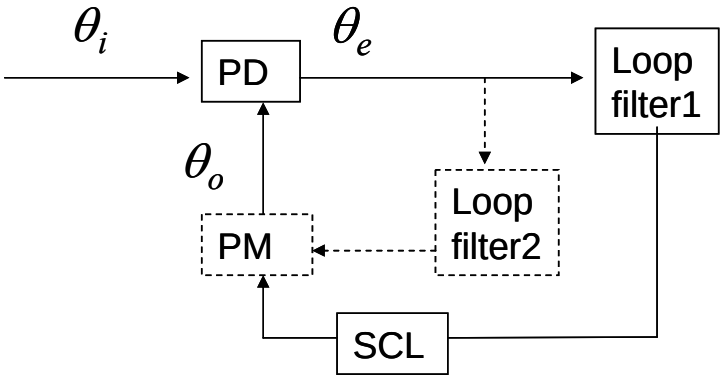

Fig. 7.1 Schematic diagram of an OPLL with a phase modulator (PM) feedback loop

Fig. 7.1 shows a schematic diagram of an OPLL with an additional phase modulator feedback loop. The solid lines and blocks stand for a typical OPLL built with a single-section SCL. In Chapter 2 I obtained the open loop transfer function of this OPLL as

$$G_{op}(s) = -\frac{K_{dc}F_1(s)H_{FM}^{DFB}(s)}{s}\exp(-s\tau_1) \tag{7.1}$$

where

$$H_{FM}^{DFB}(s) = -\frac{1}{1-a}\left(\frac{1}{1+\sqrt{s/2\pi f_c}} - a\right) \tag{7.2}$$

is the normalized FM response of the DFB laser. In Eq. (7.1), $s = j2\pi f$, and K_{dc}, $F_1(s)$, and τ_1 stand for the gain of the phase detector (PD), the transfer function of the loop filter 1 and the loop delay respectively. In Eq. (7.2) f_c is the structure-dependent thermal cut-off frequency of the slave laser and $a = K_{el}/K_{th}$ is the relative strength between the carrier effect and the thermal effect, and is typically smaller than 1.

Adding an external phase modulator following the DFB laser and using the same error signal to feed into the phase modulator as shown in Fig. 7.1, the OPLL contains two parallel feedback loops and the open loop transfer function is given by

$$G_{op}(s) = -\frac{K_d F_1(s)H_{FM}^{DFB}(s)}{s}\exp(-s\tau_1) + K_{PM}F_2(s)\exp(-s\tau_2) \tag{7.3}$$

where K_{PM}, $F_2(s)$, and τ_2 represent, respectively, the DC gain, the transfer function of the loop filter 2 and the delay of the PM feedback loop. In Eq. (7.3) I have assumed that the modulation strength of the phase modulator is almost constant within the frequency range (DC~ 1GHz) considered here. To simplify the analysis I first neglect all the loop delays and the loop filters. After substituting Eq. (7.2) into Eq. (7.3) one obtains

$$G_{op}(s) = \frac{K_{dc}}{s(1-a)}\left[-a + \frac{1}{1+\sqrt{s/2\pi f_c}}\right] + K_{PM} \tag{7.4}$$

The stability condition of the whole system requires $|G_{op}(s)| < 1$ at the π-phase frequency $\angle G_{op}(f_\pi) = -\pi$ [1]. Without the PM feedback loop, the thermal effect dominates at low frequency and gives way to the carrier effect at higher frequency. The

shifting of the dominant effect causes $G_{op}(s)$ to experience a π phase reversal btween 100kHz-10MHz and thus limits the loop bandwidth to the same frequency range. By adding the phase modulator feedback loop one "adds" the term K_{PM} in Eq. (7.4). When sufficiently large, the combined thermal and PM contribution can dominate the carrier effect at all frequencies and the phase reversal of $G_{op}(s)$ is eliminated. Thus the constraint on the loop bandwidth is removed.

Considering the long loop delay, the complexity and cost of discrete fiber optical components, the best way to implement OPLLs is using planar integrated optics. Looking back on the history of electronic PLLs, it is the invention of PLL integrated circuits that had made the wide applications of PLL take off. Today, the technology of integrating SCLs, PDs, modulators and waveguides on the same chip is already available. Should OPLL chips of low cost and high performance be implemented, its extensive applications in phase coherent optics and RF photonics can be expected.

References

1. F. M. Gardner, *Phaselock Techniques* (2005).
2. D. R. Stephens, *Phase-Locked Loops For Wireless Communications* (Kluwer Academic Publishers, 1998).
3. L. H. Enloe and J. L. Rodda, "Laser Phase-Locked Loop," Proceedings of the Institute of Electrical and Electronics Engineers **53**(2), 165-166 (1965).
4. M. Brunel, F. Bretenaker, S. Blanc, V. Crozatier, J. Brisset, T. Merlet, and A. Poezevara, "High-spectral purity RF beat note generated by a two-frequency solid-state laser in a dual thermooptic and electrooptic phase-locked loop," IEEE Photonics Technology Letters **16**(3), 870-872 (2004).
5. W. R. Leeb, H. K. Philipp, A. L. Scholtz, and E. Bonek, "Frequency Synchronization and Phase Locking of Co2-Lasers," Applied Physics Letters **41**(7), 592-594 (1982).
6. R. C. Steele, "Optical Phase-Locked Loop Using Semiconductor-Laser Diodes," Electronics Letters **19**(2), 69-71 (1983).
7. J. Harrison and A. Mooradian, "Linewidth and Offset Frequency Locking of External Cavity Gaalas Lasers," IEEE Journal of Quantum Electronics **25**(6), 1152-1155 (1989).
8. K. J. Williams, L. Goldberg, R. D. Esman, M. Dagenais, and J. F. Weller, "6-34 Ghz Offset Phase-Locking of Nd-Yag 1319nm Nonplanar Ring Lasers," Electronics Letters **25**(18), 1242-1243 (1989).
9. Z. F. Fan, P. J. S. Heim, and M. Dagenais, "Highly coherent RF signal generation by heterodyne optical phase locking of external cavity semiconductor lasers," IEEE Photonics Technology Letters **10**(5), 719-721 (1998).
10. U. Gliese, T. N. Nielsen, M. Bruun, E. L. Christensen, K. E. Stubkjaer, S. Lindgren, and B. Broberg, "A Wide-Band Heterodyne Optical Phase-Locked Loop for Generation of 3-18 Ghz Microwave Carriers," IEEE Photonics

Technology Letters **4**(8), 936-938 (1992).

11. L. N. Langley, M. D. Elkin, C. Edge, M. J. Wale, U. Gliese, X. Huang, and A. J. Seeds, "Packaged semiconductor laser optical phase-locked loop (OPLL) for photonic generation, processing and transmission of microwave signals," IEEE Transactions on Microwave Theory and Techniques **47**(7), 1257-1264 (1999).
12. J. M. Kahn, B. L. Kasper, and K. J. Pollock, "Optical Phaselock Receiver with Multigigahertz Signal Bandwidth," Electronics Letters **25**(10), 626-628 (1989).
13. J. M. Kahn, A. M. Porter, and U. Padan, "Heterodyne-Detection of 310-Mb/S Quadriphase-Shift Keying Using 4th-Power Optical Phase-Locked Loop," IEEE Photonics Technology Letters **4**(12), 1397-1400 (1992).
14. D. A. Atlas and L. G. Kazovsky, "2 Gbit/S Psk Heterodyne Communication-System Using Optical Phase-Locked Loop," Electronics Letters **26**(14), 1030-1032 (1990).
15. M. Z. Win, C. C. Chen, and R. A. Scholtz, "Optical Phase-Locked Loop (Opll) for an Amplitude-Modulated Communications Link Using Solid-State Lasers," IEEE Journal on Selected Areas in Communications **13**(3), 569-576 (1995).
16. S. A. Diddams, J. C. Bergquist, S. R. Jefferts, and C. W. Oates, "Standards of time and frequency at the outset of the 21st century," Science **306**(5700), 1318-1324 (2004).
17. S. A. Diddams, D. J. Jones, J. Ye, S. T. Cundiff, J. L. Hall, J. K. Ranka, R. S. Windeler, R. Holzwarth, T. Udem, and T. W. Hansch, "Direct link between microwave and optical frequencies with a 300 THz femtosecond laser comb," Physical Review Letters **84**(22), 5102-5105 (2000).
18. L. S. Ma, Z. Y. Bi, A. Bartels, L. Robertsson, M. Zucco, R. S. Windeler, G. Wilpers, C. Oates, L. Hollberg, and S. A. Diddams, "Optical frequency synthesis and comparison with uncertainty at the 10(-19) level," Science **303**(5665), 1843-1845 (2004).

19. R. T. Ramos and A. J. Seeds, "Delay, Linewidth and Bandwidth Limitations in Optical Phase-Locked Loop Design," Electronics Letters **26**(6), 389-391 (1990).

20. F. Herzog, K. Kudielka, D. Erni, and W. Bachtold, "Optical phase locked loop for transparent inter-satellite communications," Optics Express **13**(10), 3816-3821 (2005).

21. J. F. Cliche and B. Shillue, "Precision timing control for radioastronomy - Maintaining femtosecond synchronization in the atacama large millimeter array," IEEE Control Systems Magazine **26**(1), 19-26 (2006).

22. S. Kobayashi, Y. Yamamoto, M. Ito, and T. Kimura, "Direct Frequency-Modulation in AlGaAs Semiconductor-Lasers," IEEE Journal of Quantum Electronics **18**(4), 582-595 (1982).

23. P. Correc, O. Girard, and I. F. Defaria, "On the Thermal Contribution to the Fm Response of Dfb Lasers - Theory and Experiment," IEEE Journal of Quantum Electronics **30**(11), 2485-2490 (1994).

24. M. Kuznetsov, "High-Speed Frequency-Modulation and Switching of Tunable Distributed Feedback Lasers with 2 Active Segments," IEEE Journal of Quantum Electronics **27**(3), 668-677 (1991).

25. S. J. Augst, T. Y. Fan, and A. Sanchez, "Coherent beam combining and phase noise measurements of ytterbium fiber amplifiers," Optics Letters **29**(5), 474-476 (2004).

26. G. L. Schuster and J. R. Andrews, "Coherent Beam Combining - Optical Loss Effects on Power Scaling," Applied Optics **34**(30), 6801-6805 (1995).

27. C. X. Yu, J. E. Kansky, S. E. J. Shaw, D. V. Murphy, and C. Higgs, "Coherent beam combining of large number of PM fibres in 2-D fibre array," Electronics Letters **42**(18), 1024-1025 (2006).

28. L. Bartelt-Berger, U. Brauch, A. Giesen, H. Huegel, and H. Opower, "Power-scalable system of phase-locked single-mode diode lasers," Applied

Optics **38**(27), 5752-5760 (1999).

29. S. Demoustier, A. Brignon, E. lallier, and J. P. Huignard, "Coherent Combining of 1.5um Er-Yb Doped Single Mode Fiber Amplifier," in Conference on Lasers and Electro-Optics/Quantum Electronics and Laser Science Conference and Photonic Applications Systems Technologies, Technical Digest (CD) (Optical Society of America, 2006), paper CThAA5. (2006).
30. J. L. Hall, "Stabilized Lasers and Precision-Measurements," Science **202**(4364), 147-156 (1978).
31. B. C. Young, F. C. Cruz, W. M. Itano, and J. C. Bergquist, "Visible lasers with subhertz linewidths," Physical Review Letters **82**(19), 3799-3802 (1999).
32. L. B. Mercer, "1/F Frequency Noise Effects on Self-Heterodyne Linewidth Measurements," Journal of Lightwave Technology **9**(4), 485-493 (1991).
33. A. C. Bordonalli, C. Walton, and A. J. Seeds, "High-performance phase locking of wide linewidth semiconductor lasers by combined use of optical injection locking and optical phase-lock loop," Journal of Lightwave Technology **17**(2), 328-342 (1999).
34. Y. Yamamoto, O. Nilsson, and S. Saito, "Theory of a Negative Frequency Feedback Semiconductor-Laser," IEEE Journal of Quantum Electronics **21**(12), 1919-1928 (1985).
35. A. Yariv, "Dynamic analysis of the semiconductor laser as a current-controlled oscillator in the optical phased-lock loop: applications," Optics Letters **30**(17), 2191-2193 (2005).
36. G. S. Pandian and S. Dilwali, "On the Thermal Fm Response of a Semiconductor-Laser Diode," IEEE Photonics Technology Letters **4**(2), 130-133 (1992).
37. S. Saito, O. Nilsson, and Y. Yamamoto, "Coherent Fsk Transmitter Using a Negative Feedback Stabilized Semiconductor-Laser," Electronics Letters **20**(17),

703-704 (1984).

38. W. V. Sorin, K. W. Chang, G. A. Conrad, and P. R. Hernday, "Frequency-Domain Analysis of an Optical Fm Discriminator," Journal of Lightwave Technology **10**(6), 787-793 (1992).

39. A. Yariv, *Optical Electronics in Modern Communications,* Fifth ed. (Oxford University Press, 1996).

40. M. Ohtsu and S. Kotajima, "Linewidth Reduction of a Semiconductor-Laser by Electrical Feedback," IEEE Journal of Quantum Electronics **21**(12), 1905-1912 (1985).

41. M. Ohtsu and N. Tabuchi, "Electrical Feedback and Its Network Analysis for Linewidth Reduction of a Semiconductor-Laser," Journal of Lightwave Technology **6**(3), 357-369 (1988).

42. M. Poulin, C. Latrasse, D. Touahri, and M. Tetu, "Frequency stability of an optical frequency standard at 192.6 THz based on a two-photon transition of rubidium atoms," Optics Communications **207**(1-6), 233-242 (2002).

43. W. Liang, N. Satyan, A. Yariv, A. Kewitsch, G. Rakuljic, F. Aflatouni, H. Hashemi, and J. Ungar, "Coherent power combination of two Master-oscillator-power-amplifier (MOPA) semiconductor lasers using optical phase lock loops," Optics Express **15**(6), 3201-3205 (2007).

44. S. J. Augst, A. K. Goyal, R. L. Aggarwal, T. Y. Fan, and A. Sanchez, "Wavelength beam combining of ytterbium fiber lasers," Optics Letters **28**(5), 331-333 (2003).

45. J. R. Leger, M. Holz, G. J. Swanson, and W. Veldkamp, "Coherent beam addition: An application of binary optics," Lincoln Lab Journal **1**, 225-245 (1988).

46. T. Y. Fan, "Laser beam combining for high-power, high-radiance sources," IEEE Journal of Selected Topics in Quantum Electronics **11**(3), 567-577 (2005).

47. J. R. Leger, ed., *External methods of phase locking and coherent beam addition of diode lasers*, Surface Emitting Semiconductor Lasers and Arrays (Academic,

Boston, 1993), pp. 379-433.

48. A. F. Glova, "Phase locking of optically coupled lasers," Quantum Electronics **33**(4), 283-306 (2003).

49. R. K. Huang, B. Chann, L. J. Missaggia, J. P. Donnelly, C. T. Harris, G. W. Turner, A. K. Goyal, T. Y. Fan, and A. Sanchez-Rubio, "High-brightness wavelength beam combined semiconductor laser diode arrays," IEEE Photonics Technology Letters **19**(2-4), 209-211 (2007).

50. B. Chann, R. K. Huang, L. J. Missaggia, C. T. Harris, Z. L. Liau, A. K. Goyal, J. P. Donnelly, T. Y. Fan, A. Sanchez-Rubio, and G. W. Turner, "Near-diffaction limited diode laser arrays by wavelength beam combining," Optics Letters **30**(16), 2104-2106 (2005).

51. A. Shirakawa, T. Saitou, T. Sekiguchi, and K. Ueda, "Coherent addition of fiber lasers by use of a fiber coupler," Optics Express **10**(21), 1167-1172 (2002).

52. C. D. Nabors, "Effects of Phase Errors on Coherent Emitter Arrays," Applied Optics **33**(12), 2284-2289 (1994).

53. S. Menard, M. Vampouille, A. Desfarges-Berthelemot, V. Kermene, B. Colombeau, and C. Froehly, "Highly efficient phase locking of four diode pumped Nd : YAG laser beams," Optics Communications **160**(4-6), 344-353 (1999).

54. M. Oka, H. Masuda, Y. Kaneda, and S. Kubota, "Laser-Diode-Pumped Phase-Locked Nd-Yag Laser Arrays," IEEE Journal of Quantum Electronics **28**(4), 1142-1147 (1992).

55. L. J. Mawst, D. Botez, C. Zmudzinski, M. Jansen, C. Tu, T. J. Roth, and J. Yun, "Resonant Self-Aligned-Stripe Antiguided Diode-Laser Array," Applied Physics Letters **60**(6), 668-670 (1992).

56. S. Saunders, R. Waarts, D. Nam, D. Welch, D. Scifres, J. C. Ehlert, W. J. Cassarly, J. M. Finlan, and K. M. Flood, "High power coherent two-dimensional semiconductor laser array," Applied Physics Letters **64**, 1478 (1994).

57. Y. Kono, M. Takeoka, K. Uto, A. Uchida, and F. Kannari, "A coherent all-solid-state laser array using the Talbot effect in a three-mirror cavity," IEEE Journal of Quantum Electronics **36**(5), 607-614 (2000).

58. L. A. Newman, R. A. Hart, J. T. Kennedy, A. J. Cantor, A. J. Demaria, and W. B. Bridges, "High-Power Coupled Co2 Wave-Guide Laser Array," Applied Physics Letters **48**(25), 1701-1703 (1986).

59. J. R. Leger, G. J. Swanson, and W. B. Veldkamp, "Coherent Laser Addition Using Binary Phase Gratings," Applied Optics **26**(20), 4391-4399 (1987).

60. J. S. Osinski, D. Mehuys, D. F. Welch, R. G. Waarts, J. S. Major, K. M. Dzurko, and R. J. Lang, "Phased-Array of High-Power, Coherent, Monolithic Flared Amplifier Master Oscillator Power-Amplifiers," Applied Physics Letters **66**(5), 556-558 (1995).

61. K. H. No, R. W. Herrick, C. Leung, R. Reinhart, and J. L. Levy, "One-Dimensional Scaling of 100 Ridge-Wave-Guide Amplifiers," IEEE Photonics Technology Letters **6**(9), 1062-1066 (1994).

62. B. A. Demoustier S, lallier E and Huignard J.P., "Coherent Combining of 1.5um Er-Yb Doped Single Mode Fiber Amplifier," (2006).

63. D. S. Elliott, R. Roy, and S. J. Smith, "Extra-Cavity Laser Band-Shape and Bandwidth Modification," Physical Review A **26**(1), 12-18 (1982).

64. D. M. A. Janice K. Lawson, R. Edward English, Jr., Wayne T. Whistler, Will House, and Michael A. Nichols "Surface figure and roughness tolerances for NIF optics and the interpretation of the gradient, P-V wavefront, and RMS specifications," presented at the SPIE Optical Manufacturing and Testing III, 1999.

65. G. J. Cowle, P. R. Morkel, R. I. Laming, and D. N. Payne, "Spectral Broadening Due to Fiber Amplifier Phase Noise," Electronics Letters **26**(7), 424-425 (1990).

66. E. Desurvire, *Erbium-Doped Fiber Amplifiers Principles and Applications* (Wiley,

New York:, 1994), pp. 399–404.

67. L. Moller, "Novel aspects of spectral broadening due to fiber amplifier phase noise," Ieee Journal of Quantum Electronics **34**(9), 1554-1558 (1998).

68. E. Rochat and R. Dandliker, "New investigations on the effect of fiber amplifier phase noise," IEEE Journal of Selected Topics in Quantum Electronics **7**(1), 49-54 (2001).

69. C. Latrasse, F. Pelletier, A. Doyle, S. Savard, A. Babin, F. Costin, A. Biron, J. F. Cliche, M. Allard, and M. Tetu, "High Performances Frequency-Stabilized Semiconductor Laser Metrology Sources for Space-borne Spectrometers " presented at the Sixth International Conference on Space Optics, Proceedings of ESA/CNES ICSO 2006, ESTEC, Noordwijk, The Netherlands, 2006.

70. K. Kuboki and M. Ohtsu, "A Synthesized Method to Improve Coherence in Semiconductor-Lasers by Electrical Feedback," IEEE Journal of Quantum Electronics **25**(10), 2084-2090 (1989).

71. "See for example: VIRGO (www.vascina.virgo.infn.it), LIGO (www.ligo.caltech.edu) LISA(lisa.jpl.nasa.gov), ALMA(www.eso.org/projects/alma)".

72. "see for example: http://www.rp-photonics.com/linewidth.html, http://orbitslightwave.com/mainpages/Press_release_Ethernal1060.html, http://www.npphotonics.com/."

73. C. H. Henry, "Theory of the Linewidth of Semiconductor-Lasers," IEEE Journal of Quantum Electronics **18**(2), 259-264 (1982).

74. K. Vahala and A. Yariv, "Semiclassical Theory of Noise in Semiconductor-Lasers I," IEEE Journal of Quantum Electronics **19**(6), 1096-1101 (1983).

75. K. Vahala and A. Yariv, "Semiclassical Theory of Noise in Semiconductor-Lasers II," IEEE Journal of Quantum Electronics **19**(6), 1102-1109 (1983).

76. C. Harder, K. Vahala, and A. Yariv, "Measurement of the Linewidth Enhancement Factor-Alpha of Semiconductor-Lasers," Applied Physics Letters **42**(4), 328-330

(1983).

77. J. A. Barnes, A. R. Chi, L. S. Cutler, D. J. Healey, D. B. Leeson, McGuniga.Te, J. A. Mullen, W. L. Smith, R. L. Sydnor, R. F. C. Vessot, and G. M. R. Winkler, "Characterization of Frequency Stability," IEEE Transactions on Instrumentation and Measurement **IM20**(2), 105-& (1971).

78. P. Lesage and C. Audoin, "Characterization and Measurement of Time and Frequency Stability," Radio Science **14**(4), 521-539 (1979).

79. A. Dandridge and H. F. Taylor, "Correlation of Low-Frequency Intensity and Frequency Fluctuations in Gaaias Lasers," IEEE Journal of Quantum Electronics **18**(10), 1738-1750 (1982).

80. G. M. Stephan, T. T. Tam, S. Blin, P. Besnard, and M. Tetu, "Laser line shape and spectral density of frequency noise," Physical Review A **71**(4)(2005).

81. Y. Yamamoto, S. Saito, and T. Mukai, "Am and Fm Quantum Noise in Semiconductor-Lasers .2. Comparison of Theoretical and Experimental Results for Algaas Lasers," Ieee Journal of Quantum Electronics **19**(1), 47-58 (1983).

82. K. Kikuchi, "Effect of 1/F-Type Fm Noise on Semiconductor-Laser Linewidth Residual in High-Power Limit," IEEE Journal of Quantum Electronics **25**(4), 684-688 (1989).

83. A. Yariv and W. M. Caton, "Frequency, Intensity, and Field Fluctuations in Laser Oscillators," IEEE Journal of Quantum Electronics **QE10**(6), 509-515 (1974).

84. Armstron.Ja, "Theory of Interferometric Analysis of Laser Phase Noise," Journal of the Optical Society of America **56**(8), 1024-& (1966).

85. E. D. Hinkley and C. Freed, "Direct Observation of Lorentzian Line Shape as Limited by Quantum Phase Noise in a Laser above Threshold," Physical Review Letters **23**(6), 277-& (1969).

86. Y. Yamamoto, T. Mukai, and S. Saito, "Quantum Phase Noise and Linewidth of a Semiconductor-Laser," Electronics Letters **17**(9), 327-329 (1981).

87. H. E. ROWE, *Signal and Noise in Communication Systems* (Van Nostrand, Princeton, NJ, 1965).

88. D. W. Allan, "Statistics of Atomic Frequency Standards," Proceedings of the Institute of Electrical and Electronics Engineers **54**(2), 221-& (1966).

89. P. B. Gallion and G. Debarge, "Quantum Phase Noise and Field Correlation in Single Frequency Semiconductor-Laser Systems," IEEE Journal of Quantum Electronics **20**(4), 343-349 (1984).

90. K. Y. Lau, N. Barchaim, I. Ury, C. Harder, and A. Yariv, "Direct Amplitude-Modulation of Short-Cavity Gaas-Lasers up to X-Band Frequencies," Applied Physics Letters **43**(1), 1-3 (1983).

91. M. A. Grant, W. C. Michie, and M. J. Fletcher, "The Performance of Optical Phase-Locked Loops in the Presence of Nonnegligible Loop Propagation Delay," Journal of Lightwave Technology **5**(4), 592-597 (1987).